TOWARDS ARTIFICIAL PROPRIOCEPTION IN THE MANDIBULAR FULL ARCH FIXED IMPLANT PROSTHESIS

by

MD ABU HASAN

DISSERTATION

Submitted in partial fulfillment of the requirements
for the degree of Doctor of Philosophy at
The University of Texas at Arlington
December, 2016

Arlington, Texas

Supervising Committee:

Panos S. Shiakolas, Supervising Professor
Pranesh B. Aswath
Jonathan W. Bredow
Elias D. Kontogiorgos
Kent L. Lawrence
Luca Maddalena

Abstract

TOWARDS ARTIFICIAL PROPRIOCEPTION IN THE MANDIBULAR FULL ARCH FIXED IMPLANT PROSTHESIS

Md Abu Hasan, Ph.D.

The University of Texas at Arlington, 2016

Supervising Professor: Panos S. Shiakolas

Full arch fixed implant prosthesis has been one of the most effective treatment modalities for fully edentulous patients over the last few decades. However, due to lack of proprioception occlusal overload is experienced by the prosthesis and its components causing major biomechanical complications such as screw/abutment fracture, framework fracture, and bone loss. The currently available approaches for the overload management rely on external appliances such as an occlusal splint or bite guard and result in occlusal discomfort and high patient dissatisfaction. In this research, an approach to induce artificial proprioception in the full arch fixed implant prosthesis is proposed. However, the primary contribution of the research is the design and development of a tooth embeddable sensor to monitor occlusal load without requiring any external appliance. Studying the biomechanics of artificial dentition and available occlusion schemes, a two-axis force sensor (strain gauge based) was designed for a single acrylic resin tooth (molar). The design is based on lingualized

occlusion scheme for centric occlusion and group function scheme for lateral occlusion. A cavity was created inside the molar tooth to obtain a measurable deformation and encapsulate the sensing mechanism. Finite element models were developed to study the effects of material and geometric parameters of the tooth on deformation profiles at the lower occlusal surface of the cavity. The tooth and two-axis force sensing mechanism were prototyped using additive manufacturing. Sensing strain gauges were added on the sensing structure beams and the components were assembled inside the tooth. The responses from the sensors were experimentally characterized under a mastication load and frequency of $50\ N$ and $1\ Hz$ respectively and theoretical models were developed for the loading and unloading responses to predict the system behavior. The vertical and horizontal force sensors exhibited good dynamic behavior under repeated loading. It was demonstrated that the developed force sensor can measure both vertical and horizontal loads in the occlusal surface of the molar tooth. Thus, the proposed tooth embeddable force sensor could potentially eliminate the issue of occlusal interference observed with external appliances and may significantly improve the prosthetic rehabilitation modalities for fully the edentulous patients.

Acknowledgements

I would like to thank my committee members for providing their valuable feedback to make the research better. My sincere gratitude to Dr. Kontogiorgos for helping me out in understanding the biomechanics of the denture, occlusion and prosthesis. The field of prosthodontics was completely new to me and without his help it would have been difficult to comprehend the clinical aspects. I would like to thank Dr. Maddalena for his constructive feedback. His recommendations helped me narrow down the scope of the research and focus on the major contribution. Thanks to Dr. Lawrence for his help with finite element modeling. I would also like to thank Dr. Aswath and Dr. Bredow for their time and feedback to improve the research outcome. Lastly, I would like to Thank Dr. Das at UTARI for fabricating all the design components.

I am indebted to UTA and the MAE department for providing me financial support throughout my academic career at UTA. Without the funding, I would not be able to survive here in the US.

I am very thankful to all my lab mates at the MARS Lab. My times in the lab were so great because of people like Chris, Prashanth, Michael, Salman and Shashank. I was always able to share any of my issues (personal or academic) with these great minds, and learned a lot along the way. Chris is an incredible human being and a great friend. Anytime I asked for any help with my research or academic stuff, Chris has always extended his helping hands. Thank you Chris! I would like to thank Prashanth for being a great friend and for helping me with my work in many occasions. All the countless discussions that I had with

Prashanth have helped me grow and push through the troubled times with my research work. Michael is another very helpful person and I am very thankful for all his help. I would also like to thank Shashank for being another great friend and helping me out with some of the experiments.

Lastly, I am forever grateful to my advisor Dr. Shiakolas. I am thankful for his incredible support and guidance. I made mistakes along the way, but he was always patient and showed faith in me. There were times when I lost focus, but he helped me focus on the major contribution of the research. Dr. Shiakolas is very helpful, hardworking and a great human being. I cannot thank him enough for the countless hours that he spent reading my documents/manuscripts, providing feedback, guidance and future directions for my research. This research would not have come this far without his constant motivation and urge to focus on the essentials and intellectual aspects. Thank you Dr. Shiakolas.

Dedication

I am thankful to my family for raising me and providing unending support throughout my whole life. It is for their incredible love and support, and by the grace of Almighty, I am the first person in my whole family who has come so far in the academic level. I owe it to my parents for everything that I am today. I owe it to my brother for teaching me how to cultivate a positive attitude and increase mental strength. I owe it to my sister for her countless blessings.

I consider myself lucky to have a wife like Obany, to whom I have been married for more than two years now. I know that I have not been able to give her much, but she never stopped smiling. During the times of hardships, she always stood by my side and gave me the space that I needed. I owe it to you Obany!

Table of Contents

List of Illustrations

List of Tables

1 Introduction

1.1 Motivation

Healthy natural teeth are not only vital for physical health but also important for the well-being of individuals in personal and social settings. Unfortunately, teeth loss is a common phenomenon all around the world. In the United States, 1 out of every 200 people between the ages of 20 to 39, 1 out of every 20 people between the ages of 40 to 59, and 1 out of every 4 people of age 60 and older are missing all of their natural teeth.[1] Furthermore, according to the American Association of Oral and Maxillofacial Surgeons (AAOMS), 69% of adults (age 35 to 44) lose at least one permanent tooth due to accidents, tooth decay, gum disease, etc. In order to restore the ability to eat, speak and function properly these people resort to dental prosthesis, an industry which is worth $70 billion each year.[1] Although the rate of edentulism has been decreasing each decade for the past 30 years, the number of edentulous (the state of being devoid of natural teeth) people is still expected to increase because of the rising number of adult population.[2] By the year 2020, a growth of 79% is expected in the older population of age 55 years or older in the US and 90% of them obtain dentures according to national epidemiologic survey data.[3] Thus, the required number of complete dentures (in the US alone) is expected to increase from 53.8 million in 1991 to 61.0 million in 2020.[3] This research contributes towards the well-being of edentulous people by proposing an approach to induce artificial proprioception in the full arch fixed implant prosthesis through the

conceptualization, design, prototype and functional demonstration of a tooth embeddable two-axis force sensor.

1.2 Thesis Organization

The first chapter introduces the background of dental prosthesis, biomechanical complications, related work and an overview of the proposed approach. The second chapter presents tooth biomechanics, occlusion principles and Finite Element Analysis (FEA) of a molar tooth to evaluate deformation under a maximum mastication load. The third chapter presents the design of a two-axis force sensing mechanism and associated stress/strain analysis. Chapter 4 discusses the experimental setup, sensor response characterization and methodology for sensor calibration. The conclusions and recommendations for future research are discussed in Chapter 5.

1.3 Dental Prosthesis/Clinical Background

Dental prosthesis is defined as an artificial replacement of one or more missing teeth and associated dental structures.[4] There are two types of dental prostheses: fixed and removable. Fixed prostheses use dental adhesive, screws or dental implants to secure the device in place, whereas removable prostheses use clasps to grab onto the nearby teeth or rest onto the gum ridge.[5,6]

A denture is an example of a removable prosthesis. It is an artificial substitute that replaces all missing teeth and adjacent tissues. There are two parts of the denture: denture base and denture teeth. In general, the denture components are made of polymethylmethacrylate (PMMA) or acrylic resin.[7] Other

materials such as porcelain and composite resin are also used due to improved mechanical properties.[8] Dentures are custom made, molded and shaped to an individual's impression of the mouth based on dentist's prescription.

There are several types of dentures currently available: partial dentures, fixed bridge or fixed partial dentures, and complete dentures. Partial dentures are employed when some of the natural teeth still remain in the mouth following tooth loss as shown in Figure 1-A.[9] The original teeth prevent the denture from relocating or changing its orientation inside the mouth and hence increase the stability of the denture. Fixed partial dentures employ prosthetic teeth that are bonded to the roots of the natural teeth, or dental implants as shown in Figure 1-B.[10] They fill the gap which results from one or two missing teeth and are removable only by dentists. Complete dentures are considered when all the natural teeth are missing as shown in Figure 1-C.[9]

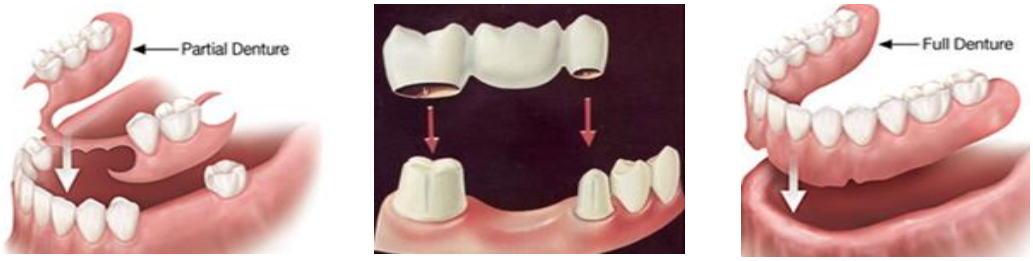

A B C

Figure 1: Denture types. A, Partial denture. B, Fixed partial denture. C, Full or complete denture

The major issue with the removable prostheses is that they are not rigidly connected to the bone. They tend to move from the original position upon application of occlusal load and compromise the health of surrounding healthy

natural teeth and oral tissues.[11] Moreover, the cortical bone slowly deteriorates as there is no forcing function to maintain its mechanical properties.[12] Consequently, the survival rate of removable dentures is generally low requiring frequent visit to the dentists.

The advent of dental implants proved to be useful in addressing these issues and has revolutionized the field of clinical dentistry. Dental implants are small devices that are surgically implanted in the jawbone to replace the roots of the natural teeth and provide solid bases for the prosthetic teeth.

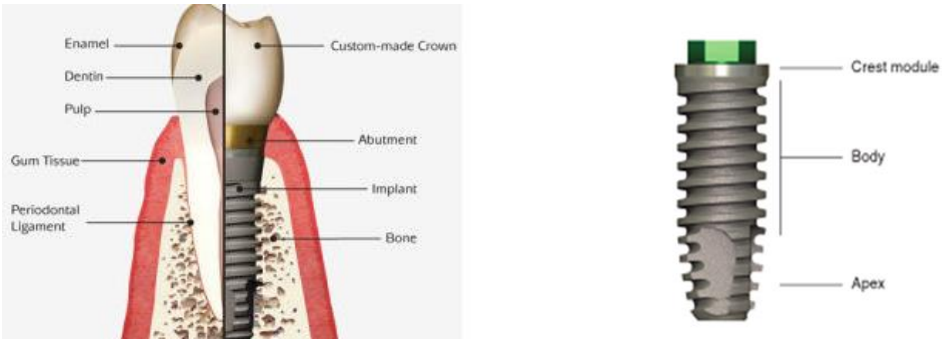

A B

Figure 2. Dental implant. A, Crown, abutment and implant. B, Implant body and crest module

The implant is generally constituted of a titanium implant body and an abutment as shown in Figure 2-A.[13] The abutment connects the prosthetic teeth (crown) with the implant body and can be of various types such as locator and ball abutment.[14] The full view of a representative implant body is shown in Figure 2-B. The bottom of the implant which is inserted in the trabecular bone is known as apex. Since the implant is attached to the bone, the occlusal load is directly

transferred to the same and hence substantial stimulus is generated to keep the periodontal tissue healthy. In addition, implant supported prostheses lose only 10% of the chewing efficiency compared to the natural teeth, whereas traditional dentures lose up to 35%.[15] It is for these reasons that the number of dental implants used in the U.S. increased more than 10 times from 1983 to 2002 and another 10 times from 2000 to 2010.[16]

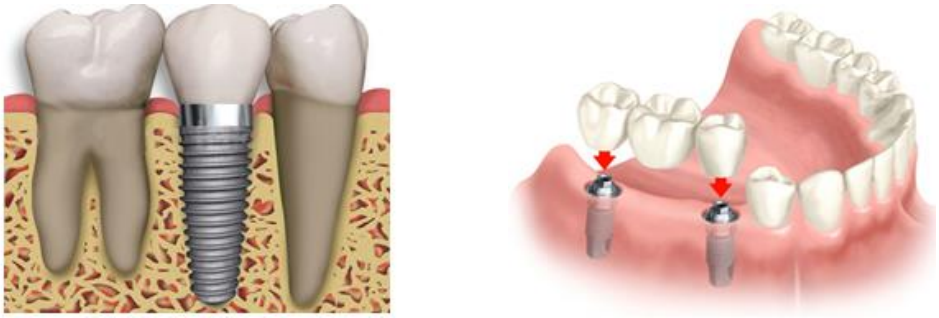

A B

Figure 3: Fixed implant prosthesis. A, Crown supported by a single implant. B, Fixed partial denture supported by two implants

Two basic uses of the implants are to provide artificial root for a single tooth replacement (Figure 3-A)[17] and to work as an anchor for fixed bridges (Figure 3-B)[18] or complete dentures (Figure 4-A&B).[9,19] Single tooth replacement with an implant is a standalone unit and does not involve treating the surrounding teeth. Anchoring the bridge with implants provides superior stability and better preserves the underneath bone.

Figure 4 illustrates different types of complete denture prostheses supported by dental implants. The complete denture can be jointly supported by the implants and soft tissue (Figure 4-A),[9] or it can be fully supported by the

implants (Figure 4-B).[19] The former is known as implant retained overdenture and the latter is known as full arch fixed implant prosthesis or hybrid prosthesis. Implant retained overdentures generally require two implants and are for those patients who are dissatisfied with the mobility of the complete denture and experience soreness in the mucosa. The function of implants in this type of prosthesis is to provide retention to the complete denture, not to bear the occlusal load. Hybrid prosthesis, on the other hand, provides full support to the denture prosthesis and bears the total load during occlusion. This type of restoration requires four or more implants to support the complete denture and can be provided to patients with sufficient inter-arch space and bone density.[20]

A B

Figure 4: Full arch implant prosthesis. A, Implant retained overdenture. B, Fixed implant supported prosthesis

The present study focuses on the implant supported mandibular prosthesis for the tooth embeddable force sensor design and its integration into the complete denture in an attempt to induce artificial proprioception. The long-

term success rate of the hybrid prosthesis is well documented and is becoming an increasingly popular treatment modality for the edentulous patients.

1.4 Biomechanical Complications

Even though the implant supported prostheses are becoming the standard of effective care for the edentulous patients over the last few decades, there are also various complications reported in the literature. The source of these complications can be categorized into two types: biological and biomechanical.

Biological complications include pain, inflammation and peri-implant bone loss.[21] According to Kwon et al. marginal bone loss is the most common biological complications of the hybrid prosthesis and might continuously occur in the peri-implant alveolar bone.[22] Papaspyridakos et al. investigated the biological and technical complications in the full arch fixed implant prosthesis and reported that the peri-implant bone loss was greater than $2\ mm$ at a rate of 20.1% after 5 years and 40.3% after 10 years.[23]

Bone remodeling at the cellular level is governed by mechanical strain which is directly related to the applied stress on the bone.[24,25] According to Frost, bone fractures at $10{,}000$ to $20{,}000\ \mu\varepsilon$ (1% to 2% deformation), and if the value is 20% to 40% of the mentioned strain levels then a process called bone resorption (break down of bone tissue) initiates.[26] Thus, occlusal stress beyond a physiological limit may introduce unwarranted mechanical strain leading to marginal bone loss. The situation is more critical under oblique loading, for

patients with softer bone or for full arch prosthesis with distal cantilever extension.

Biomechanical prosthetic complications are more frequently reported than biological complications and include implant and framework fractures, screw loosening, screw fracture, acrylic resin teeth fracture and wear, etc.[8,22,23,27,28] The most commonly reported issue in the full arch fixed implant prosthesis is acrylic resin teeth fracture.[22,27,29,30] Figure 5 shows cases of denture fracture in the hybrid prosthesis.[31] These fractures mostly occur at the beginning of the distal cantilever extension where the teeth debond or from the metal framework superstructure. In a recent long-term clinical study by Priest et al., the metal framework fracture was also found to be a significant concern occurring at an overall rate of 13% when opposed by fixed dental prosthesis.[27]

Figure 5: Hybrid prosthesis fracture

1.5 Biomechanical Complication Factors

There are several factors that are accountable for the biomechanical complications in the implant supported prosthesis. Mechanical overload is considered to be a major cause of such complications.[32–37] Occlusal overload is

defined as the application of functional or parafunctional loading in excess of the withstanding ability of the implant components and the bone-implant interface.[33] Excessive occlusal load not only causes multifarious biomechanical complications as mentioned in Section 1.4, but also affects peri-implant tissue health.[38] The effect of the overloading can be particularly detrimental for patients with insufficient bone volume, poor bone quality, poorly constructed prosthesis etc. Occlusal overload in the implant supported prosthesis is caused by a number of factors related to the biomechanics and design of the prosthesis. These factors are lack of proprioception, bruxism, absence of periodontal ligament and occlusion (occlusal interference or premature contact) and discussed in Subsections 1.5.1, 1.5.2, 1.5.3, and 1.5.4 respectively.

1.5.1 Lack of Proprioception

Natural teeth possess more occlusal awareness as compared to the dental implants. The proprioceptive information relayed by natural dentition is rapid and provides a sharp pain sensation under higher load. For instance, a study conducted by Trulsson and Gunne observed the act of three groups holding a peanut for 3 seconds between the teeth followed by biting through the same.[39] While the natural teeth group had no trouble with holding the peanut and biting, the implant and denture group bit with four times higher force than the group with natural dentition. Hence, the lack of proprioawareness in the implant supported prosthesis results in the application of higher forces by the patients during functional or parafunctional oral activities.[40] According to Robison et al. lack of proprioception can increase the masticatory force up to 7 to 10 times as

compared to the natural dentition.[7] An analogy to illustrate the difference of impact force between natural and implant supported teeth is hitting a nail with a rubber hammer (natural teeth) compared to a steel hammer (implant supported teeth).[41] Inappropriate implant positioning and poor occlusion may add further load to the prosthesis and make the restoration more vulnerable to failure.

1.5.2 Bruxism

Bruxism is a parafunctional oral activity that is defined by clenching and/or grinding of the teeth during sleep and wakefulness.[42,43] About 6 to 20% people suffer from bruxism and experience various biomechanical complications. In the US alone, 40 million people are reported to grind or clench their teeth.[44] Bruxism can be of two types: awake bruxism (AB) and sleep bruxism (SB). AB is also known as teeth clenching and is related to anxiety/stress stemming from personal and work life. SB, on the other hand, is characterized by grinding and/or clenching during sleep.[45] Bruxism has been positively correlated with complications such as teeth wear and prosthesis fracture and may lead to temporomandibular disorder (TMD).[36,46,47] In the literature, a higher number of technical complications (60% vs. 20% - five-year study) and implant failures (41% vs. 12% - one-year study) for patients with bruxism has been reported as compared to non-bruxists.[43] In a critical review on bruxism and prosthetic treatments, Johansson et al. emphasized that the heavy occlusal load due to bruxism should be reduced to maintain the structural integrity of the prostheses.[47] Force magnification of 4 to 7 times than the normal functional occlusion has been documented for patients with bruxism.[48]

1.5.3 Absence of Periodontal Ligament

Dental implants come in direct contact with the supporting bone as opposed to natural teeth which are connected via periodontal ligaments (PDL). The PDL is a fibrous connective tissue interface which acts as a viscoelastic "shock absorber".[49,50] In natural teeth the PDL increases the load dissipation time and reduces the induced stress levels at the crestal region.[41] Thus, the dental implants are stripped of cushion, and any occlusal overstressing thereby tends to gather around the crestal bone module. Moreover, when a force is applied, the crestal region may act as a fulcrum point making the region even more vulnerable to bone loss.[37] Aparna et al. conducted a finite element study and reported that the highest amount of bone loss is around the crestal bone region of the of loaded implants.[51]

1.5.4 Occlusion

Occlusion is defined as an act or process of closure or being closed.[4] An occlusal scheme is defined as the form and organization of occlusal contacts among the opposing teeth. The intensity and location of these occlusal contacts determine the amount and direction of load transfer in the fixed and removable prostheses. Thus, occlusion has been considered to play critical roles in increasing prosthesis longevity and to reduce biomechanical complications of the prosthesis.[52] An ideal occlusion is the one which provides stability, efficient mastication and aesthetic appeal without causing undue complications to the underlying hard and soft tissues.[53] Currently, there are many occlusal schemes available for the complete denture occlusion.[54] However, there is no general

consensus as to which occlusal scheme is superior to the others. Therefore, the choice of the scheme is primarily governed by empirical evidence and personal judgment of the practitioners.[54–56]

An improper occlusal scheme sometimes may lead to occlusal interference which is defined as any tooth contact that prevents the remaining occlusal surfaces from coming in contact.[4] This type of interference is detrimental to the prosthesis stability and generates excessive forces. Premature contact is another occlusal abnormality that acts as a force magnifier. This is also known as a deflective occlusal contact which reroutes the mandible from its desired movement or displaces a tooth leading to instability. According to Michalakis et al. premature contact of as little as $100\ \mu m$ can cause significant increase of bite force.[57]

1.6 Measures to Prevent Overloading

Significant research has been performed to reduce the biomechanical complications of the implant supported prosthesis. The proposed/established solutions range from providing feedback to the user through intra-oral appliances to modification of current occlusion schemes. In this section, the currently available approaches for the occlusal overload management are discussed based on open literature. Subsection 1.6.1 presents various feedback mechanisms based on sensor integration into external appliances, and Subsection 1.6.2 presents recommended occlusion schemes for the implant supported prosthesis and proposed modifications to reduce detrimental effects due to overload.

1.6.1 Occlusal Splint or Bite Guard

The most common approach to managing occlusal overload has been wearing occlusal appliance such as a bite guard/occlusal splint.[45,58,59] An occlusal bite guard is a removable dental device which is worn over the teeth to protect them from damage due to excessive occlusal load stemming from clenching, grinding or temporomandibular (TMD) disorder.[60] The inherent limitation of the bite guard is that it is designed to only protect the teeth from wearing down, and cannot remove or alleviate parafunctional habit.

Recently, providing biofeedback to the user has been a promising approach for patients with severe clenching, grinding or TMD disorder.[45,59] The form of feedback can be visual, auditory, vibratory, electrical, tactile signals or a combination of them.[45] Incorporation of biofeedback modality for the occlusal overload management has been achieved by relying on various sensing mechanisms in the bite guard or by using electromyography (EMG) of masticatory muscles.[59,60]

EMG is defined as the graphical recording of action potentials generated during activation of masticatory muscles and has been extensively used to provide feedback to the end user.[4] This approach measures the electrical impulse generated due to the movement of the masseter muscle during sleep and compares the value with predetermined maximum voluntary tooth clenching. By measuring the duration and amplitude of the generated signals, the pattern and magnitude of the loading are determined.[61] While this method is extensively used for the diagnosis or monitoring of bruxism, the EMG signal is affected by

the position of electrode placement, posture, skin resistance etc.[59] Furthermore, it is uncomfortable for the patients to sleep with attached electrodes and hence this method causes trouble sleeping.[59]

Alternative to EMG has been pressure sensitive transducers integrated into the occlusal bite guard for the monitoring of occlusal forces. Lantada et al. incorporated a force to resistance transducer in the occlusal bite guard and powered it wirelessly by using a magnetic near field communication scheme.[62] Another group of researchers designed a wireless pressure sensing bite-guard to monitor bruxism in real time.[59] They fabricated a pressure sensitive polymer composite and encapsulated the composite in the occlusal bite splint. The pressure sensitive polymer is composed of conductive fillers (e.g. carbon) distributed homogeneously in an insulating matrix (PDMS pre-polymer). As pressure is applied, a conductive path is formed in the insulating matrix resulting in a change of resistance proportional to the applied pressure.[63] Nordlander et al. incorporated a thin layer of piezoelectric film in the acrylic splint (patented) which emits small current as a result of compression during tooth contact.[64] The piezoelectric film is connected to a battery-powered radio transmitter (RT) to transmit the radio frequency signal outside in conjunction with a remote receiver module. If the received signal is above a predefined threshold value, the receiver module generates an audible alarm. Another patented device is based on optical sensing principle.[65] The device tracks the position of the lower mandibular jaw by mounting a position sensitive detector (PSD) on a dental removable appliance placed in one arch and a light source such as light emitting diode (LED) mounted

on the opposite arch. The pattern of the jaw movement is obtained by tracking the position of the light source. Knowing the jaw motion kinematics effective measures can be undertaken to restore the teeth in a way that helps resist the forces arising from parafunctional activities and improve the longevity of the teeth.

Although the mentioned sensing mechanisms have shown promising results, their major deficiency is that they completely rely on external occlusal appliances (e.g. bite guard). In order to allow for the monitoring, patients have to wear the bite guard and follow certain cautionary steps. Johansson et al. reported that only a few patients continued to use the splints for the whole desired period and that the pattern of usage varied significantly.[47] In addition, wearing an occlusal splint or bite guard is known to cause secondary complications such as pain, occlusal discomfort, interferences, etc.[66] Another significant issue with the currently available techniques is that they are primarily designed for the monitoring of SB only. It is highly improbable that patients will be wearing occlusal splints while eating or in the day time. Based on an extensive literature search, there are no standard methods available to monitor and prevent AB, which is even more frequently observed (especially with women) with the currently available approaches.

For edentulous patients with implant supported prosthesis wearing occlusal splints adds more complications to the restoration. In order to monitor through EMG, patients either have to wear headbands at home or go to the hospital for overnight diagnosis. Thus, there is a need of improvement in the

treatment modality of full arch restoration and inclusion of a feedback modality to generate artificial proprioception that may significantly improve the treatment outcomes of the prosthesis.

1.6.2 Selection of Occlusion Scheme

Occlusion schemes play major roles in determining the longevity for the implant supported prostheses. For the full arch fixed implant prosthesis, bilateral balanced occlusion and group function occlusion schemes have been recommended.[67] Bilateral balanced occlusion (BBO) maintains simultaneous anterior and posterior teeth contacts during all excursive movements of the mandible.[56] Since the occlusal forces are distributed evenly in the anterior and posterior regions of the denture teeth, this type of occlusion scheme is well established for the fixed implant prostheses. The selection of the scheme is also dependent on the nature of opposing teeth. If a full arch implant prosthesis is opposed by a complete denture, then BBO is widely used. However, if the prosthesis is supported by natural dentition in the opposing arch then group function occlusion (GFO) (also known as unilaterally balanced occlusion) is recommended.[37] In GFO, the teeth in lateral occlusion come in contact with the working side only.[55] Furthermore, implant protected occlusion (IPO) has been suggested as a means to protect implant supported prostheses. The primary objective of this scheme is to maintain the occlusal load within the physiological and biomechanical limits of the structures. Several modifications from the conventional schemes have been proposed under IPO and are aimed at reducing occlusal force transfer to the implant and bone. For example, $30\% -$

40% of reduction of occlusion table width in the posterior teeth has been proposed by many researchers.[52,67] Other suggested parameters for IPO include implant length, implant diameter, crown-to-implant height ratio, distal cantilever extension ($< 15\ mm$) etc. For implant supported prostheses with full arch restoration mutually protected occlusion (MPO) is also recommended. The MPO includes shallow anterior contacts during excursive movements and posterior contacts in centric relation position. Thus, the posterior disclusion during excursive movements of the mandible protects the posterior teeth from damage.

1.7 Proposed Approach

In this research, an approach to induce artificial proprioception in the mandibular full arch fixed implant prosthesis is proposed. Unlike the currently available approaches, which rely on occlusal bite guard or EMG, a two-axis force sensing mechanism is designed which is an integral part of the prosthesis and will not require any external appliance. The response from the force sensor will be used to monitor the occlusal load in real time and provide biofeedback to the wearer in an attempt to induce artificial proprioception as illustrated in Figure 6.

The measurable quantity of the proposed design is the force generated during mastication. This force is measured based on deformation (sensing variable) obtained by creating a cavity inside a molar tooth. The deformation is sensed via a sensing mechanism outfitted with strain gauge sensors mounted on two sensing structures and is fully encapsulated inside the tooth to avoid occlusal interferences.

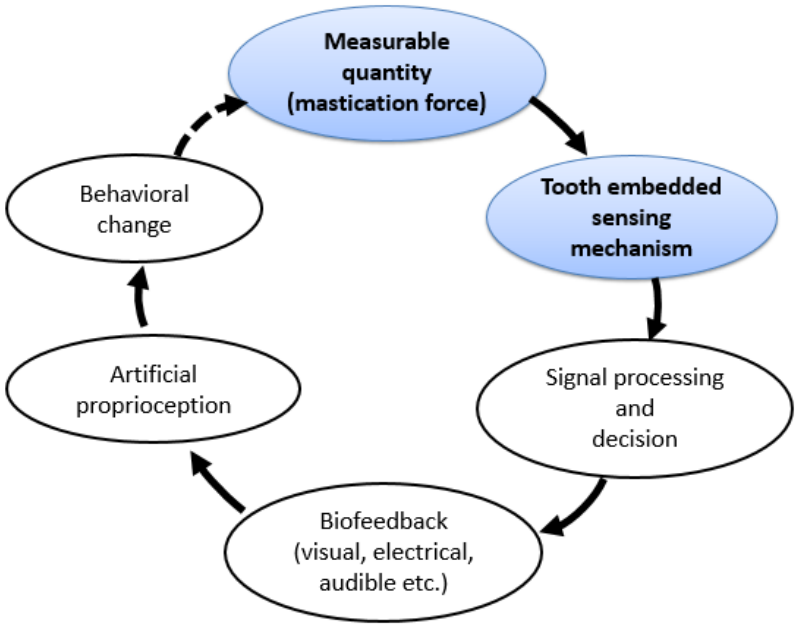

Figure 6: Illustration of the proposed approach to induce artificial proprioception in the full arch fixed implant prosthesis

The tooth embedded sensing mechanism will then be integrated into the complete denture to generate signals in response to the applied mastication loads and frequency ($\sim 1\ Hz$). The associated sensor electronics for signal processing will be incorporated into the available space in the buccal side of the denture. For the power supply, wireless energy transmission or energy harvesting methods may be utilized. To reduce power consumption, the generated signals will be compared with a threshold value, where signals exceeding the preset value will be transmitted wirelessly and received by a receiver module to provide biofeedback. This complete denture integrated sensing mechanism is what is termed as a smart denture, the anatomy of which is shown in Figure 7.

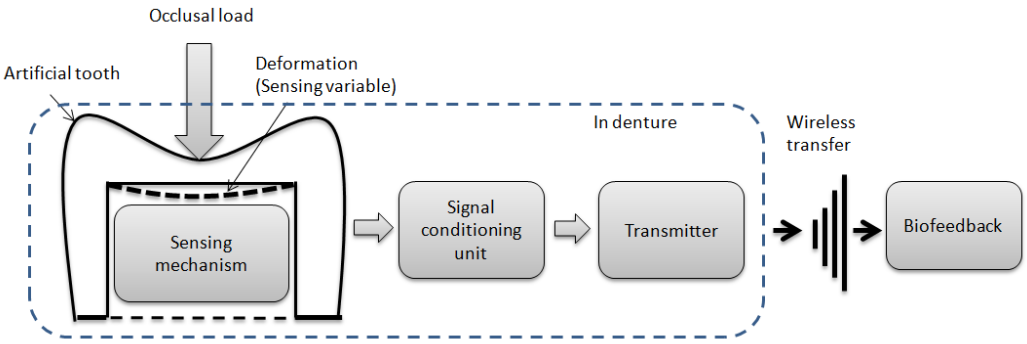

Figure 7. Anatomy of a smart denture

The biofeedback may be provided in terms of visual, audible or electrical stimulations. With the received biofeedback, a patient will be able to perceive or recognize the magnitude and nature (e.g. vertical or horizontal) of the occlusal loads and other conscious or unconscious parafunctional activities. This artificial proprioception or prioprioawareness in terms of the magnitude and direction of the occlusal load may also lead to the change of behavior such as reduced grinding, reduction of mastication force intensity and alleviate parafunctional occlusion symptoms.

Thus, the primary contribution of the present research is conceptualization, design, and development of a tooth embeddable sensing mechanism for full arch prosthesis that will not require any intra-oral occlusal appliance as is observed in the currently available approaches. The functional requirements for the proposed design are that the artificial tooth needs to be able to sustain a $200\ N$ mastication load by fulfilling static (factor of safety of 2 or more) and dynamic reliability criteria (fatigue limit of 10^6 cycles), and the

integrated sensors need to measure both vertical and horizontal forces and exhibit good repeatability under $1\ Hz$ mastication frequency.

1.8 Impact of the Research

The successful implementation of the proposed approach is expected to have a major impact on the lives of edentulous patients with full arch fixed implant restoration in a number of ways:

1. The occlusal overload may be managed more effectively with the proposed approach as compared to the currently available approaches, leading to a reduced degree of maintenance and greater longevity of the prosthesis.

2. Currently, the prostheses are designed based on generalized forces obtained from random individuals during voluntary clenching/biting. However, bite force of an individual is contingent upon several factors such as muscle strength, cranio-mandibular anatomy and neuro-muscular feedback mechanisms.[68] Integration of the proposed approach may enable the practitioners to design customized components for the individual patient based on real clinical data and may facilitate improved treatment plans.

3. Currently, there is no reference database for mastication loads in patients with implant supported prostheses. With the proposed approach, it may be possible to obtain a real-time measurement of the occlusal loads during mastication for the edentulous patients with full arch restoration. The information regarding the vertical and horizontal force components may be utilized to understand the functional and parafunctional loading patterns and to improve prosthetic device design and treatment modalities.

4. Lastly, enabling a method for proprioception will not only improve the quality of lives of edentulous patients but also bring about social and psychological benefits with improved personal confidence.

1.9 Summary

In summary, the first chapter presented the motivation of the research, described the underlying complications experienced by the implant supported prostheses and proposed an approach to address the issues. First, the background of dental prosthesis and associated biological and biomechanical complications are presented. Next, the effects of lack of proprioception and parafunctional habit in the implant supported prostheses are discussed and their positive correlations with occlusal overload are highlighted. Next, available methodologies to provide biofeedback to the patients are presented. Lastly, an approach to induce artificial proprioception in the full arch fixed implant restoration by incorporating a tooth embeddable sensing mechanism is proposed and discussed in light of potential clinical outcomes.

2 Sensing Variable

This chapter presents the biomechanics of artificial dentition and occlusion principles in an attempt to determine a sensing variable (deformation) for the proposed approach. Influences of tooth material and geometric parameters are investigated to obtain a maximum deformation satisfying the static and dynamic failure criteria.

2.1 Denture Tooth Biomechanics and Occlusion Principles

The morphology and biomechanics of artificial dentition are usually quite different than natural dentition. While the natural teeth always appear in anatomic occlusion form, there are generally three types of posterior teeth available for artificial restorations: anatomic teeth, semi-anatomic teeth, and monoplane or non-anatomic teeth.

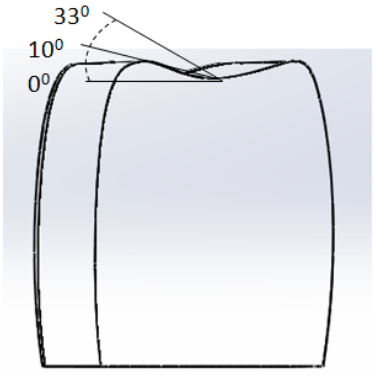

Figure 8: Types of posterior teeth

The teeth forms are defined on the basis of the cusp angle as shown in Figure 8. If the cuspal inclination is $\sim 33\ deg$ then it is called anatomic tooth, and its appearance closely resembles natural dentition.[4] Semi-anatomic teeth can be

$10\ deg$ or $20\ deg$ and are generally used for lingualized occlusion scheme. Monoplane teeth are cuspless teeth ($0\ deg$) and are usually used for monoplane occlusion.

For the proposed approach, available occlusal teeth forms and their relationships with different types of occlusal schemes have been investigated. As discussed in Section 1.6.2, multiple occlusion schemes are available. To begin with, these schemes are purported to have maximum intercuspal contacts in centric positions. However, the biomechanics vary substantially when it comes to excursive (protrusive and lateral) movements of the mandible. During right and left lateral movements, the contacts on the occlusal surfaces are governed by the type of adopted occlusion scheme for the lateral occlusion. Since one of the primary objectives of the proposed design is not to interfere with functional occlusion during mastication or other oral activities, the features of the currently adopted occlusion schemes are studied and described in the context of the proposed design.

Lingualized and conventional balanced occlusions (also known as fully balanced and bilateral balanced occlusion) are two of the most popular ones for complete denture occlusions and are applied to the implant supported prostheses as well.[69,70] Lingualized balanced occlusion scheme is characterized by maxillary lingual contacts with mandibular central fossae in centric working and non-working positions as shown in Figure 9-A.[71] Because of its simplicity, the lingualized balanced scheme is easy to implement and preferred by the practitioners in general.

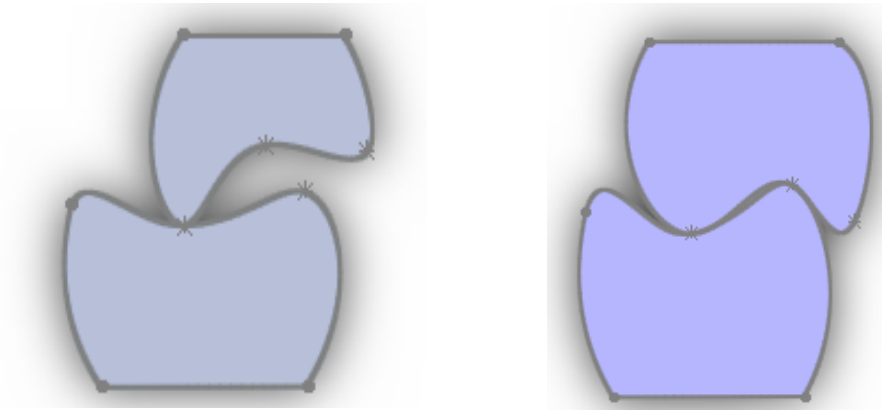

A B

Figure 9: Conventional occlusion schemes in complete denture.

A, Lingualized balanced occlusion scheme. B, Conventional balanced occlusion scheme

Conventional balanced occlusion, on the other hand, is defined as the form of contact arrangement which maintains simultaneous anterior and posterior occlusal contacts in both centric and eccentric mandibular movements as shown in Figure 9-B. Both maxillary lingual and mandibular buccal cusps occlude with the opposing fossae and marginal ridges in this occlusal scheme. As a result, cross tooth balance is observed in the conventional balanced occlusion. The advantage of this type of scheme is that it offers more stability and the forces are evenly distributed among all the teeth in contact.[71] However, it is very difficult to implement this scheme in the clinical setting and requires a lot of dedicated time to perfect. Moreover, the cross tooth balance is susceptible to damage due to lateral loading which is known to be more detrimental to the structural integrity of the prosthesis. Other occlusion schemes such as linear occlusion and

monoplane occlusion are also employed, but they are less common due to lack of proper stability and natural appearance.

For the lateral occlusion, there are three types of schemes which are categorized as: bilateral balanced occlusion, group function or unilateral balanced occlusion, and anterior occlusion (canine guidance and anterior guidance). The bilateral balanced occlusion maintains simultaneous anterior and posterior occlusal contacts during all excursive positions.[70] Group function scheme is defined as multiple contact relations between maxillary and mandibular teeth during lateral movements on the working side. This scheme acts as a group to distribute the occlusal forces in the posterior region and discludes the anterior teeth. Since the load is shared among the posterior teeth, it is considered to be suitable for the fixed implant prostheses. Anterior occlusion, on the other hand, discludes the posterior teeth during excursive movements and occludes with the anterior teeth. Anterior occlusion scheme is of two types: canine guidance and anterior guidance occlusion. In the canine guidance occlusion, the lateral loads are absorbed by the canine itself, whereas in the anterior guidance the loads are shared among the teeth in the anterior region.

Although, several schemes are available for the centric and lateral occlusion schemes, there has not been any consensus among clinicians about which scheme is the best for the fixed and removable prostheses.[55] This is partly because of the fact that various parameters such as number of implants, their axial inclinations, lengths, diameter, quality of supporting bone and ease of construction determine the effectiveness of the selected scheme.[72] As such, the

selection in a clinical situation is usually based on anecdotal clinical experience as opposed to evidenced based conclusion.[67,73,74]

For the proposed approach with tooth embeddable sensor, the lingualized balanced occlusion scheme for the centric occlusion and group function occlusion scheme for the lateral occlusion are selected. Since the loads with the conventional balanced occlusion are distributed in the cusps and central fossae of the mandibular arch, this scheme is not ideal for the proposed sensing approach. Moreover, group function occlusion is selected due to the fact that the sensor is going to be encapsulated inside the 1st molar tooth and contacts need to be established in the posterior region to generate measurable responses.

2.2 Sensing Variable - Deformation

The sensing variable for the proposed design is the deformation inside a tooth (molar) as shown in Figure 10. The deformation is obtained by creating a cavity inside the molar tooth. When the occlusal load is applied on the occlusal surface, the inside surfaces of the tooth deform. The idea is to advantageously utilize these deformations to generate measurable responses without compromising the structural integrity of the tooth and the underlying supporting structures.

The deformations inside the tooth are mainly influenced by three parameters: tooth morphology, tooth material, and size of the cavity. The effects of these parameters are investigated using finite element analysis (FEA) to obtain measurable deformations.

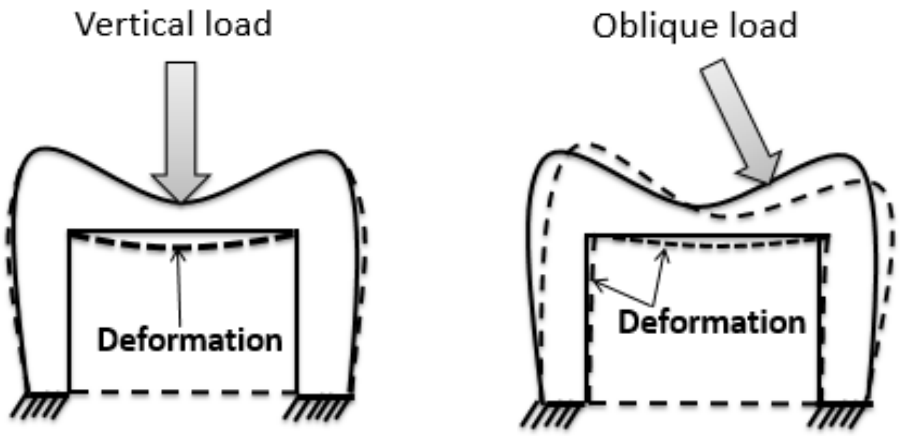

A B

Figure 10: Illustration of deformation profiles for the molar tooth.

A, Under vertical load. B, Under oblique load

2.3 Finite Element Models and Methods

In this section, the molar tooth morphology and geometric dimensions of the developed solid model and its cavity (Subsection 2.3.1), tooth material (Subsection 0), and applied boundary conditions (Subsection 2.3.3) to investigate the effects of material and geometric parameters on the induced deformation inside the tooth cavity are discussed.

The mandibular 1st molar tooth is selected to house the two-axis sensor. Typically, the complete denture for the full arch restoration extends up to the 1st molar tooth, which is known to endure the most load during mastication.[75] Furthermore, the 1st molar is the largest in size among all other teeth in the mandibular arch. A larger tooth provides more space to facilitate sensor housing and integration, and a higher force is important to generate measurable

responses especially in the bucco-lingual direction. The dimensions of all teeth in the mandibular arch are provided in Table 1.

Table 1: Dimensions of mandibular teeth[42]

Mandibular teeth	Mesio-distal length of crown (mm)	Bucco-lingual length of crown (mm)
Central incisor	5.0	6.0
Lateral incisor	5.5	6.5
Canine	7.0	7.5
First premolar	7.0	7.5
Second premolar	7.0	8.0
First molar	11.0	10.5
Second molar	10.5	10.0

2.3.1 Tooth Morphology

The morphology of the artificial molar tooth to be used for FEA and associated dimensions are shown in Figure 11. For the cusp angle, $10\ deg$ inclination is selected since this is the most commonly used tooth form for the lingualized occlusion. The geometric model of the tooth was developed using advanced surface modeling technique in SolidWorks 2013 (Waltham, Massachusetts, USA). An image of a denture molar tooth was imported in SolidWorks and the curved profiles were replicated using 3D sketches. A solid body was formed by filling the enclosed surfaces using fill and knit features. Next,

a cavity was created by Boolean operation (subtract) in an effort to generate deformation at the lower occlusal surface in response to applied load. Figure 11-B shows the developed molar tooth model with the cavity and its dimensions in mesio-distal and bucco-lingual directions.

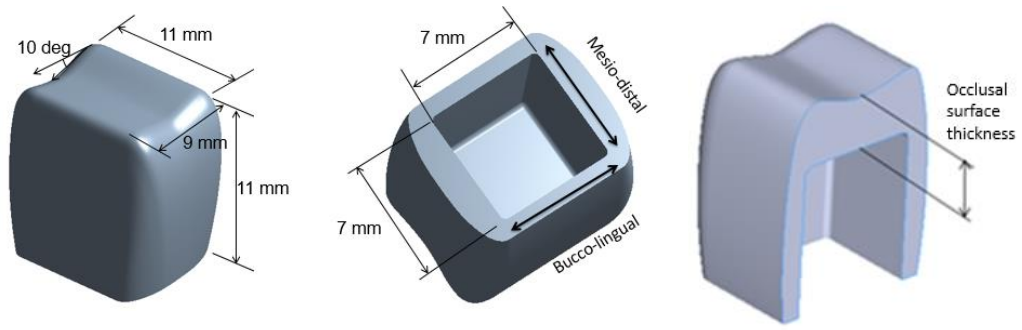

A B C

Figure 11: Molar tooth geometry. A, Solid model with generalized dimensions. B, Dimensions of the cavity. C, Occlusal surface thickness

Next, a finite element parametric model was developed in ANSYS 14.5 (Canonsburg, Pennsylvania, USA) to investigate the effects of geometric parameters and material property (Young's modulus) on the induced deformation inside the tooth cavity: The primary parameters affecting the deformation are tooth material, mesio-distal length, bucco-lingual length, and occlusal surface thickness (Figure 11-C).

2.3.2 Tooth Material

The denture teeth can be fabricated of various materials such as acrylic resin, porcelain, composite resin or gold.[76] About 60% of the artificial teeth in the United States are made of acrylic resin.[77] For the present study, acrylic resin

tooth is selected as the tooth material due to its lower Young's modulus ($2.26\ GPa$) compared to other materials such as porcelain ($70\ GPa$) and composite resin ($14.1\ GPa$).[78] Due to the lower Young's modulus of the acrylic resin tooth, it is expected that under the same load an acrylic resin tooth will undergo a higher deformation as compared to a porcelain or composite resin tooth which is desirable for the proposed design.

2.3.3 Applied Load and Boundary Conditions

A fixed boundary condition was imposed at the bottom surface of the tooth model as shown in Figure 12-A. For the occlusal loading magnitude, a $200\ N$ vertical load was applied as pressure at an area with $0.57\ mm$ diameter at the central fossa of the tooth as shown in Figure 12-B.

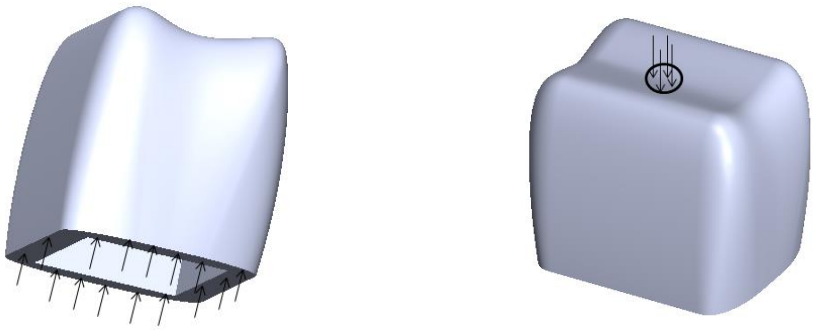

A B

Figure 12: Finite element model setup for the molar tooth. A, Fixed constraint. B, Vertical load applied at the central fossa

Bite forces of individuals vary quite significantly and are contingent upon various factors such as muscle strength, cranio-mandibular anatomy and neuro-muscular feedback mechanisms.[68] According to Mericske-Stern et al., the

average maximum bite force experienced by the 1st molar tooth in fixed implant supported prostheses is $200\ N$.[79] In another study, the maximum bite force in the molar tooth of an implant supported denture was reported to be $160\ N$ (95% confidence interval, $140\ N$ - $180\ N$).[80] Thus, $200\ N$ was considered a reasonable approximation of the highest mastication force magnitude for edentulous patients with full arch fixed implant restoration. Lastly, the load was applied in an area of $1\ mm^2$ to avoid false stress concentration at the load application area. Furthermore, the typical contact area between the antagonist teeth is reported to be $1\ mm^2$ or lower.[81]

Figure 13: Generated mesh for the molar tooth

The next step in FEA pre-processing was to generate a mesh. The generated mesh in the molar tooth using a 10 node tetrahedral element (also known as $SOLID187$ in ANSYS with three translational degrees of freedom for each node in the x, y, and z directions) is shown in Figure 13. This type of element exhibits quadratic displacement behavior and is suitable for modeling irregular geometry. The aspect ratio of the elements was maintained below 3 and a Jacobian of > 0.7 was ensured for improved element quality.[82] Each node of

the $SOLID187$ element has three translational degrees of freedom in the x, y and z directions. The number of elements and nodes in the model were 54864 and 87491 respectively.

2.4 Results and Discussions

In this section, the effects of acrylic resin Young's modulus, mesio-distal and bucco-lingual lengths, and occlusal surface thickness on the induced deformation at the lower occlusal surface are discussed. Based on static and dynamic strength criteria, the mentioned dimensions are finalized to obtain a maximum deformation under the maximum mastication load.

The Young's modulus of the acrylic resin material contributes to the amount of induced deformation. The mechanical properties of acrylics vary considerably depending on the composition, manufacturing technique and environmental conditions.[77] A range of Young's modulus values ($2.26\ GPa$ to $5.31\ GPa$) are documented in the open literature.[77,78,83–85] In order to investigate the effect of acrylic resin Young's modulus on the induced deformation, the modulus of the material was varied from $2.5\ GPa$ to $5.3\ GPa$ at $0.3\ GPa$ increments while keeping other geometric parameters constant.

Figure 14 shows the graph of generated deformation at the lower occlusal surface of the tooth as a function of Young's modulus of acrylic resin material. The results show that the deformation decreases with increasing Young's modulus. A non-linear relationship is observed which is evident from the third order polynomial curve fit equation presented in Figure 14.

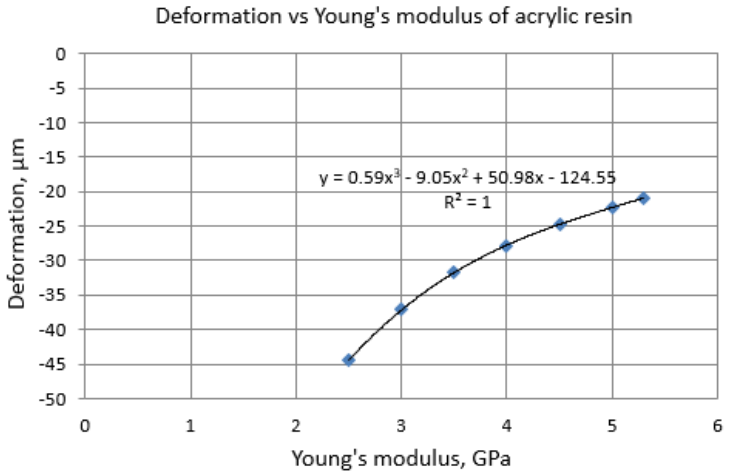

Figure 14: Effect of acrylic resin Young's modulus on the deformation at the lower occlusal surface

The non-linear relationship between the induced deformation and Young's modulus of the acrylic resin may be attributed to the irregular geometry of the tooth structure. The location of the maximum deformation is at the lower occlusal surface as shown in Figure 15.

A B

Figure 15: Deformation profile inside the molar cavity. A, Undeformed view. B, Deformed view (amplified by 25 times for better visualization)

For the present study, an acrylic resin with a lower Young's modulus is desired in order to generate a higher deformation. As such, the Young's modulus

and Poisson's ratio of the acrylic resin were selected to be $2.8\ GPa$ and 0.30 respectively, and the material was considered to be linearly elastic and isotropic.[85]

The effect of mesio-distal length on the induced deformation was evaluated by varying the length from $6.0\ mm$ to $7.0\ mm$ at $0.2\ mm$ increments. The bucco-lingual length and the occlusal surface thickness were defined at $7\ mm$ and $2.9\ mm$ respectively while investigating the effect of the mesio-distal length. The resultant deformation values at the lower occlusal surface are provided in Table 2. According to the analysis, the mesio-distal length does not have significant effect on the induced deformation. For a total $1\ mm$ change of the mesio-distal length the induced deformation changed by 4.9 μm.

Table 2: Deformation at the lower occlusal surface for varying mesio-distal lengths

	Mesio-distal length, mm					
	6.0	6.2	6.4	6.6	6.8	7.0
Deformation, μm	-38.9	-39.9	-40.8	-41.8	-42.8	-43.8

Similarly, the effect of bucco-lingual length on the deformation was evaluated by varying the length from $6.0\ mm$ to $7.0\ mm$ at $0.2\ mm$ increments. While performing the analyses, the mesio-distal and occlusal surface thickness were defined at $7\ mm$ and $2.9\ mm$ respectively. The resultant deformation values

are provided in Table 3. Similar to the effect of mesio-distal length, the change of deformation for a $1\ mm$ change of the bucco-lingual length is $4.9\ \mu m$.

Table 3: Deformation at the lower occlusal surface for varying bucco-lingual lengths

	Bucco-lingual length, mm					
	6.0	6.2	6.4	6.6	6.8	7.0
Deformation, μm	-39.0	-39.9	-40.9	-41.8	-42.9	-43.9

The final dimensions of the cavity in the mesio-distal and bucco-lingual directions were defined as $7\ mm\ x\ 7\ mm$ respectively as the induced deformation is maximum for this cavity size. Since the mesio-distal and bucco-lingual lengths do not affect the deformation significantly, in case the available space is limited due to clinical factors such as implant placement or superstructure construction, these dimensions can be decreased without significantly affecting the induced deformation. However, to ensure measurement accuracy, the sensor calibration equations should be modified accordingly. The principal stresses were also evaluated for all these cases to ensure that they are within allowable range as discussed later in the present section.

Next, the effect of occlusal surface thickness on the deformation at the lower occlusal surface was examined (with Young's modulus of $2.8\ GPa$, mesio-distal length of $7\ mm$, bucco-lingual length of $7\ mm$,and mastication load of $200\ N$). The occlusal surface thickness was varied from $2.0\ mm$ to $4.1\ mm$ at an increment of $0.3\ mm$ and the results are shown in Figure 16. The deformation, as

expected, decreases with increasing occlusal surface thickness. Due to the non-uniform geometric dimensions of the tooth structure, the change of thickness generates a non-linear deformation profile which is evident from the third order polynomial curve fit equation shown in Figure 16. Similar to the effect of Young's modulus, the tooth structure stiffens with increasing occlusal surface thickness A higher deformation is desired for the sensing purpose as this is directly proportional to the sensitivity of the measurement.

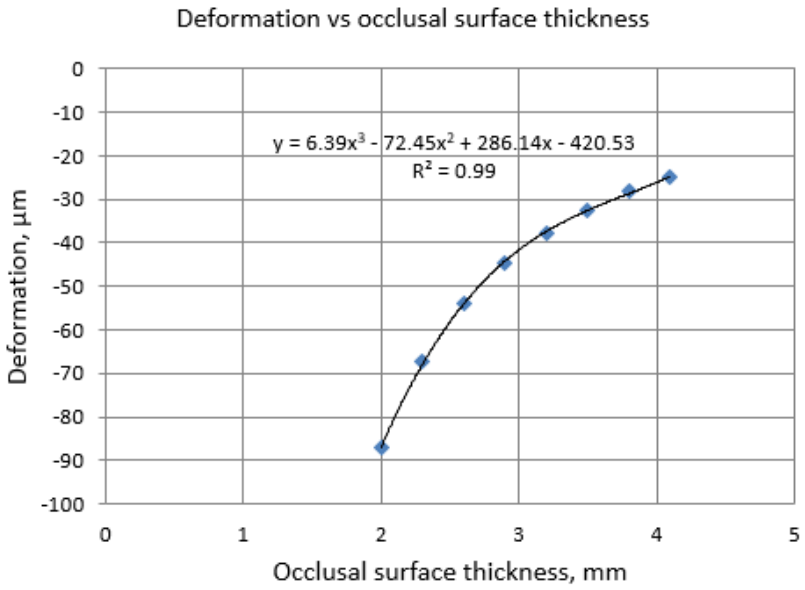

Figure 16: Effect of occlusal surface thickness on the induced deformation at the lower occlusal surface

The selection of the occlusal surface thickness is also based on the induced stresses at the tooth. The maximum and minimum principal stresses are evaluated since the acrylic resin is considered a brittle material.[86] The tensile and compressive strength values may be different and lower than the yield strength of

the material separately. Therefore, to predict failure, evaluation of principal stresses is recommended as the most conservative approach.[76,87]

Figure 17 shows the maximum and minimum principal stress distributions in the tooth as a function of the occlusal surface thickness. The occlusal surface thickness was varied from $2.0\ mm$ to $4.1\ mm$ at $0.3\ mm$ increments and the resultant principal stresses are evaluated from ANSYS. The results show that the induced stresses decrease non-linearly with increasing occlusal surface thickness. The non-linear third order polynomial curve fit equations for the maximum and minimum principal stresses are presented in Figure 17.

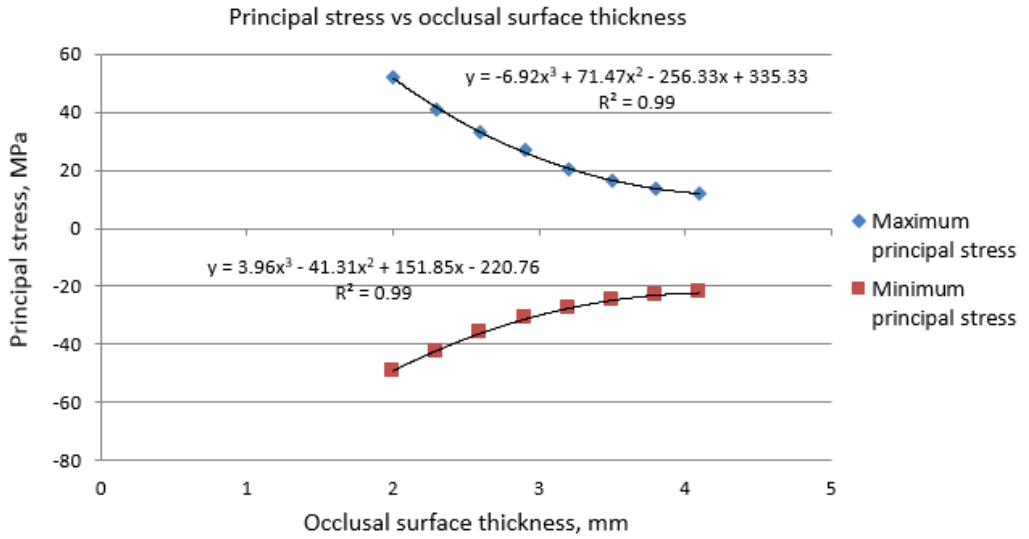

Figure 17: Principal stress at the lower occlusal surface as a function of occlusal surface thickness

The reason for this non-linear behavior is the non-linear deformation profile as a function of the occlusal surface thickness as shown in Figure 16. For the same increment of the occlusal surface thickness, the change of maximum

principal stress is higher than the minimum principal stress. Furthermore, at a lower occlusal surface thickness, the magnitude of the maximum principal stress is higher than the minimum principal stress, and at a higher thickness, the magnitude of the maximum principal stress is lower than the minimum principal stress. In order to predict failure, these stresses are compared with the strength properties of the acrylic resin which vary depending on the composition of the material. The generalized ultimate and compressive strength values of denture based acrylics are $62\ MPa$ and $76\ MPa$ respectively.[77,88] Since the ultimate tensile strength of the acrylic resin is lower than the ultimate compressive strength, and the maximum principal stress is more sensitive to the occlusal surface thickness, the ultimate tensile strength plays a greater role in determining the structural integrity of the tooth under the applied mastication load.

The allowable maximum and minimum principal stresses are determined based on the desired factor of safety. In the present study, a minimum factor of safety of 2 was desired. The factor of safety, N, is calculated according to Modified-Mohr theory (Equation 1). The Modified-Mohr theory is recommended when the ultimate tensile strength of a brittle material is lower than the ultimate compressive strength.[89]

$$N = \frac{S_{ut}|S_{uc}|}{|S_{uc|}\sigma_1 - S_{ut}(\sigma_1 + \sigma_3)} \qquad \text{Equation 1}$$

In Equation 1, S_{ut} is the ultimate tensile strength, S_{uc} is the ultimate compressive strength, and σ_1 and σ_3 are the maximum and minimum principal

stresses respectively. The calculated factor of safety values for the investigated occlusal surface thicknesses are presented in Table 4.

Table 4: Factor of safety for various occlusal surface thicknesses

Occlusal surface thickness, mm	Maximum principal stress	Minimum principal stress	Factor of safety
2	52.00	-49.00	1.25
2.3	41.20	-42.50	1.47
2.6	33.10	-36.13	1.74
2.9	27.01	-31.10	2.04
3.2	20.10	-27.69	2.36
3.5	16.44	-24.95	2.65
3.8	13.91	-23.11	2.90
4.1	11.92	-22.20	3.05

The lowest factor of safety (1.25) is obtained for $2\ mm$ occlusal surface thickness. According to Table 4, as the thickness increases the factor of safety also improves and they are non-linearly correlated based on a third order polynomial equation ($y = -0.17x^3 + 1.52x^2 - 3.44x + 3.43$, where y is the factor of safety and x is the occlusal surface thickness) curve fit with a regression coefficient of 1. The factor of safety for $2.9\ mm$ thickness is estimated to be 2.04 which is close to the desired value of 2 and hence this thickness is defined as the final occlusal surface thickness for the molar tooth with artificial cavity.

The maximum and minimum principal stress distributions for the finalized occlusal surface thickness are shown in Figure 18. The highest tensile stress is located at the center of the lower occlusal surface and the minimum principal stress is observed at the edge of the cavity.

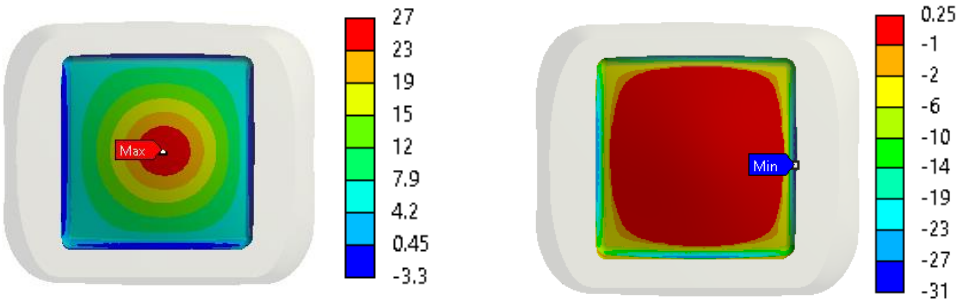

A B

Figure 18: Principal stress (MPa) distributions at the lower occlusal surface. A, Maximum principal stress. B, Minimum principal stress

Using the finalized dimensional specifications, the deformation values are obtained for up to $200\ N$ load at an increment of $20\ N$ as shown in Figure 19. A linear correlation is obtained between the applied load and deformation. Although the effects of tooth material and occlusal surface thickness on the induced deformation are non-linear, the maximum deformation is linearly correlated with the applied load. The correlation equation between the applied mastication load, x, and deformation, y, is presented in Equation 2.

$$y = -0.22x \qquad \text{Equation 2}$$

For the proposed design, a linear relationship between the applied load and deformation is desirable for the sensor calibration method.

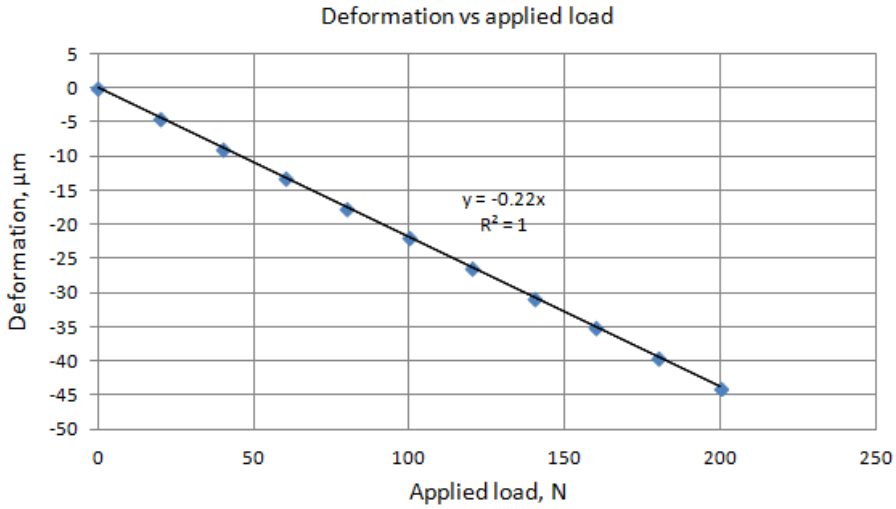

Figure 19: Deformation at the lower occlusal surface as a function of occlusal load applied at $20\ N$ increments

Fatigue failure analysis under dynamic loading was also performed. Due to fatigue, the tooth might fail at a much lower stress than defined by the static failure criterion. The average number of times a person chews/masticates in a year is approximately five hundred thousand.[90] As such, the molar tooth needs to sustain an average of 1 million repeated stress cycles in a year which may change based on the experienced occlusal load in the prosthesis during functional and parafunctional occlusions. In the literature, various failure strength values of acrylics are reported based on the material composition. For instance, Koichi reported that a heat cured pure PMMA has a fatigue limit of $22.35\ MPa$ at 10^6 cycles.[90] In another study, Salih et al. reported that the fatigue strength of a PMMA composite (PMMA-5% Glass fiber-3% nHA) is $38\ MPa$.[91] Since the mean stress ($(\sigma_{max} + \sigma_{min})/2 = (27 + 0)/2\ = 13.5\ MPa$) under the present design

specifications and applied occlusal load is below $22.35\ MPa$, the tooth may be able to sustain 10^6 cycle reliably.

2.5 Summary

In this chapter, various posterior teeth forms and occlusion schemes of the implant supported prostheses are discussed. Considering the occlusal biomechanics and the maximum mastication load, the 1st molar tooth is selected for the embedded sensor design. A cavity is created inside the molar tooth and the deformation of the lower occlusal surface is defined as the sensing variable for the proposed approach. Acrylic resin (linear and isotropic) is selected as the tooth material. Next, effects of acrylic resin Young's modulus and various geometric parameters associated with the cavity are investigated using FEA to obtain a maximum deformation under the $200\ N$ mastication load without compromising the structural integrity of the tooth. The dimensions of the cavity are $7\ mm\ x\ 7\ mm$ and the occlusal surface thickness is $2.9\ mm$. The maximum and minimum principal stresses for the finalized dimensions are $27\ MPa$ and $-31\ MPa$ respectively. The tooth model has a static factor of safety of 2.04 and is expected sustain at least 10^6 cycles of dynamic loading.

3 Sensing Mechanism

This chapter presents the design of the sensing mechanism. To measure the deformation at the lower occlusal surface, various sensor technologies were considered. The primary constraint for the selection was size. Based on the tooth dimensions, the maximum available space for the sensor integration inside the tooth is ~ $7\ mm\ x\ 7\ mm\ x\ 8\ mm\ (L\ x\ W\ x\ H)$. Furthermore, the maximum mastication load is set at $200\ N$ and the frequency of the applied load during functional occlusion is ~$1\ Hz$.

The first consideration was MEMS (Micro-Electro-Mechanical Systems) force/pressure sensors because of their small size (micrometers to millimeters), high sensitivity and precision. However, the overall dimensions of these sensors can be large after packaging.[92] Chen et al. reported three commercially available MEMS pressure sensor packaging dimensions: Freescale ($7.4\ mm\ x\ 7.4\ mm\ x\ 3.9\ mm$), Metrodyne ($7.0\ mm\ x\ 7.0\ mm\ x\ 4.0\ mm$), and Bosch ($8.4\ mm\ x\ 6.9\ mm\ x\ 4.6\ mm$).[93] Although the Metrodyne packaging dimensions satisfy the mentioned space constraints, this is the size of a single sensor only. In the present study, at least two sensors are required to measure the vertical and horizontal force components of the mastication load. Piezoelectric sensors do not need external excitation and offer high sensitivity. However, they require an additional component such as charge amplifier for the measurement, and therefore the size of the total system becomes larger. The smallest commercially available piezoelectric pressure transducer by Kulite Semiconductor is $22.86\ mm$ long, $4.82\ mm$ diameter and has a small sensing area ($\Phi 2.52\ mm$).[94] Another

type of sensor called force sensing resistor (FSR) was also considered. FSR sensors are based on the change of resistance in response to applied force or pressure. These sensors have small sensing area ($\Phi 3.81\ mm$), but with the associated substrate the overall size increases ($\Phi 7.6\ mm$).[95] Furthermore, they are known to suffer from poor repeatability.[96,97]

Although various sensor technologies are available, the primary challenge lies in designing the approximate structure/sensing mechanism on which these sensors will be attached to measure the forces in two directions (vertical and horizontal) and within the bounds of spatial constraints. If the requirement was to measure the vertical load only, then the design of the sensing element would have been relatively easy. However, measurement of occlusal forces in the vertical and horizontal directions in response to the applied load in the entire occlusal surface (central fossa to $2\ mm$ offset in the cusp) necessitated research towards the design of a sensing mechanism.

For the present study, a strain gauge sensor was selected as the sensing element. Strain gauge sensors have wide sensing range, good sensitivity, and are available in small sizes that satisfy the spatial constraints of the tooth cavity.[92] A sensing mechanism is designed that can incorporate two strain gauge sensors to measure both vertical and horizontal force components of the applied mastication load. As such, the proposed sensing mechanism has two components: vertical force sensing structure and horizontal force sensing structure. The design of the two force sensing structures is shown in Figure 20.

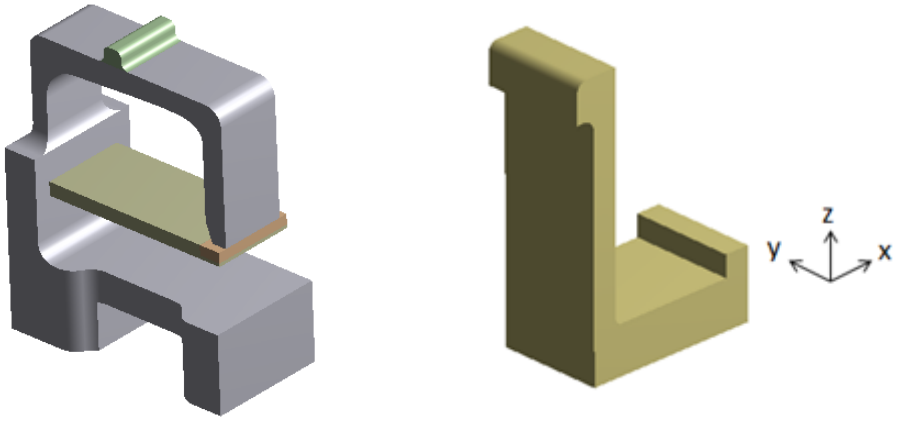

A B

Figure 20: Sensing mechanism. A, Vertical force sensing structure. B, Horizontal force sensing structure

The vertical force sensing structure, shown in Figure 20-A, is designed to measure the load applied perpendicular (z-direction) to the occlusal plane. The horizontal force sensing structure, on the other hand, is designed to measure the load applied parallel to the occlusal plane (x-direction) as shown in Figure 20-B. Figure 21-A shows the assembly of the two sensing structures and Figure 21-B shows the total sensing mechanism incorporated inside the molar tooth. The vertical structure is placed in the mesio-distal direction and the horizontal structure is placed in the bucco-lingual direction of the complete denture construction in the full arch fixed implant prosthesis. In the remaining subsections, the geometrical and design features of the sensing mechanism, design constraints, influencing parameters and comprehensive analyses to define the dimensional specifications are discussed.

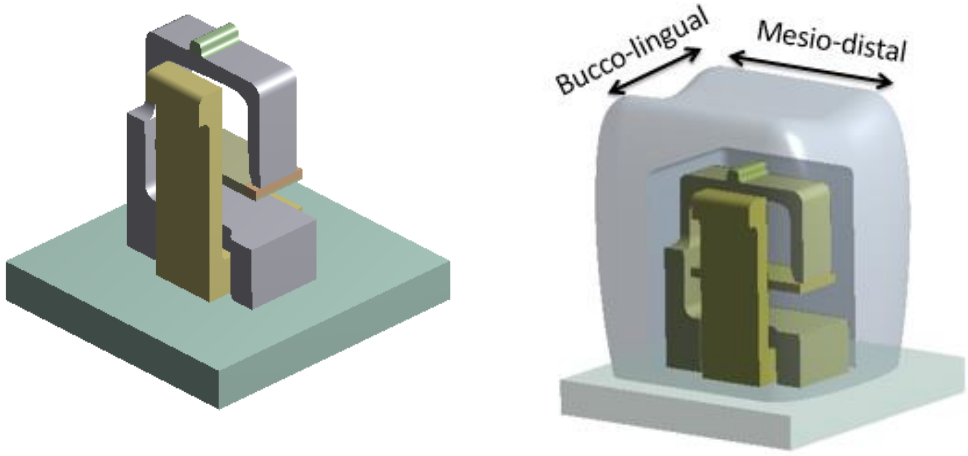

A B

Figure 21: Tooth embedded sensing mechanism. A, Assembly of vertical and horizontal force sensing structures. B, Full assembly of the sensing mechanism integrated inside the molar tooth

3.1 Vertical Force Sensing Structure

This section presents the design overview of the proposed vertical force sensing structure in Subsection 3.1.1, where the description of the geometric features of the sensing structure and how the dimensional specifications are defined to maximize the induced strain are discussed. Static and dynamic stress analyses to evaluate the structural integrity of the sensing structure are presented in Subsection 3.1.2.

3.1.1 Design Overview

The design of the vertical force sensing structure is based on deformation. As discussed in Chapter 2, a cavity is created inside the tooth in order to induce deformation at the lower occlusal surface. The structure is

designed to utilize this deformation to generate a measurable strain and to serve as a mounting structure for the strain gauge sensing element. Since the induced maximum deformation is small ($42\ \mu m$), the effects of various geometric dimensions of the sensing structure were investigated to amplify the deformation and increase the range of measurable strain.

The proposed concept of the vertical force sensing structure is shown in Figure 22. The design consists of two cantilever beams where the 1st cantilever beam is used to amplify the deformation at the lower occlusal surface, and the 2nd cantilever beam on which the strain gauge is mounted utilizes the amplified deformation.

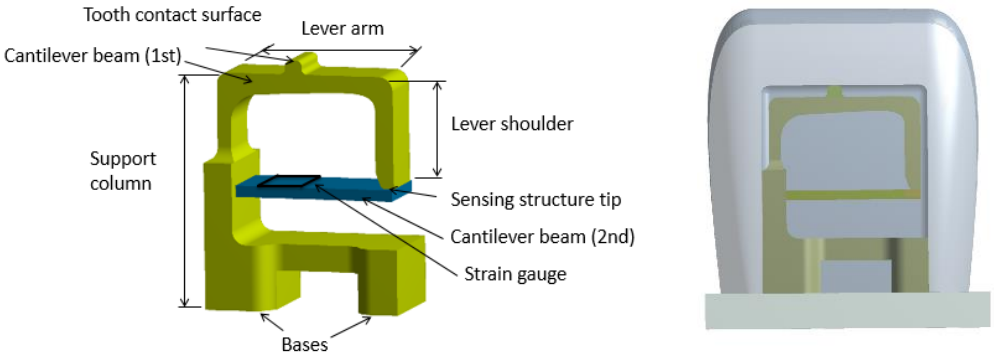

Figure 22: Design of the vertical force sensing structure. A, Labeling of the geometric features. B, Transparent view with the structure incorporated inside the tooth

The design objectives, influencing parameters and design constraints for the vertical force sensing structure are summarized in Figure 23. The primary objective was to generate a maximum measurable strain which is directly related

to the deformation. Therefore, the dimensions of the sensing structure were defined to maximize the deformation at the lower occlusal surface. The extent of the maximum achievable deformation is governed by material property and geometric dimensions of the sensing structure.

The material of the sensing structure is a key design parameter that affects the level of the induced deformation. However, the option is limited due to the availability of biocompatible materials. For the proposed design, titanium alloy ($Ti-6Al-4V$) is selected as the sensing structure and cantilever beam material due to its biocompatibility and widespread use in biomedical (e.g. dental) applications.[98,99]

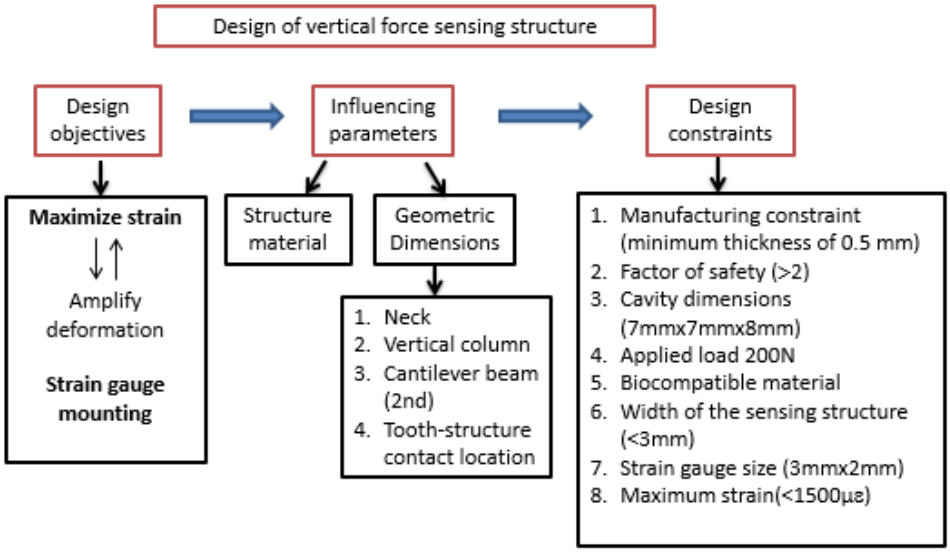

Figure 23: Diagram showing the design objectives, influencing parameters and constraints for the design of the vertical force sensing structure

With the material of the sensing structure defined, the effects of the geometric parameters were investigated to maximize the deformation. First, the

effect of tooth and sensing structure contact location on the deformation at the sensing structure tip was investigated. Figure 24 shows the developed solid model, applied load and boundary conditions for the finite element analysis. $Tet10$ and $Hex20$ elements were used for the mesh generation and at least two elements were maintained across any cross section of the structure. The quality of the elements was also ensured by maintaining an aspect ratio below 3 and a Jacobian of > 0.7 for at least 95% of the elements. The same elements were used for all the FEA analyses in the remaining sections of this chapter.

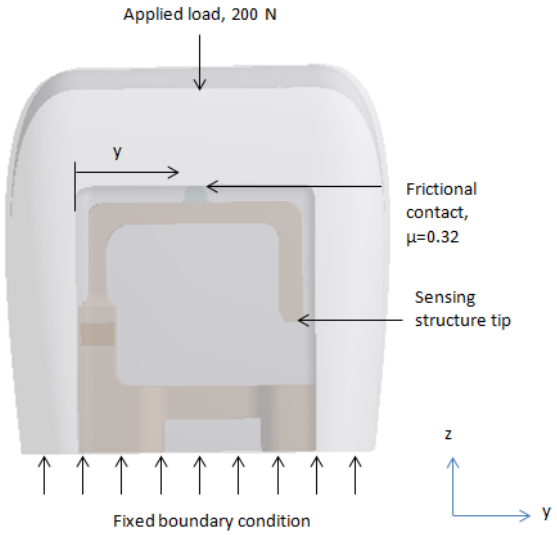

Figure 24: Developed solid model to investigate the effect of tooth and sensing structure contact location on the induced deformation at the vertical force sensing structure tip

The contact location distance, y, defined as the distance from the tooth side wall to the point of contact between the tooth and sensing structure in the y direction, was varied from $1.4\ mm$ to $3.3\ mm$ at an increment of $0.4\ mm$ as shown

in Figure 24. The interface between the tooth and sensing structure is defined as a frictional boundary condition with a friction coefficient of 0.32.[100] For the frictional analysis, the two contacting surfaces are defined as contact and target faces and the friction coefficient is assigned between the contacting elements. The resultant deformations at the sensing structure tip are plotted as a function of the contact location distance as shown in Figure 25.

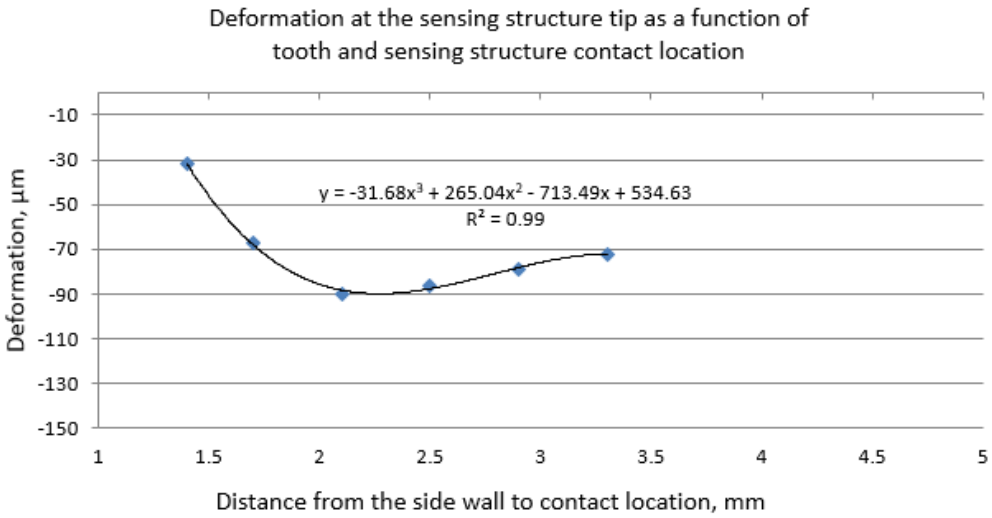

Figure 25: Effect of tooth and sensing structure contact location on the deformation at the sensing structure tip

A non-linear relationship is observed for the induced deformation as a function of the tooth and sensing structure contact location which is evident from the third order polynomial curve fit presented in Figure 25. The graph shows that the deformation increases initially as the distance of contact location from the support column increases. However, as the contact moves further away from the support, the deformation starts to decrease. This is because the deformation at

the lower occlusal surface is maximum at the center of the tooth, and at the sensing structure tip is maximum for contact location near the support column. Therefore, the maximum deformation at the sensing structure tip is expected for contact location somewhere between the center of the tooth and near the support column. According to the analysis, the maximum deformation was obtained for the contact location at $2.1\ mm$ away from the support column and was established as the final contact interface location between the tooth and sensing structure. The maximum von-Mises stress at the sensing structure neck was also evaluated for all the analyzed contact locations and was below the yield strength of the titanium.

With the defined contact location between the tooth and sensing structure, effects of geometric dimensions of the sensing structure on the resultant deformation were investigated. Since Young's modulus of the titanium material is 37 times higher than the acrylic resin, the 1st cantilever beam provides resistance to the input deformation at the lower occlusal surface. Consequently, the beam support column dimensions were modified to provide compliance to the structure. The support column is divided into two regions: vertical column and neck as shown in Figure 26. The neck is introduced to facilitate greater mechanical amplification of the input deformation, and the vertical column is to hold the 2nd cantilever beam and establish contact with the tooth side wall. The dimensional specifications of these two regions are decided based on resultant deformation and induced stress at the sensing structure neck.

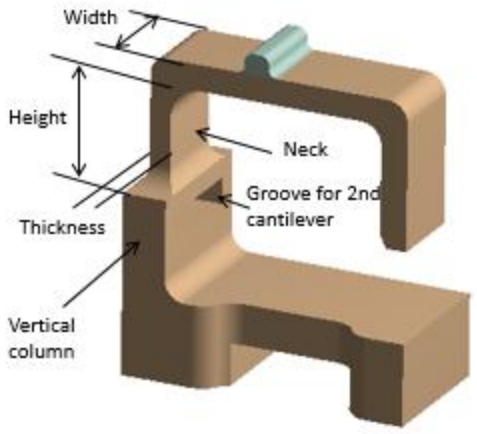

Figure 26: Vertical force sensing structure showing vertical column and neck height, thickness, and width

The thickness of the structure at any location is maintained at a minimum of $0.5\ mm$ for ease of fabrication and fillets with a minimum radius of $0.2\ mm$ are provided in various sections of the model to avoid stress concentration and especially during FEA. The vertical column is designed to be thicker and wider than the neck of the structure to ensure that there is no relative movement during loading and the incorporated cantilever beam (2nd) has a rigid support. The height of the vertical column is $\sim 4.5\ mm$, where $\sim 2\ mm$ is allocated for the base and $\sim 2.5\ mm$ is allocated for the 2nd cantilever beam mounting. Note that these dimensions are defined based on the $8\ mm$ cavity height. However, in the clinical setting, the available height may change due to factors such as prosthetic framework construction and implant location. In case the height of the cavity is reduced, the heights of the vertical column and bases can be adjusted without compromising the original design intended performance.

Next, finite element models were developed to study the effects of the sensing structure neck dimensions (thickness, height and width) on the induced deformations at the sensing structure tip. First, solid models of the sensing structure were developed with $1.9\ mm$, $2.2\ mm$ and $2.5\ mm$ neck heights. The neck height of the vertical force sensing structure is shown in Figure 26. The applied load and boundary conditions were similar to the previous analysis illustrated in Figure 24. The resultant deformations and maximum stress values are presented in Table 5. The location of the maximum von-Mises stress is at the neck of the structure (to be discussed in Section 3.1.2).

Table 5: Maximum deformation and von-Mises stress at the vertical force sensing structure for varying neck heights

Neck height (mm)	Sensing tip deformation (μm)	Maximum von-Mises stress (MPa)
1.9	-84	234
2.2	-86	204
2.5	-87	169

As shown in Table 5, the height of the neck was not found to affect the deformation significantly. However, it affects the generated stress; the smaller the height, the higher the stress at the neck. The minimum stress and maximum deformation were observed for $2.5\ mm$ height and hence defined as the neck dimension. Comparing the maximum von-Mises stress ($169\ MPa$) for the defined

neck dimension with the yield strength of the titanium alloy ($825\ MPa$), the factor of safety is calculated to be 4.88.

Similarly, for the width of the structure at the neck region, three different dimensions ($2\ mm$, $2.75\ mm$ and $3.5\ mm$) were investigated using FEA with similar boundary conditions and applied load shown in Figure 24. The resultant deformation at the sensing structure tip and maximum von-Mises stress at the neck are presented in Table 6. The maximum deformation is obtained for $2\ mm$ width and is defined as the sensing structure width. Although the von-Mises stress is higher at this width, the magnitude is well below the yield strength of the titanium (factor of safety, 4.88) as discussed in Section 3.1.2. Another reason for the selection of this width is to create space for the horizontal force sensing structure.

Table 6: Maximum deformation and von-Mises stress at the vertical force sensing structure for varying neck widths

Neck width (mm)	Sensing tip deformation (μm)	Maximum von-Mises stress (MPa)
2	-87	169
2.75	-84	160
3.5	-81	151

Next, effects of 2nd cantilever beam dimensions on the induced strain were investigated. The cantilever beam is a separate component and is to be

assembled with the body of the vertical force sensing structure once the sensing element is mounted on it. The sensing structure has a groove cut in the vertical column for the assembly as shown in Figure 26. The length of the beam is limited by the mesio-distal length inside the tooth and the width of the beam is selected based on the sensing element width ($2\ mm$). Lastly, the thickness of the beam is an important parameter which not only affects the output strain but also the level of deformation amplification.

The theoretical strain in a cantilever beam can be obtained from simple beam theory and beam deflection formula. The deflection, $s(x)$, at any point in the cantilever beam due to a point load applied at the tip of the beam is given by Equation 3.[101]

$$s(x) = \frac{P}{6\,E\,I}(2L^3 - 3L^2x + x^3) \qquad \text{Equation 3}$$

In Equation 3, P is the force, x is the distance of any section from the free cantilever end, E is the Young's modulus, L is the cantilever beam length, and I is the area moment of inertia. Using beam bending formula and generalized Hook's law, the strain at any location along the cantilever beam is estimated using Equation 4.

$$\varepsilon(x) = \frac{6s(0)c(L-x)}{2L^3 - 3L^2x + x^3} \qquad \text{Equation 4}$$

In Equation 4, c is the distance from the neutral axis to the outermost surface of the beam and $s(0)$ is the deformation at the free cantilever beam end transferred from the sensing structure tip. According to Equation 4, the strain at

any location is proportional to both input deformation and beam thickness. As such, to investigate the effects of cantilever beam thickness and input deformation on the resultant strain, finite element models were developed with varying cantilever beam thicknesses. The applied load and boundary conditions are shown in Figure 27. The friction coefficient at the contact interface between the sensing structure tip and cantilever beam was defined at 0.30.[102] The beam thickness was varied from $0.25\ mm$ to $0.60\ mm$ at an increment of $0.05\ mm$ $(50\ \mu m)$.

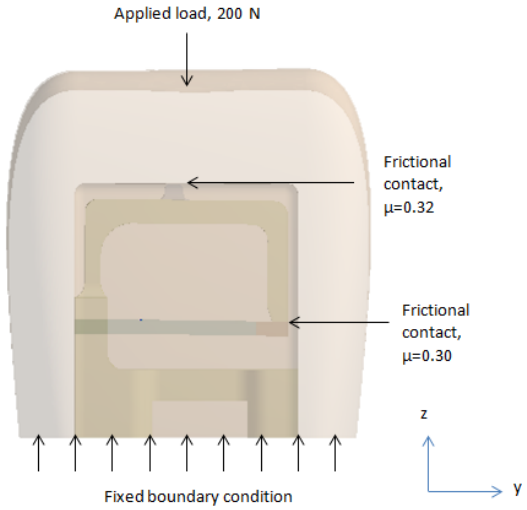

Figure 27: Applied load and boundary conditions to investigate the effect of cantilever beam thickness on the resultant normal strain at the strain gauge sensor location

The resultant deformations evaluated at the sensing structure tip are shown in Figure 28. The deformation decreases non-linearly with increasing cantilever beam thickness which affects the area moment of inertia. The

maximum deflection of a cantilever beam with an input load at the free end is inversely proportional to the area moment of inertia which is a function of beam width and thickness for a rectangular cross section. This inverse relationship explains the non-linear behavior between the deformation and cantilever beam thickness. The data points are best fit with a third order polynomial equation which also corroborates that a non-linear relationship exists between the deformation and occlusal surface thickness.

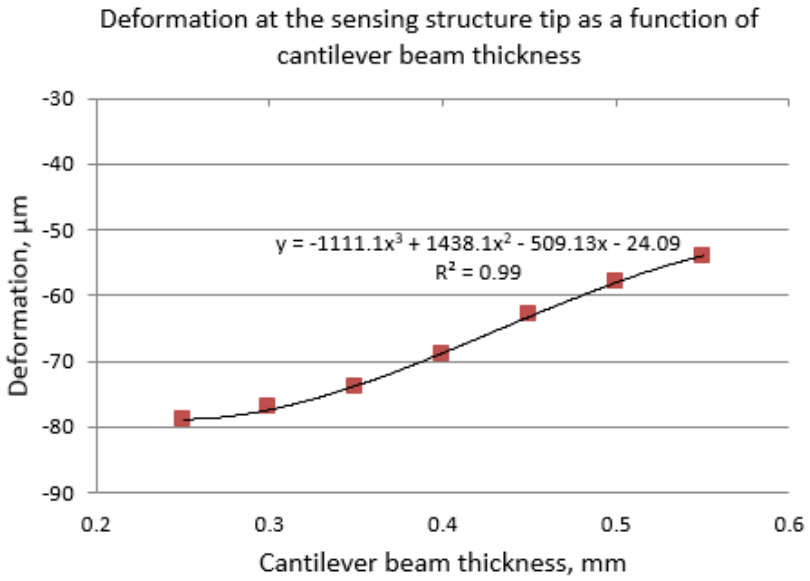

Figure 28: Resultant deformation at the sensing structure tip as a function of cantilever beam thickness

The strain values at the anticipated sensor location ($0.5\ mm$ from the vertical column support) are shown in Figure 29. The induced strain and cantilever beam thickness are also non-linearly correlated according to the curve

fit equation presented in the figure (Figure 29).The strain increases initially with increasing cantilever beam thickness.

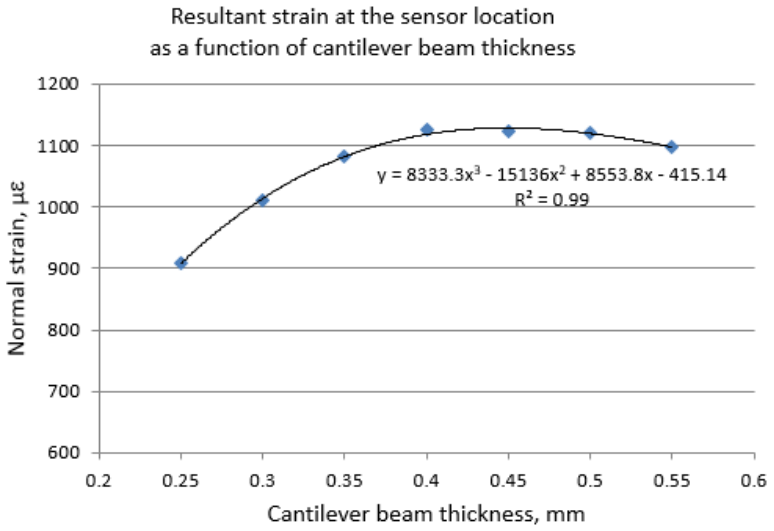

Figure 29: Induced strain at the strain gauge sensor location as a function of cantilever beam thickness

The increase of strain is observed up to $0.4\ mm$ thickness and then it starts to reduce. The non-linear behavior is due to the combined effect of cantilever beam thickness and deformation at the sensing structure tip as illustrated in Equation 4 Since the primary design objective of the vertical force sensing structure is to maximize the generated strain, the $0.4\ mm$ thickness is defined as the final cantilever beam thickness.

The proposed sensing structure can be fabricated using additive manufacturing technology. The use of additive manufacturing to fabricate safe, biocompatible titanium alloy implants has already proven to be successful in in-vitro and in-vivo studies.[98]

3.1.2 Stress Analysis

Stress analysis was performed to evaluate the structural integrity of the vertical force sensing structure. The mechanical properties of titanium alloy ($Ti-6Al-4V$) are presented in Table 7.[103]

Table 7: Mechanical properties of titanium alloy ($Ti-6Al-4V$)

Mechanical property	Magnitude (MPa)
Modulus of elasticity	101,000
Yield strength	825
Fatigue strength (10^7cycles)	598

The analysis was performed using the final defined values of the sensing structure design; contact location $2.1\ mm$ from the vertical column, neck height $2.5\ mm$, neck width $2\ mm$, and cantilever beam (2nd) length $5.7\ mm$, width $2.5\ mm$, and thickness $0.4\ mm$. The maximum von-Mises stress distribution is shown in Figure 30. Since titanium (both pure and alloy) is a ductile material, the maximum von-Mises stress was evaluated for the failure analysis.[104,105] The maximum stress ($164\ MPa$) is located at the neck of the sensing structure as shown in Figure 30. Comparing this value with the yield strength of titanium (Table 7), the static factor of safety is calculated to be ~5. Thus, it is concluded that the design will be able to sustain the maximum amount of occlusal load quite reliably.

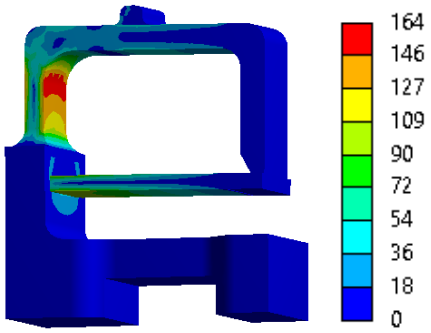

Figure 30: Maximum von-Mises (MPa) stress in the vertical force sensing structure

The structural integrity of the vertical force sensing structure under fatigue loading is also an important design requirement. Due to dynamic nature of mastication, an average of 1 million cycle loads may be experienced by the denture tooth every year.[90] Under dynamic loading, structures tend to fail due to fatigue and the fatigue stress levels may be considerably lower than those defined by static failure criteria. In the present study, stress-life (S-N) approach is used for the fatigue analysis. The fatigue limit of the titanium alloy used for the proposed design is $598\ MPa$ at 10^7 cycles. The mean stress $(\sigma_{max} + \sigma_{min})/2$ calculated from the analysis is $82\ MPa$. Since the stress is well below the fatigue limit, the structure is expected to sustain at least 10^7 stress cycles.

3.2 Horizontal Force Sensing Structure

This section presents the design overview of the proposed horizontal force sensing structure in Subsection 0, and static and dynamic stress analyses to ensure the structural integrity of the structure are discussed in Subsection 3.2.2.

3.2.1 Design Overview

The horizontal force sensing structure was designed to utilize the sideways movement of the tooth due to oblique loading. Figure 31 shows the solid model of the horizontal force sensing structure and the structure incorporated inside the tooth.

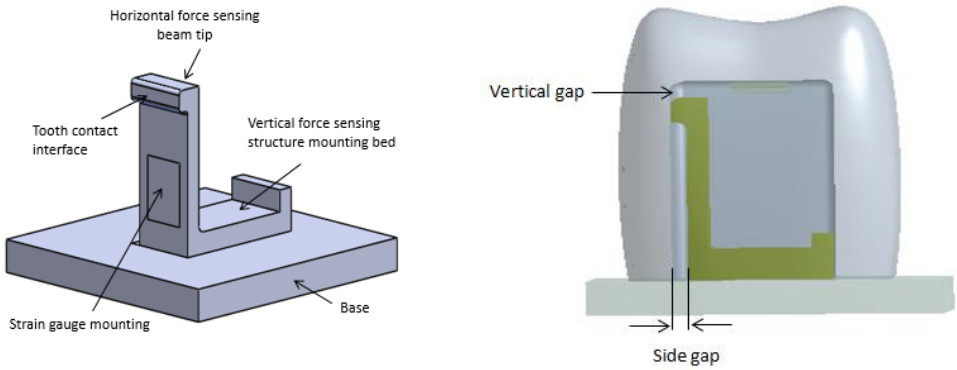

A B

Figure 31: Horizontal force sensing structure design. A, Labeling of the geometric features. B, Transparent view of the encapsulated structure inside the molar tooth

Similar to the vertical force sensing structure design, the primary objectives of the horizontal force sensing structure were to generate a measurable strain and mount a strain gauge sensing element. The design objectives, influencing parameters and design constraints of the horizontal force sensing structure are illustrated in Figure 32.

The working principle of the horizontal force sensing structure is bending strain in the horizontal cantilever beam which has a contact interface with the tooth side wall. The parameters that influence the induced strain at the beam due

to oblique loading are material and dimensions of the beam. The same material ($Ti-6Al-4V$) as the vertical force sensing structure is selected for the horizontal force sensing structure.

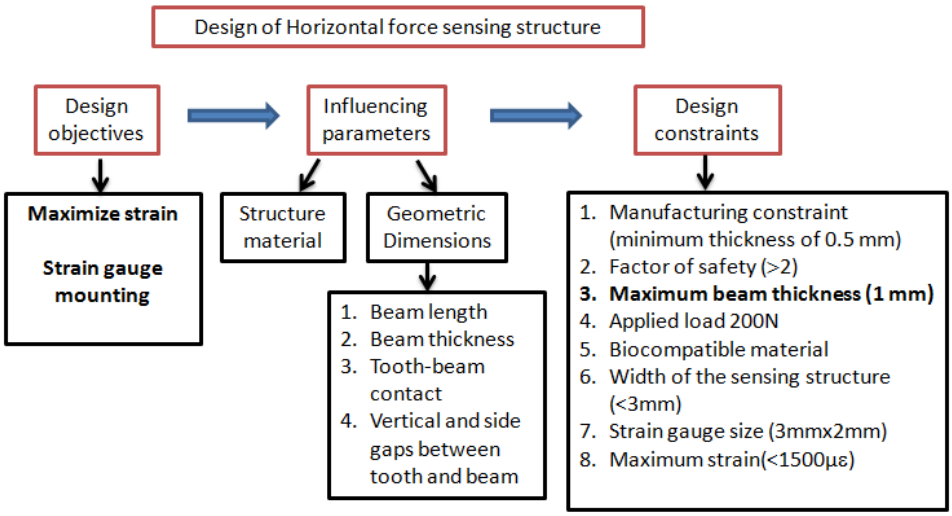

Figure 32: Diagram of the design objectives, influencing parameters and constraints for the design of the horizontal force sensing structure

For the dimensional specifications, the width of the beam is defined as $3\ mm$ considering that the dimensions of the strain gauge sensing element are $3\ mm$ x $2\ mm$. Since the vertical force sensing structure width is $3\ mm$ in the bucco-lingual direction, the available space to incorporate the horizontal force sensing structure on either side of the vertical force sensing structure is limited to $2\ mm$. In the present study, the sensing structure was incorporated on one side of the cavity. However, the design has the flexibility to incorporate sensing structures on both buccal and lingual sides of the tooth, which may be beneficial to investigate mastication load patterns during lateral occlusion and for patients with parafunctional habits.

Assuming that a minimum clearance of $1\ mm$ is required for the strain gauge mounting on the horizontal structure and to avoid interference between the vertical and horizontal force sensing structures during lateral deformation due to the oblique loading, the maximum beam thickness is limited to $1\ mm$. Effect of horizontal cantilever beam thickness on the induced strain was investigated using FEA. The developed solid model for FEA and the boundary conditions are shown in Figure 33. A $200\ N$ oblique load ($30\ deg$) was applied at $2\ mm$ offset from the center of the occlusal surface. The load was applied at an area of $1\ mm^2$to avoid false stress concentration.

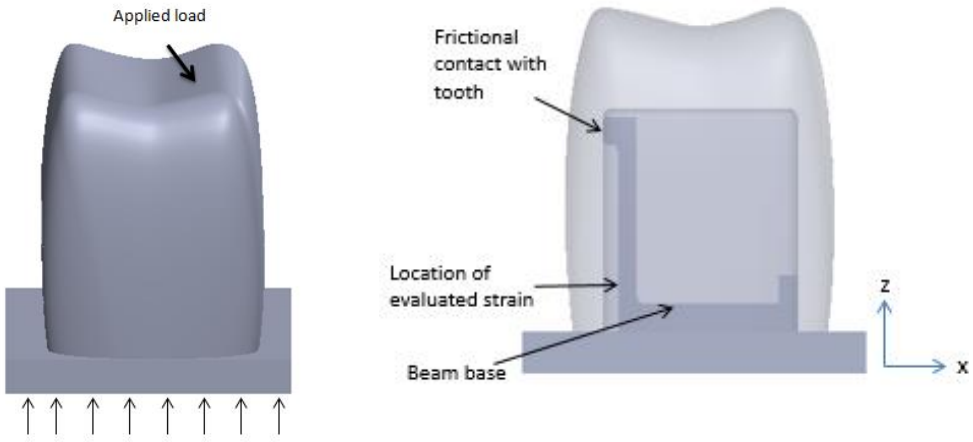

A B

Figure 33: Developed solid model with horizontal force sensing structure. A, Applied oblique ($30\ deg$) load and boundary conditions. B, Frictional contact location with the tooth side wall

The strain values were obtained at the strain gauge sensor location which is defined at $0.5\ mm$ away from the base as shown in Figure 33. The resultant

strain values as a function of the beam thickness are shown in Figure 34. The strain increases with increasing beam thickness. As the load is applied on the cusp at an angle it is decomposed into vertical and horizontal force components. Since this horizontal force component causes the tooth to deform in the x direction, the sensing beam experiences a positive (tensile) normal strain at the sensor location. Although a higher strain is desired, the final thickness is defined as $0.7\ mm$ to maintain a side gap between the beam and tooth side wall. This gap is required for the strain gauge integration in the structure and may be adjusted depending on the available space. Similarly, a vertical gap is maintained between the top of the beam and lower occlusal surface in order to ensure that there is no contact when a vertical load is applied on the occlusal surface.

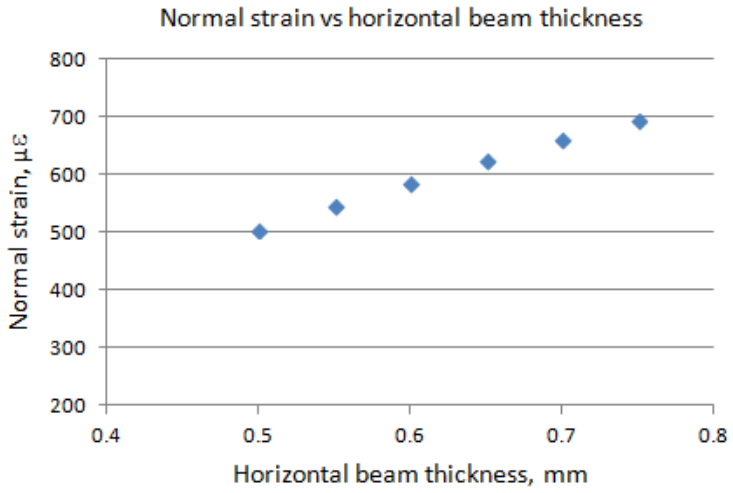

Figure 34: Effect of horizontal beam thickness on the induced strain at the horizontal force sensing structure

The length of the beam from the base to the tooth and sensing structure contact location in the side wall is another important factor that influences the

resultant strain in the horizontal force sensing beam. The longer the length, the higher the strain. However, the selection of this length is governed by the available cavity height and the vertical force sensing mechanism. Considering the $8\ mm$ cavity height in the present design, the length of horizontal force sensing structure from the base to the contact location is defined at $6.5\ mm$.The strain gauge is mounted near the base where the maximum strain is induced due to bending.

Overall, a conservative approach was followed to define the dimensions of the sensing structure. If the available space is further limited due to clinical conditions such as reduced occlusal table width and superstructure positioning, the dimensions of the sensing structure can be modified to satisfy the design requirements.

3.2.2 Stress Analysis

Similar to the vertical force sensing structure, stress analysis was performed in the horizontal force sensing structure to ensure that the induced stresses do not exceed the yield strength of the material. The boundary condition and the input displacement in the model are presented in Figure 33. The analysis was performed with the finalized dimensions of the structure; beam length (from the base to the contact location) $6.5\ mm$, beam thickness $0.7\ mm$, and beam width $3\ mm$. The maximum von-Mises stress distribution in the horizontal force sensing structure is shown in Figure 35.

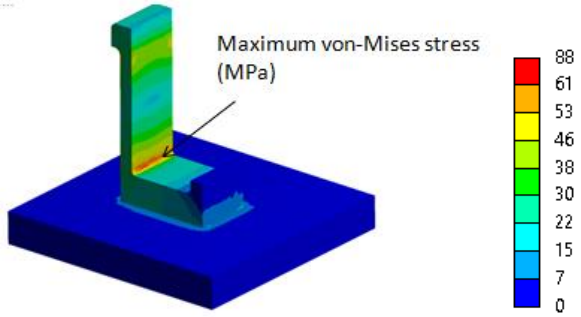

Figure 35: Maximum von-Mises distribution (MPa) in the horizontal force sensing structure

The maximum von-Mises stress ($88\ MPa$) is located at the neck of the horizontal beam and much lower than the yield strength of titanium alloy yielding a factor of safety of ~ 9. Therefore, the induced stresses in the horizontal force sensing structure are not expected to lead to structural failure under the analyzed loading conditions and design assumptions. Furthermore, the mean stress induced by the horizontal force sensing structure is $44\ MPa$, which is also much lower than the fatigue strength ($525\ MPa$) of titanium alloy. Therefore, the structure is expected to sustain at least 10^7 stress cycles.

3.3 Assembly of Tooth and Sensing Mechanism

This section presents the full assembly of the total sensing mechanism and molar tooth as shown in Figure 36. The molar tooth is placed in a $2.5\ mm$ base to emulate the clinical boundary condition in complete denture prosthesis. This is a reasonable assumption considering the fact that the thickness of denture base can be up to $3\ mm$.[106] This thickness depends on the available inter-arch space and other clinical factors such as implant positioning and

superstructure design. El-Anwar et al. reported that the average inter-arch space available for denture construction is 12 to 14 mm.[107]

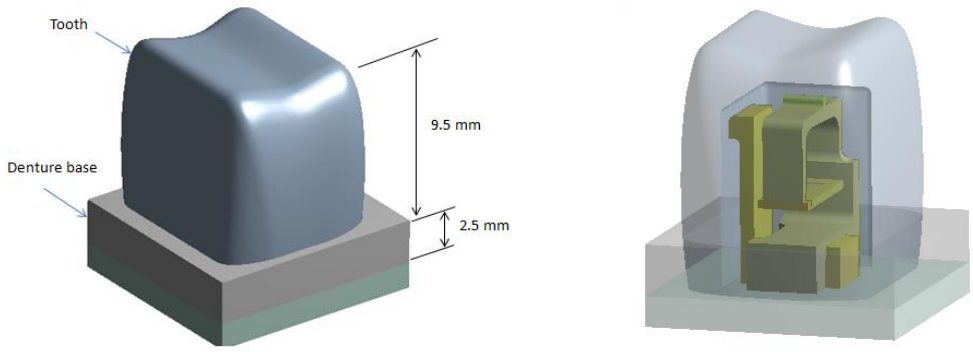

A B

Figure 36: Full assembly of the sensing mechanism, tooth and denture base. A, Isometric exterior view of the assembly. B, Transparent view showing vertical and horizontal force sensing structures inside the tooth

3.4 Evaluation of Strain

With the fully assembled model, the induced strains were evaluated in the vertical and horizontal force sensing beams under the maximum mastication load. It is important to know the maximum strain levels because the strain magnitudes govern the selection of the sensing element. Sensing elements such as strain gauges or force sensors have recommended operating range for long term application. For greater longevity, the strain level should be maintained within the specified range especially for dynamic load applications. As such, both vertical and horizontal loading conditions are analyzed and the resultant strain values are evaluated in the vertical and horizontal beams using FEA. The locations of the evaluated strains are discussed in Section 3.1.1 and 0. The

generated mesh with $Tet10$ and $Hex20$ elements is shown in Figure 37. The number of elements and nodes in the model were 185516 and 315038 respectively. The aspect ratio and Jacobians of at least 95% of the elements were maintained below 3, and 0.7 or greater respectively to put confidence on the results. At least two elements were maintained across the thickness of the structures.

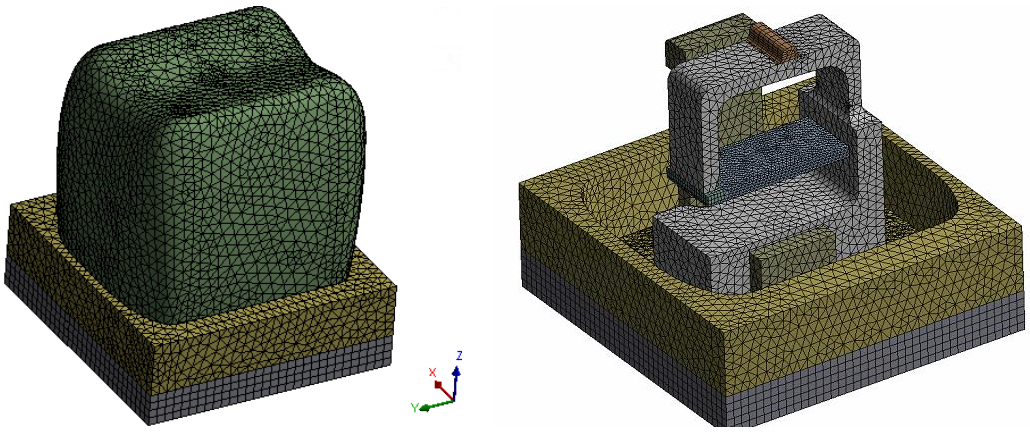

Figure 37: Generated mesh for the full assembly

The applied load and boundary conditions are similar to Figure 27 and Figure 33. $200\ N$ vertical and oblique ($30\ deg$) loads were applied at the central fossa and cusp (located $2\ mm$ offset from the central fossa) respectively. The loads were applied independently and at an area of $1\ mm^2$ on the occlusal surface. Fixed boundary conditions were imposed on the bottom surface and on the side walls of the denture base. This is to emulate the clinical condition where a tooth in a complete denture is bonded with the nearby teeth and no movement is allowed in the mesio-distal direction.

Bonded interface was assigned to all contact regions in the models except for the three regions as shown in Figure 38. Frictional boundary conditions were assigned between the sensing structure tip and cantilever beam (2nd) contact surfaces, between the horizontal beam tip and tooth side wall and between the lower occlusal surface and vertical force sensing structure contact interfaces. The coefficient of friction for the frictional contacts between the tooth wall (acrylic resin) and sensing structures (titanium alloy) was 0.32 and between the sensing structure tip and cantilever beam was 0.30.[100,102]

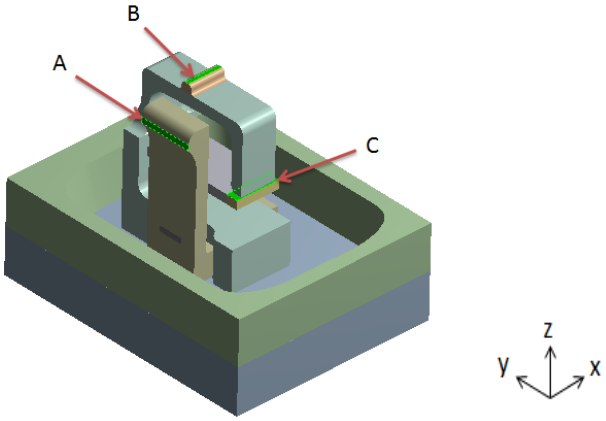

Figure 38: Contact regions with frictional boundary conditions (marked by A, B and C)

The resultant strain values are presented in Table 8. The maximum strain for the vertical loading is $1103\ \mu\varepsilon$. The maximum strains for the oblique loading are $646\ \mu\varepsilon$ and $513\ \mu\varepsilon$ in the vertical and horizontal force sensing beams respectively. The location of the induced strain in the vertical force sensing cantilever beam is at $0.5\ mm$ from the vertical column, and in the horizontal force sensing structure is at $0.5\ mm$ from the base.

The normal strain values of the full assembly model without denture base under the same loading conditions are $1125\ \mu\varepsilon$ in the vertical force sensing beam for the vertical loading, and $656\ \mu\varepsilon$ and $597\ \mu\varepsilon$ for the oblique loading in the vertical and horizontal force sensing beams respectively. Comparing these strain values with the full assembly model with denture base strain values as provided in Table 8, the induced strains at the vertical force sensing beam are not found to be significantly affected ($< 2\%$ decrease) by the denture base. However, the induced strain at the horizontal force sensing beam decreased to ~14% which is attributed to the fact that the fixed denture base resists the horizontal tooth movement during oblique load application.

Table 8: Resultant strain at the vertical and horizontal force sensing beams of the full assembly model

Loading condition	Normal strain ($\mu\varepsilon$)	
	Vertical force cantilever beam (y-dir)	Horizontal force cantilever beam (z-dir)
Vertical	1103	0
Oblique	646	513

3.5 Summary

In this chapter, the design of the two-axis sensing mechanism is presented. The sensing mechanism consists of a vertical force sensing structure and a horizontal force sensing structure. Various design features associated with the two structures are discussed to obtain a maximum measurable strain and

stress analyses are performed (using FEA) to ensure structural integrity under static and dynamic loadings. The full assembly of the sensing mechanism is incorporated inside the molar tooth and strain values are obtained under vertical and oblique loading conditions ($200\ N$). The maximum induced strain in the vertical force sensing beam is $1103\ \mu\varepsilon$ and in the horizontal force sensing beam is $513\ \mu\varepsilon$. Thus, it is demonstrated that the vertical and horizontal force sensing structures satisfies the design objectives considering all the design constraints or geometric feature size, material properties and loading conditions.

4 Prototyping and Verification

This chapter presents prototyping and verification of the proposed sensing mechanism through experimental analysis. At first, specifications of the sensing element and procedure for strain measurement are discussed. Next, the method of component fabrication and experimental setup are described. The tooth and the sensing structures were fabricated out of a polymeric material (somos-watershed 11120) instead of acrylic resin and titanium respectively. Lastly, sensor response characterization, validation of mechanical amplification and sensor calibration process to evaluate the total force from the vertical and horizontal force sensor readings are discussed.

4.1 Sensing Element and Electronics

In this section, the characteristic features of the strain gauge sensing element (Subsection 4.1.1), signal conditioning circuitry (Subsection 4.1.2) and the LabVIEW interface for data acquisition (Subsection 4.1.2) are presented.

A strain gauge was selected as the sensing element for the proposed sensing mechanism. Strain gauge sensors are available in small sizes and are well established in terms of design and fabrication techniques. In general, the measured strain is small and often expressed as microstrain ($\mu\varepsilon$).

Figure 39 presents the flow diagram of the data acquisition process for strain measurement. Since the change of resistance is very small, a signal conditioning unit is required. The signal conditioning circuit is typically comprised of a Wheatstone bridge and an amplification circuits. The output signal is then

acquired using a data acquisition (DAQ) module and processed within the LabVIEW environment. Next, the acquired signal is filtered using a digital filter in LabVIEW followed by graphical display/data logging.

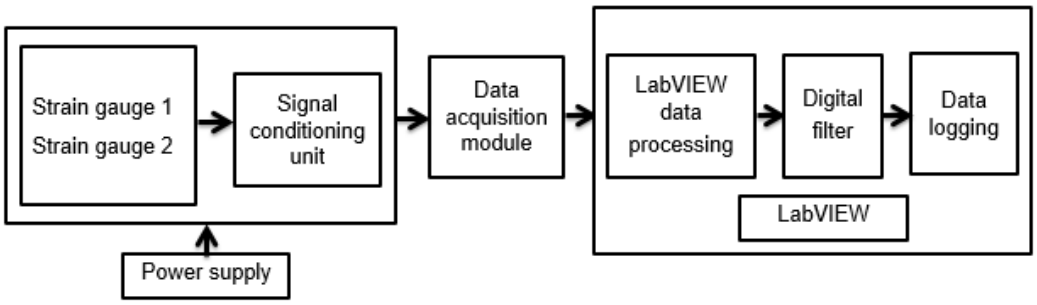

Figure 39: Flow diagram of the data acquisition process for strain measurement procedure

4.1.1 Strain Gauge for the Proposed Design

The strain gauge used in the present study was a metal foil strain gauge ($FLA-03$) from Tokyo Sokki Kenkyujo Co., Ltd. This is a single element $120\ \Omega$ strain gauge with $0.3\ mm$ gauge length, $1.4\ mm$ gauge width and 2.33 gauge factor. The gauge base length and width are $3\ mm$ and $2\ mm$ respectively. The grid material is Cu-Ni alloy and the backing is made of epoxy resin. The nomenclature for describing the strain gauge characteristic features are shown in Figure 40.[108]

The $FLA-03$ strain gauge was selected due to its small size and dynamic strain limit. According to the manufacturer, this gauge can sustain more than 10^6 strain cycles provided that the exerted strain is below $1500\ \mu\varepsilon$.[108] From the analyses performed under the vertical and oblique loading conditions

(Section 3.4), the induced maximum strains at the location of the active gauge area in the vertical and horizontal force cantilever beams are $1103\ \mu\varepsilon$ and $513\ \mu\varepsilon$ respectively which are well below $1500\ \mu\varepsilon$.

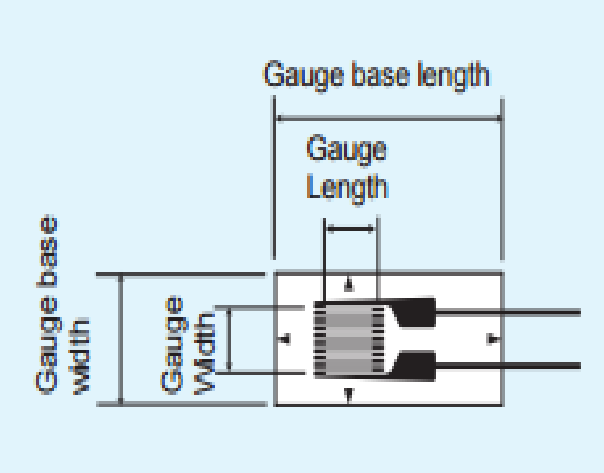

Figure 40: Characteristic features of a strain gauge

4.1.2 Signal Conditioning Unit

In general, the measurable strain in physical systems is small provided that the induced strain on which the gauge is mounted is within the elastic limit of the material. Consequently, the resultant change of strain gauge resistance is also small. In order to measure such small changes accurately, a Wheatstone bridge circuit is commonly used. In the present study, a Wheatstone bridge circuit with a quarter bridge configuration was used for which the output voltage (V_{out}) is related with the strain according to Equation 5.

$$\mathrm{V_{out}} = -\frac{GF\ \varepsilon}{4}\left(\frac{1}{1+GF\ \frac{\varepsilon}{2}}\right)\mathrm{V_{ex}} = -\frac{GF\ \varepsilon}{4}N\ V_{ex} \qquad \text{Equation 5}$$

In Equation 5, ε is the strain, GF is the gauge factor, and V_{ex} is the excitation voltage. Note that the term, N indicates non-linearity in the output voltage. However, for small strain of $1100\ \mu\varepsilon$ and GF of 2.33, as in the case of the present study, the magnitude of N is 0.99 and is therefore set equal to 1.

An instrumentation op-amp ($AD623$) was used to amplify the output voltage signal. This is a single supply instrumentation amplifier with $+3\ V$ to $+12\ V$ operating voltage range. The $AD623$ gain is adjusted using a single resistor and can be configured to be up to 1000. The maximum attainable gain depends (primarily) on the excitation voltage and input mastication frequency. In the present study, the amplifier gain was set to be 200 based on the excitation voltage. The gain has to be selected such that the amplified voltage output does not exceed the excitation voltage level.

For data acquisition, an $NI\ USB-6002$ DAQ was used. This is a 16-bit (A/D converter) device with $\pm 10\ V$ input range. For the $3.3\ V$ excitation voltage used in the present study, the resolution (smallest possible detectable voltage) of the DAQ is $3.3 \div (2^{16}-1) = \ 0.04\ mV$. With this voltage, the smallest measurable strain is $20.80\ \mu\varepsilon$ according to Equation 5. Due to 200 times amplification, the smallest measurable strain is further reduced to $0.104\ \mu\varepsilon$.

4.1.3 LabVIEW Interface

LabVIEW (version 14.0) was used for the graphical display and data recording. The flow diagram of the LabVIEW data processing interface is shown in Figure 41.

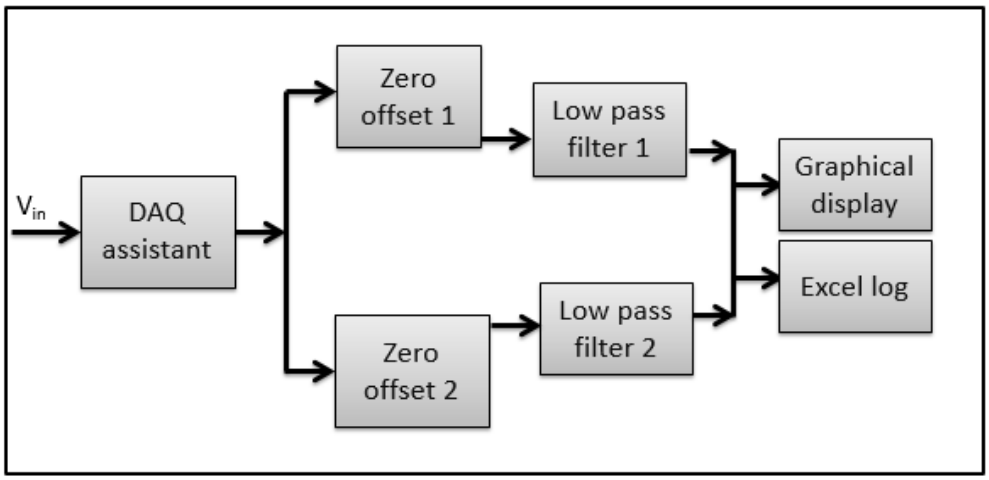

Figure 41: Flow diagram of the LabVIEW interface

First, the generated voltage outputs (amplified) from the signal conditioning circuits are input to the analog input channels of the DAQ device. The DAQ inputs are then wired to zero offset functions in LabVIEW software to remove bias voltages and balance the bridge outputs. These outputs are then passed through low pass filters to remove noise. A 1st order low pass digital filter with a cut-off frequency of $5\ Hz$ was used. The cut-off frequency was defined based on experimental observation and may be changed. The filtered signals are then graphically displayed in waveform graphs and saved in Microsoft Excel file format for post processing.

4.2 Experimental Setup

For the experimental validation of the proposed design, the vertical and horizontal force sensing structures and the molar tooth were fabricated using additive manufacturing technology. Due to the unavailability of resources to fabricate titanium sensing structures and acrylic resin molar tooth, all the

components were manufactured using somos-watershed 11120 material. In this section, prototyping of the proposed sensing mechanism (Subsection 4.2.1), method of fabrication (Subsection 4.2.2), assembly of the fabricated vertical and horizontal force sensing structures with molar tooth (Subsection 4.2.3), description of the experimental testbed (Subsection 4.2.4), and load cell calibration for the sensor response characterization (Subsection 4.2.5) are discussed.

4.2.1 Design Modifications

The Young's modulus of somos material is ~ 36 times lower than that of titanium[103]. Consequently, the vertical force sensing structure had to be modified as shown in Figure 42. There were two modifications from the proposed design with titanium sensing mechanism; change of vertical cantilever beam thickness and reduction of vertical force sensing structure neck height as shown with a circled area in Figure 42. The thickness of the cantilever beam was increased to $0.5\ mm$ and the neck height was reduced to $1.7\ mm$ to facilitate better fabrication quality and structural integrity. There was no modification of the proposed horizontal force sensing structure design. For the molar tooth, the Young's modulus of the somos material ($2.7\ GPa$) is close to the acrylic resin material ($2.8\ GPa$) and is expected to closely resemble clinical denture tooth property. For the mastication load, a $50\ N$ load was applied instead of $200\ N$. The reason for changing the mastication load was that the robot used for the load application did not have the capacity to apply $200\ N$ (discussed in Section 4.2.4). The occlusal surface thickness was reduced from $2.90\ mm\ to\ 1.40\ mm$ so that the resultant

deformation at the lower occlusal surface is $\sim 40\ \mu m$. Thus, the adopted modifications, for the purpose of testing and proof of concept, do not alter the original design intended performance and the proposed approach can still be experimentally validated.

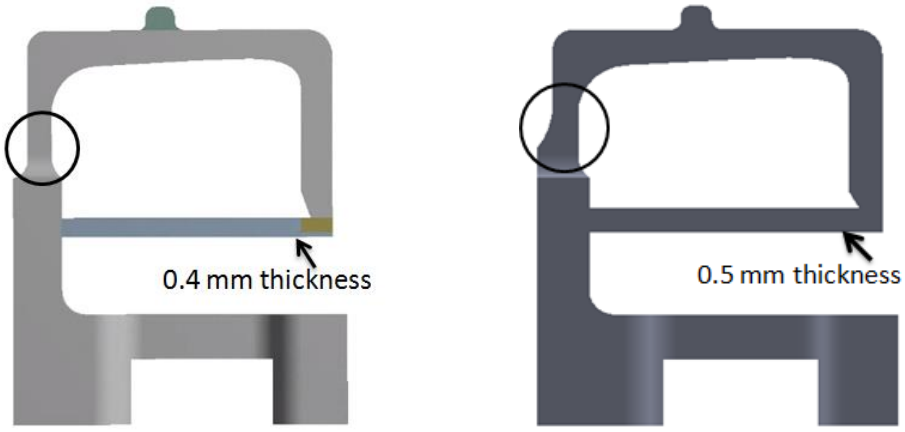

A B

Figure 42: Design modifications for prototyping and verification purposes. A, Proposed vertical force sensing structure with titanium. B, Fabricated vertical force sensing structure with somos material (modified neck height and cantilever beam thickness)

4.2.2 Fabrication

The fabricated vertical and horizontal force sensing structures with somos material are shown in Figure 43. These parts were fabricated using SLA printer (Viper si2 SLA System 3D Printer) at the University of Texas Arlington Research Institute (UTARI).

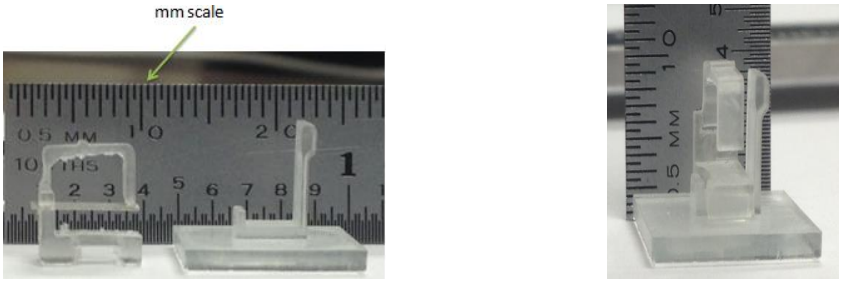

A B

Figure 43: Fabricated sensing structures with a mm scale in the background. A, Individual components. B, Sensing mechanism assembly

4.2.3 Assembly of Tooth and Sensing Mechanism

The strain gauges were mounted on the vertical and horizontal force sensing beams using Loctite instant adhesive. For the surface preparation, the mounting beams were cleaned with alcohol and slightly etched with fine sand paper.

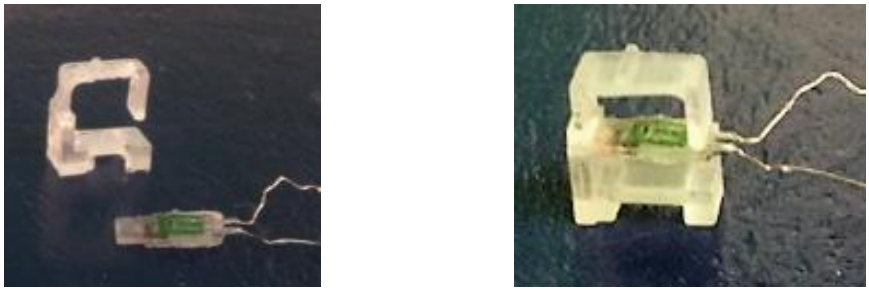

A B

Figure 44: Assembly of the vertical force sensing structure. A, Strain gauge installed on the vertical cantilever beam. B, Vertical force sensing structure assembly

The mounted strain gauge on the vertical cantilever beam is shown in Figure 44-A. Once firm bonding is established, the beam was inserted into the

sensing structure and glued as shown in Figure 44-B. The strain gauge lead wires were guided around the sensing structure base to facilitate assembly. Similarly, another strain gauge was attached to the horizontal force sensing structure as shown in Figure 45. The lead wires, in this case, were wrapped around the tip of the structure to enable proper wire harnessing.

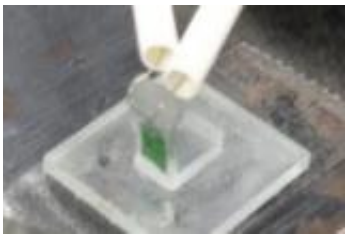

Figure 45: Strain gauge mounted on the horizontal force sensing structure

Next, the vertical and horizontal force sensing structures were integrated and the assembled sensing mechanism with strain gauges is shown in Figure 46.

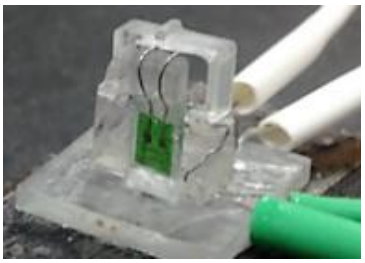

Figure 46: Assembly of vertical and horizontal force sensing structures

Lastly, the assembled vertical and horizontal force sensing structures were inserted in the molar tooth. In order to ensure that the tooth is rigidly positioned and contacts are maintained at the desired locations of the sensing structures, a base and a guide were designed and fabricated using additive manufacturing. The thickness of guide was selected to represent the denture base height in the complete denture prosthesis construction.

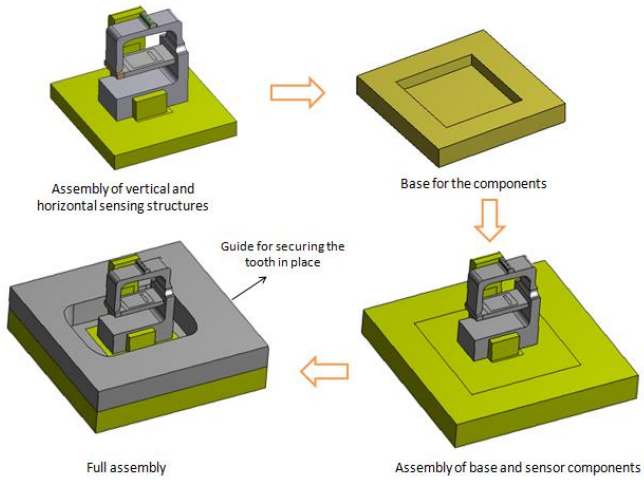

Figure 47: Assembly flow diagram of the full assembly

Figure 47 shows the flow diagram of the full assembly. First, the assembly of the vertical and horizontal force sensing structures was glued to the base. Next, the guide was placed above the base and manually adjusted to establish the desired contacts. The final assembly of the vertical and horizontal force sensing structures, tooth sensor base and guide is shown in Figure 48.

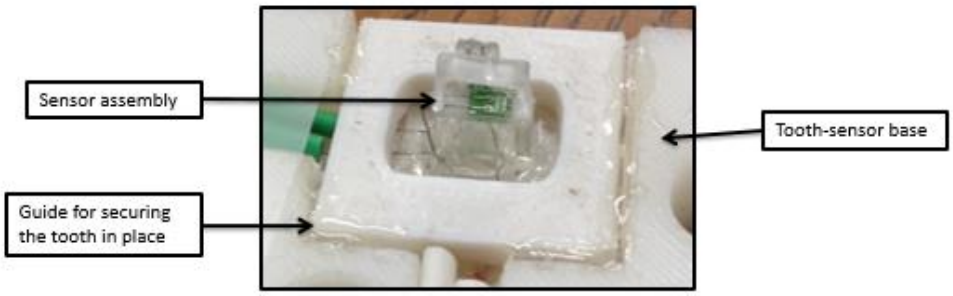

Figure 48: Assembly of the sensing mechanism, tooth-sensor base and guide

4.2.4 Experimental Testbed

The experiments were performed using a SCARA robot (Adept Cobra i600) as the load application device. First, the final assembly of the sensing

mechanism was secured in the robot workspace as shown in Figure 49. Next, the molar tooth was placed in the created final assembly and bonded permanently with the guide to restrict undue movements during load applications.

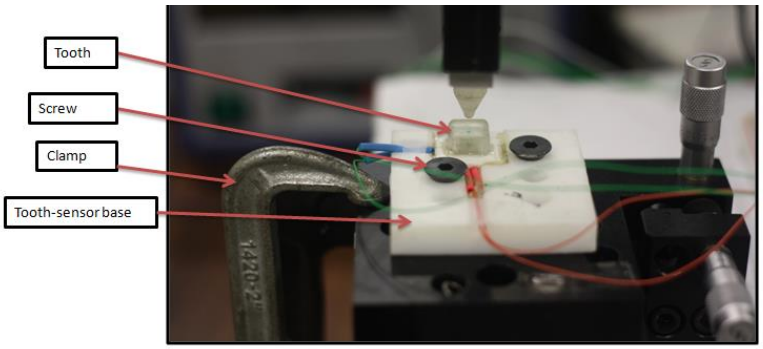

Figure 49: Experimental testbed with tooth and sensing mechanism assembly

The Adept Cobra i600 is a four-axis SCARA robot with three rotational (joint #1, joint #2, joint #3) and one translational (joint #4) joints as shown in Figure 50. This robot was selected due to its good repeatability which is essential for controlled load applications. The repeatability of the fourth joint is $\pm 3\ \mu m$.

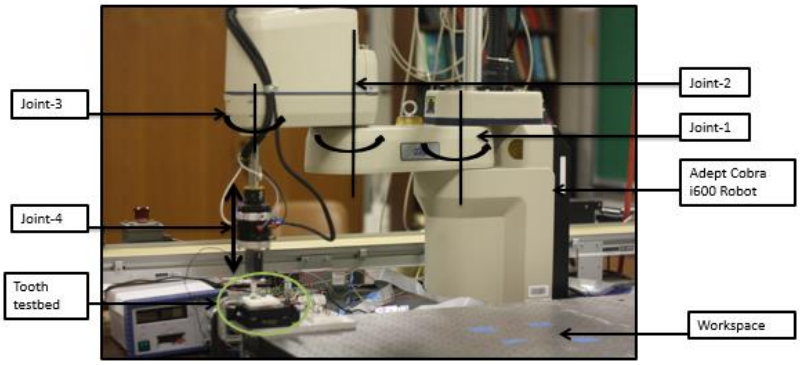

Figure 50: Adept Cobra i600 robot for experimental analysis

To measure the applied force, a load cell was attached at the end of the manipulator's head as shown in Figure 51. The load cell is an MTS force

transducer (part # $4501018/B$) with rated maximum capacity of $250\ N$ ($56.2\ lbf$). One end of the load cell was connected to the robot manipulator head and the other end was augmented with a spherical tip of $\sim 1\ mm$ diameter as shown in Figure 51. Since the load cell was used to characterize and calibrate the vertical and horizontal force sensors, it was initially calibrated.

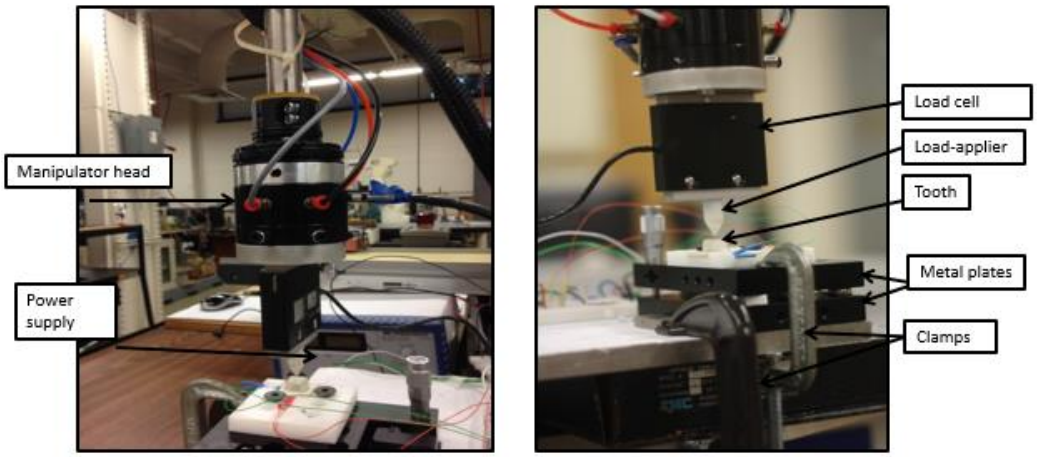

Figure 51: Close view of the robot manipulator head, load cell, and experimental testbed

4.2.5 Load Cell Calibration

Calibration of the load cell was performed before attaching to the robot. The calibration was performed with dead weights for a total of $50\ N$ load applied at $10\ N$ increments. The excitation voltage for the load cell was $3.3\ V$. The resultant plot for the load versus voltage output is shown in Figure 52. The load, F and load cell voltage output, v are linearly correlated ($F = 6.38v$) with a regression coefficient of 0.99 as shown in Figure 52.

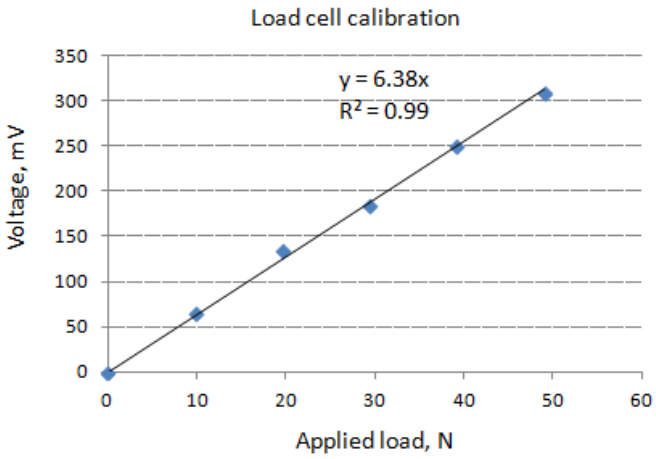

Figure 52: Load cell calibration plot

4.3 Sensor Response Characterization

Sensor characterization is important in understanding the behavior of the sensor response as a function of the input. Typical questions relating to sensor behavior include - What is the settling time? How does the sensor behave with time? Is the response linear or non-linear? To seek answers to these questions, responses from the two sensors were investigated separately and mathematical models were developed for theoretical predictions.

4.3.1 Vertical Force Sensor

A representative typical sensor output from the vertical force sensor due to a step input load of $25\ N$ held for $60\ s$ is shown in Figure 53. The sensor output voltage decreases exponentially with time and reaches a steady state value. Similar behavior is observed for the unloading phase as well where the response gradually returns to the base voltage. Furthermore, the responses for the loading and unloading phases are different. To account for these different behaviors, the

loading and unloading phases were analyzed separately and later combined to obtain the total response.

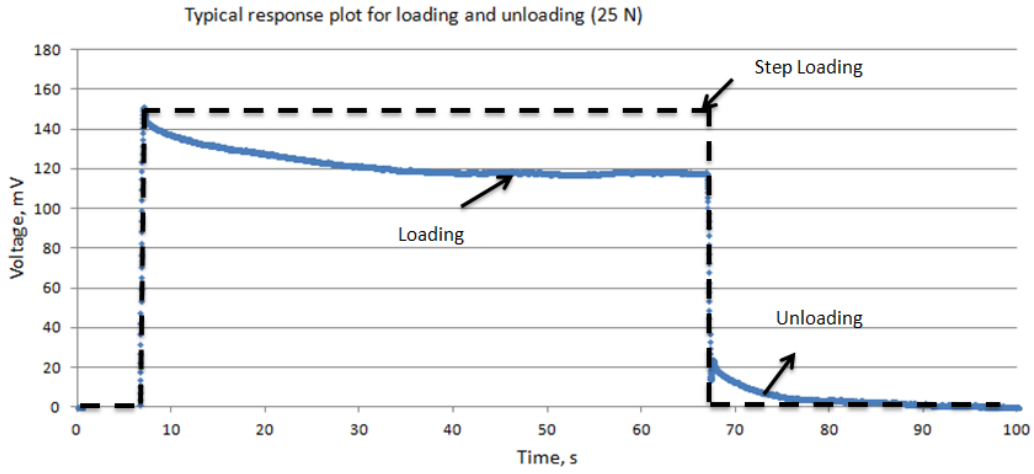

Figure 53: Typical vertical force sensor response for loading and unloading

The exponential decay in the sensor response may be represented by a second order system (overdamped) or as a combination of two first order systems due to the fact that they exhibit similar response behavior. The loading response is first characterized with a second order overdamped system in an attempt to determine if the inertia effect is significant enough to influence the system behavior.

The solution for an overdamped system in the time domain is given by Equation 6.[109]

$$x(t) = \frac{x_0}{\lambda_1 - \lambda_2}(\lambda_1 e^{\lambda_2 t} - \lambda_2 e^{\lambda_1 t}) \qquad \text{Equation 6}$$

In Equation 6, x_0 is the initial value, and $\lambda_1$and λ_2 are the eigenvalues of the system given by Equation 7.

$$\lambda_{1,2} = -\zeta\omega_n \pm \omega_n\sqrt{\zeta^2 - 1} \qquad \text{Equation 7}$$

In Equation 7, ω_n is the natural frequency (undamped), and ζ is the damping ratio. The undamped natural frequency of the cantilever beam is obtained based on Euler-Bernouli beam theory which is valid for beams with length-to-height ratio of 10 or more and neglects the shear deformation effects.[110] The length-to-height ratio of the cantilever beam in the present study is ~ 11. Thus, for free vibration the equation of the first natural frequency, $\omega_1(rad/s)$, of a cantilever beam with fixed-free boundary condition is given by Equation 8.[101,110]

$$\omega_1 = 1.875^2\sqrt{\frac{EI}{mL^4}}\,(rad/s) \qquad \text{Equation 8}$$

In Equation 8, E is the Young's modulus of the beam material ($2.7\ GPa$), I is the area moment of inertia of the beam ($I = 0.026\ mm^4$ with $b = 2.5\ mm$, $h = 0.5\ mm$), m is the mass of the beam ($7.98\ mg$), and L is the length of the beam ($5.7\ mm$). Using Equation 8, the undamped natural frequency of the cantilever beam is calculated as $24249\ rad/s$ ($3859\ Hz$).

Next, employing Equation 6, a curve fit of the loading response was established using least squares approximation method. The goodness of the curve fit is determined using root mean squared (RMS) error for n samples according to Equation 9.

$$RMS = \sqrt{\frac{\sum_1^n (Experimental\ output - theoretical\ output)^2}{n}} \qquad \text{Equation 9}$$

The experimental response and theoretical curve fit for the vertical force sensor response during loading are shown in Figure 54. The total RMS error ($n =$

6000) for the curve fit is $0.95\ mV$. The voltage output of the vertical force sensor for the maximum load ($50\ N$) is $275\ mV$. As such, the estimated RMS error is only 0.3% of the maximum voltage output which indicates a good agreement between the experimental and theoretical responses. For the obtained curve fit, the damping ratio (ζ) is 125800, and the eigenvalues are $\lambda_1 = -0.09$ and $\lambda_2 = -6.1\times10^9$.

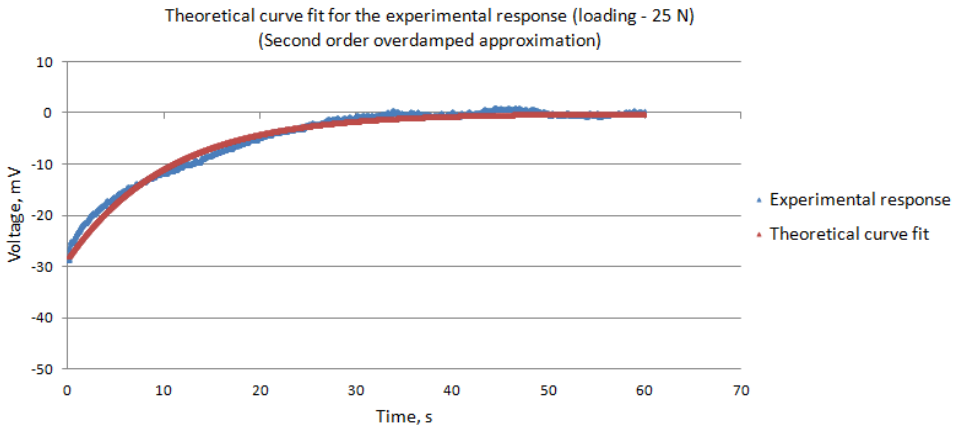

Figure 54: Theoretical curve fit for the vertical force sensor response during loading ($25\ N$) with a second order overdamped system

Note that the damping ratio is very large and the magnitude of λ_2 is much greater than that of λ_1. The large damping ratio value is indicative of a highly overdamped system. In general, systems with two real roots can be represented as a combination of two first order systems and the time constants are calculated as the reciprocals of the eigenvalues (real parts). Generally, if the absolute magnitude of the larger pole is 10 times higher than that of the smaller one, then the influence of the former on the system behavior is considered negligible and the total system may be approximated as a single first order system.[111]

Therefore, for the present study, the system behavior is predominantly affected by λ_1 and the effect of λ_2 is negligible. As such, the two sensor responses are characterized as equivalent first order systems and time constants are evaluated accordingly.

The time response of a first order system with a step input is presented in Equation 10.

$$y(t) = \frac{c}{a} + \left(b - \frac{c}{a}\right) e^{-at} \qquad \text{Equation 10}$$

In Equation 10, c/a represents the equilibrium value and b is the initial value for output, $y(t)$. The transfer function for this system is given by Equation 11. The transfer function is used to evaluate the theoretical responses of the sensor output.

$$H(s) = \frac{bs + c}{s + a} \qquad \text{Equation 11}$$

In the subsequent analyses, Equation 10 is used for theoretical curve fitting. Since the loading and unloading responses were different, they were curve fit separately and later combined. Figure 55 shows the curve fit for the vertical force sensor loading response and the theoretical equation is shown in Equation 12, where $V_{VFSL}(t)$ is the voltage output for vertical force sensor during loading.

$$V_{VFSL}(t) = \frac{12.25}{0.10} + \left(150.84 - \frac{12.25}{0.10}\right) e^{-0.10t} \qquad \text{Equation 12}$$

The time constant for the loading cycle is $10\ s$ and the RMS error ($n = 6000$) is $1.41\ mV$. This error is 0.5% of the maximum vertical force sensor output

voltage ($275\ mV$) which is indicative of a good fit between the experimental and theoretical responses. Since the settling time is approximately five times the time constant, in this case it is $\sim 50\ s$. Thus, it takes $\sim 50\ s$ for the vertical force sensor to reach steady state (99%).

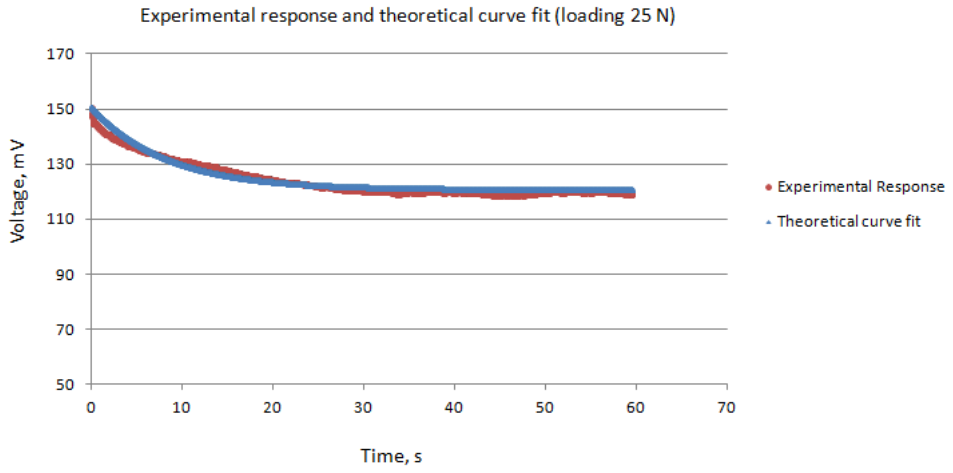

Figure 55: Experimental and theoretical responses of the vertical force sensor during loading ($25\ N$)

The exponential decay behavior may be attributed to the sensor beam material. The sensor is installed on a polymeric beam and polymer is known to exhibit viscoelastic behavior. Two main characteristics of viscoelastic materials are creep and stress relaxation. Creep is characterized as the increase of strain upon application of constant stress. Stress relaxation is described by the gradual decay of stress under constant strain or displacement. The response of the sensor is representative of a typical stress relaxation behavior wherein under constant displacement, the output voltage decreases exponentially until an equilibrium value is reached.

Stress relaxation in the polymer is usually described in terms of the relaxation time and relaxation modulus. The relaxation time, τ, is a measure of the time-dependent gradual decay of the stress under a constant displacement. Stress relaxation modulus, on the other hand, is given by, $E(t) = \sigma(t)/\varepsilon_0$, where $\sigma(t)$ is the induced stress as a function of time and ε_0 is the initial strain. The stress relaxation of materials such as polymers can be represented by the SE (Stretched Exponential) model given by Equation 13.[112]

$$E(t) = E_\infty + (E_0 - E_\infty)e^{-\frac{t}{\tau}} \qquad \text{Equation 13}$$

In Equation 13, E_0 is the initial modulus, E_∞ is the equilibrium modulus (relaxation modulus) at infinite time and τ is the relaxation time. This equation is similar to Equation 10 with the constants a, b and c depended on material properties.

Next, the curve fitting is performed for the unloading phase. Similar to the procedure for the loading response, a theoretical curve fit is obtained and the time constant is determined. Figure 56 shows the experimental response and theoretical curve fit for the vertical force sensor response during unloading. The theoretical equation for the curve fit is presented in Equation 14, where $V_{VFSU}(t)$ is the voltage output due to vertical force sensor during unloading.

$$V_{VFSU}(t) = 24.53e^{-0.15t} \qquad \text{Equation 14}$$

The time constant for the unloading phase is $6.6\ s$ which is equivalent to a settling time of $\sim 33\ s$. The RMS error ($n = 4500$) is $1.55\ mV$. This error is 0.5% of

the vertical force sensor voltage output ($275\ mV$) for the maximum applied load ($50\ N$).

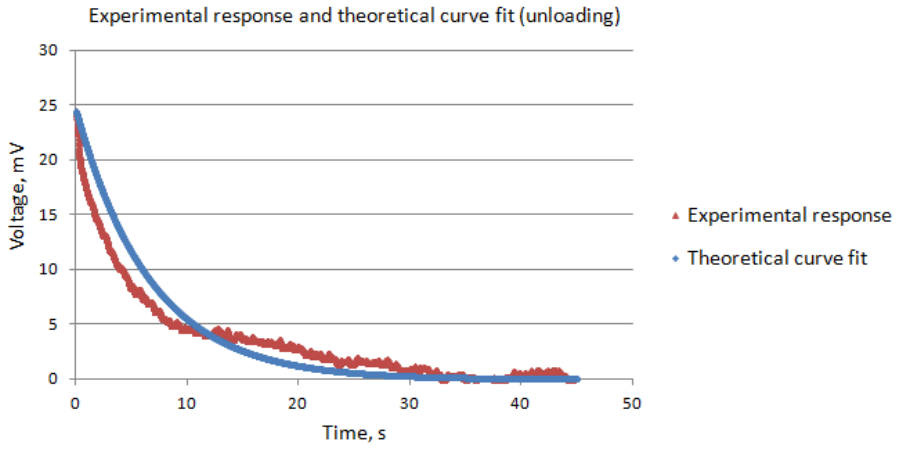

Figure 56: Experimental and theoretical responses of the vertical force sensor during unloading

Following the same procedure, the loading and unloading responses were analyzed for various input loads of up to $50\ N$ and similar time constants were obtained (between $10\ s$ to $8.3\ s$ for loading and $7\ s$ to $6.6\ s$ for unloading). Thus, the sensor exhibited a repeatable behavior under the applied loading scenarios.

The transfer functions for loading and unloading are evaluated (using Equation 11), and combined to model the complete vertical force sensor behavior. The transfer functions for the loading and unloading of the vertical force sensor are presented in Equation 15 and Equation 16 respectively.

$$V_{VFSL}(s) = \frac{150.84\ s + 12.25}{s + 0.10} \qquad \text{Equation 15}$$

$$V_{VFSU}(s) = \frac{24.53\ s}{s + 0.15}$$ Equation 16

To validate the developed theoretical model for the vertical force sensor response characterization, experimental and theoretical responses for a different load ($15\ N$) are evaluated. Figure 57 shows the experimental and theoretical responses for the $15\ N$ step load held for $60\ s$. The theoretical response is generated with the same time constants as the $25\ N$ loading ($10\ s$) and unloading ($6.6\ s$). The graph shows a good agreement between the two responses and demonstrates that the theoretical model can predict the vertical force sensor response behavior reliably.

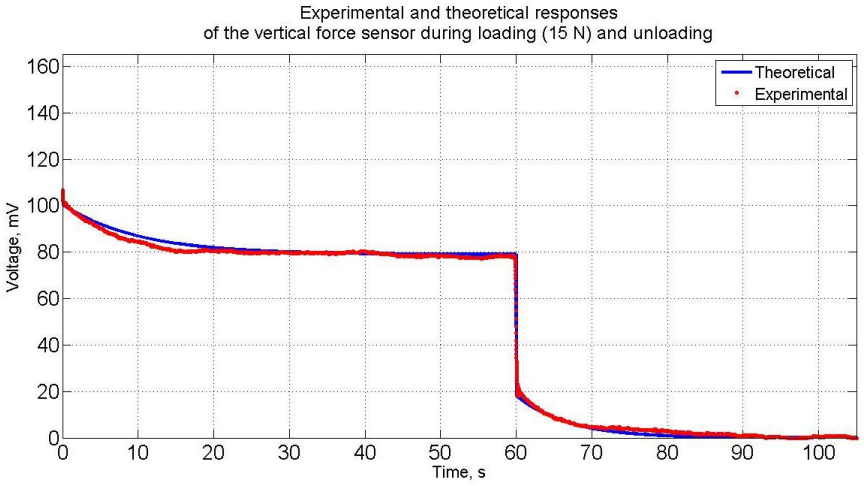

Figure 57: Experimental and theoretical responses of the vertical force sensor for a $15\ N$ step load

Mastication is a dynamic process with a typical frequency of ~1 Hz.[113] Since the vertical force sensor requires time to reach its steady state value during loading and unloading, it is important to investigate the sensor behavior

under different load durations. A step load of $25\ N$ was applied for $0.5\ s$, $1\ s$, $3\ s$ and $6\ s$ durations. The responses were allowed to reach their steady states between the successive loading. The sensor responses are shown Figure 58. Different behaviors are observed for different load durations. When the load is applied for a short duration, the beam recovers almost instantly. With the increase of load duration, the sensor requires a longer time to reach the base/reference voltage. As such, a time dependent response is observed which could be attributed to the fact that holding the load for longer duration allows the stress relaxation process to occur. For the short duration, however, there is not enough time for the stress relaxation process to even initiate. This behavior is desirable for the purpose of measuring the mastication load, since the sensor response needs to be fast enough to be able to accurately measure the load under $1\ Hz$ frequency.

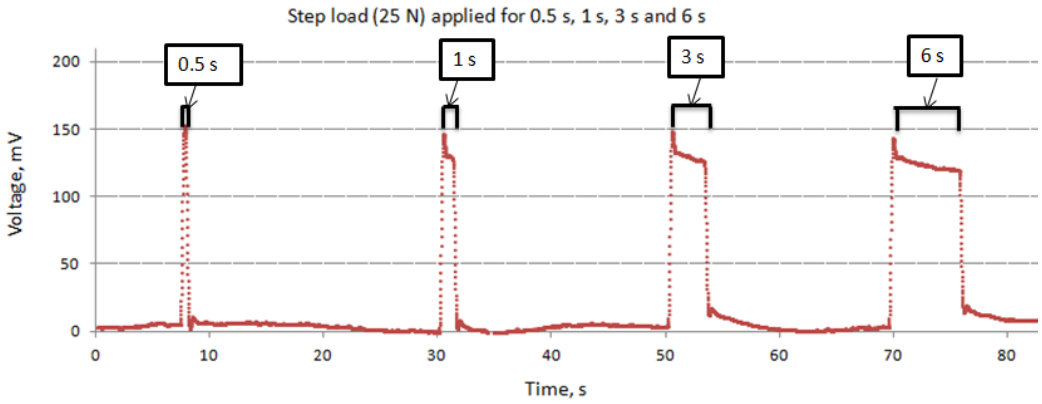

Figure 58: Step load of $25\ N$ applied for $0.5\ s$, $1\ s$, $3\ s$ and $6\ s$ durations

Repeatability is defined as the ability of a sensor to produce the same output under same input conditions. In the present study, the repeatability of the

vertical force sensor was evaluated by applying a step load $(20\ N)$ 10 times at $\sim 1\ Hz$ frequency. Figure 59 shows the response of the sensor due to the repeated load. The peak voltage at each cycle is measured and analyzed. The average of the 10 readings is $77.83\ mV$, and the standard deviation is $0.13\ mV$ which is 0.04% of the maximum vertical force sensor voltage output ($275\ mV$). The analysis was also repeated for various input loads with the same frequency of $1\ Hz$ and similar standard deviations $(< 0.25\ mV)$ were observed. Thus, the vertical force sensor exhibited good repeatability under dynamic loading.

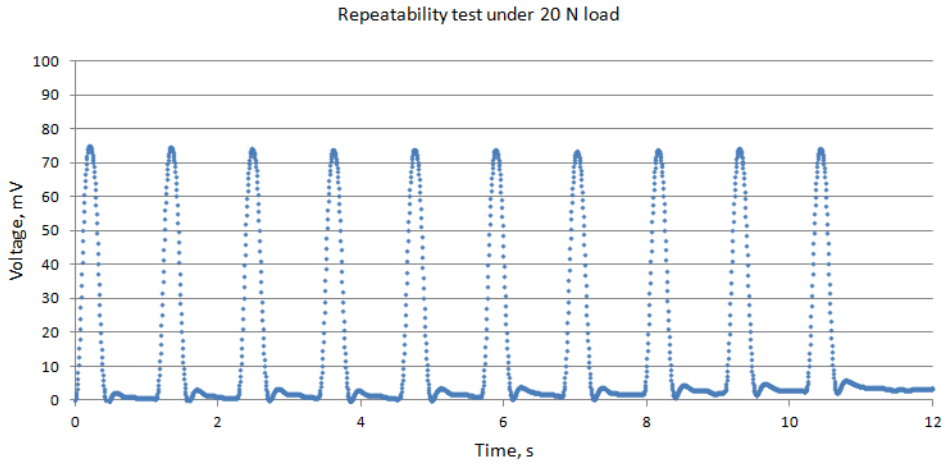

Figure 59: Repeatability test with $20\ N$ load applied 10 times at $\sim 1\ Hz$ frequency

4.3.2 Horizontal Force Sensor

The transfer functions for the horizontal force sensor are obtained following the same procedures as the vertical force sensor. Figure 60 shows the plot of the experimental response and theoretical curve fit for the horizontal force sensor loading phase under a $30\ N$ applied load. The time constant for loading is

$\sim 9\ s$. Therefore, it requires $\sim 45\ s$ for the horizontal force sensor to reach its steady state value during loading. The RMS error ($n = 6000$) for the curve fit is $0.54\ mV$ which is 1.35% of the horizontal force sensor voltage output ($40\ mV$) under the maximum applied load ($50\ N$) in the present study, and therefore indicates a good fit between the experimental and theoretical responses.

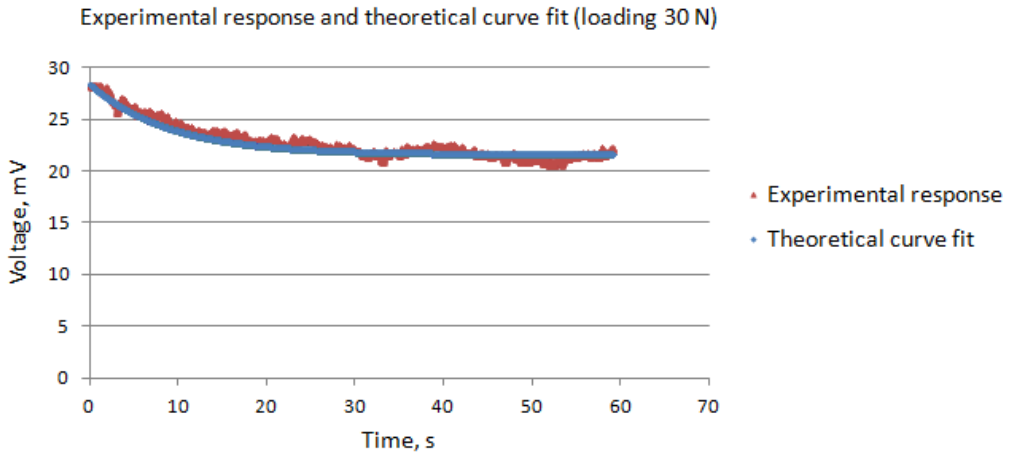

Figure 60: Experimental response and theoretical curve fit of the horizontal force sensor response during loading ($30\ N$)

Next, the time constant for the unloading phase is evaluated. The experimental response and theoretical curve fit are shown in Figure 61. The time constant is $1.25\ s$ meaning it requires approximately $6.25\ s$ for the horizontal force sensor to reach the base voltage during unloading. The RMS error ($n = 1800$) is $0.72\ mV$ which is 1.8% of the maximum horizontal force sensor voltage output ($40\ mV$) and indicates a good fit between the experimental response and theoretical curve fit.

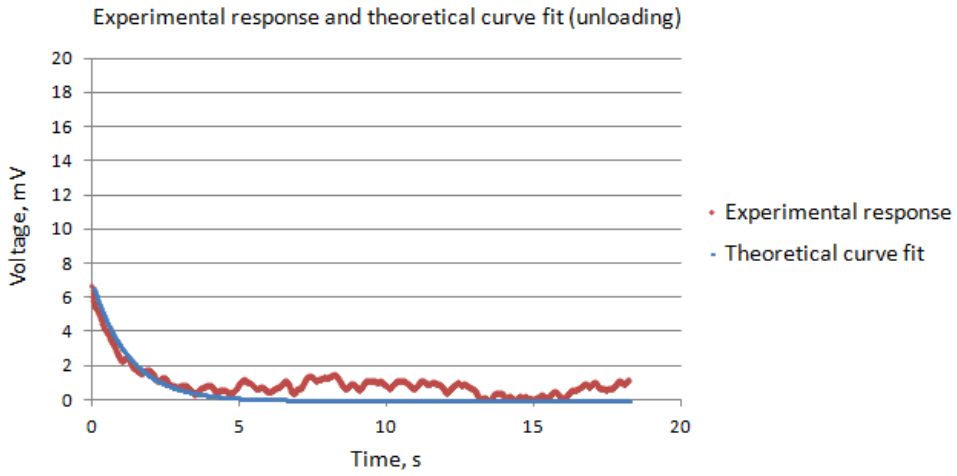

Figure 61: Experimental response and theoretical curve fit of the horizontal force sensor response during unloading

Next, the transfer functions for loading and unloading are combined and the total theoretical response is generated. The transfer functions for the loading, $V_{HFSL}(s)$, and unloading, $V_{HFSU}(s)$, of the horizontal force sensor are presented in Equation 17 and Equation 18 respectively.

$$V_{HFSL}(s) = \frac{28.38\,s + 2.38}{s + 0.11} \qquad \text{Equation 17}$$

$$V_{HFSU}(s) = \frac{6.67\,s}{s + 0.8} \qquad \text{Equation 18}$$

To validate the developed theoretical model, a different load ($20\ N$) is applied and the experimental and theoretical responses are plotted in the same graph as shown in Figure 62. For the theoretical response, same time constants obtained from the $30\ N$ loading ($9\ s$) and unloading ($1.25\ s$) are used. The graph shows a good agreement between the experimental and theoretical responses

and validates that the developed theoretical model can reliably predict the horizontal force sensor response behavior.

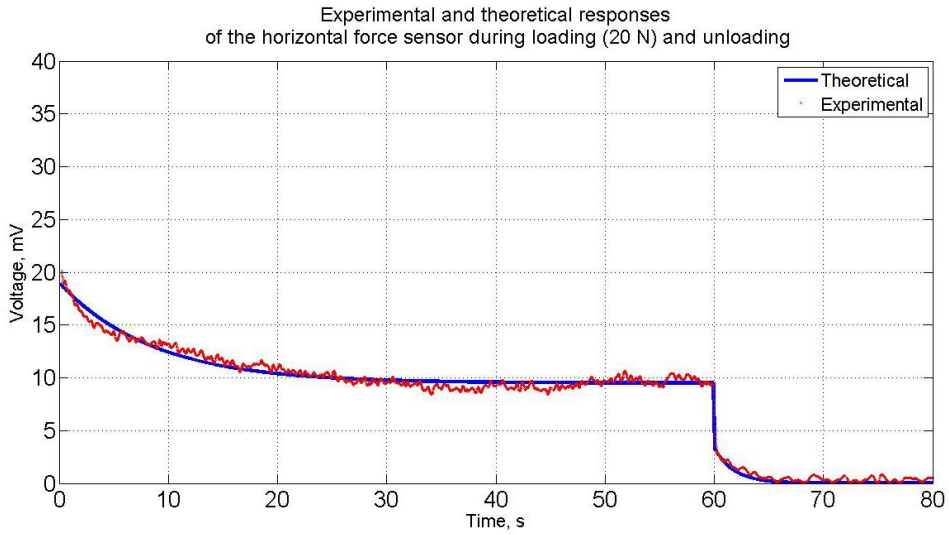

Figure 62: Experimental and theoretical responses of the horizontal force sensor for a $20\ N$ step load

Similar to the vertical force sensor, the horizontal force sensor also demonstrated quick recovery under dynamic loading. Since the time constant for the unloading phase is small, the sensor is able to recover quickly. To determine the repeatability of the horizontal force sensor, a step load of $25\ N$ load was applied 10 times at a frequency of $\sim 1\ Hz$. Figure 63 shows the plot of the repeatability test. The average of the 10 peak voltages is $23.98\ mV$, and the standard deviation is $0.67\ mV$. This is 1.67% of the maximum horizontal force sensor voltage output ($40\ mV$) and indicates good repeatability of the horizontal force sensor response under dynamic loading.

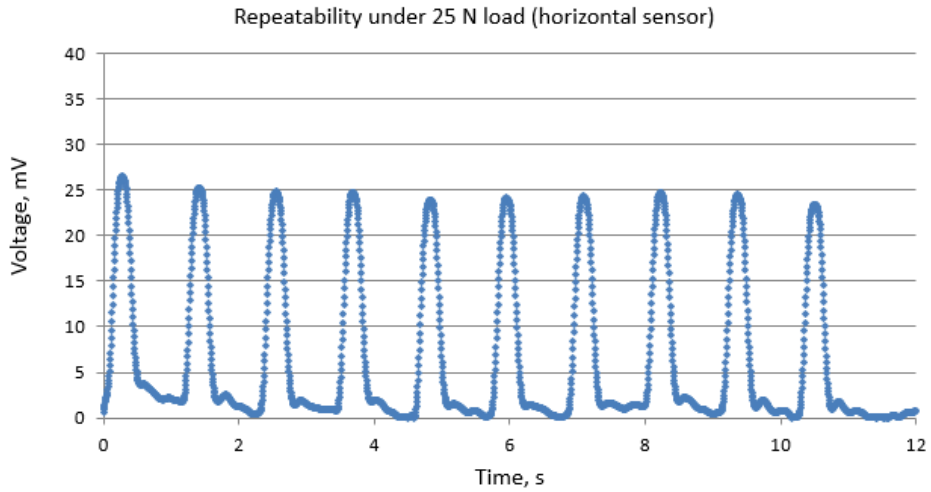

Figure 63: Repeatability test for the horizontal force sensor under $25\ N$ load applied 10 times at $\sim 1\ Hz$ frequency

4.3.3 Validation of Mechanical Amplification

Before discussing the sensor calibration process, the mechanical amplification of the vertical force sensor design is verified experimentally. To accomplish this, first the theoretical (from simulation) amplification factor is evaluated using FEA. Since the design was slightly modified and a different material was used, the resulting amplification was expected to be different than the original proposed design. The boundary condition and input displacement locations are shown in Figure 64-A. The input displacement to the finite element model was $40\ \mu m$ and applied at the center as shown in Figure 64-A. The resulting displacement at the sensing structure tip is $77\ \mu m$ (Figure 64-B). Therefore, an amplification of 93% is achieved with the vertical force sensing structure design.

A B

Figure 64: Demonstration of deformation amplification due to the vertical force sensing structure design using FEA. A, Applied displacement ($40\ \mu m$) at the center. B, Resultant deformation at the sensing structure tip

For the experimental validation, an input displacement of $40\ \mu m$ (maximum) was applied at $10\ \mu m$ increments using the SCARA robot. The displacement was applied at two locations; center of the structure which makes contact with the tooth and end of the structure as shown in Figure 65.

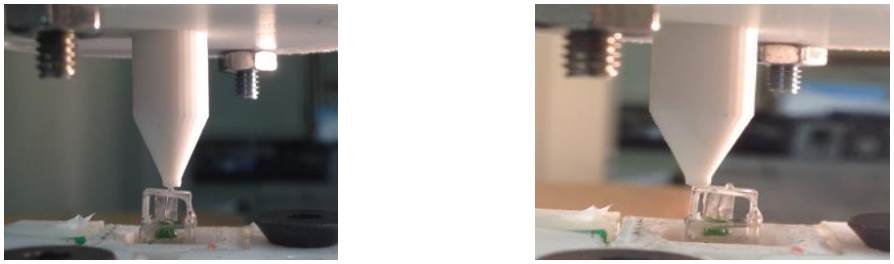

A B

Figure 65: Applied displacement ($40\ \mu m$) at the vertical force sensing structure for experimental verification. A, Center of the vertical force sensing structure. B, End of the vertical force sensing structure

To determine the amplification factor, the output voltage due to the input displacement at the center and at the end of the vertical force sensing structure

is plotted on the same graph as shown in Figure 66. The slope for each of the two responses is compared to evaluate the amplification factor. According to the analysis, the experimental amplification factor is calculated to be $(4.62 - 2.44)/2.44 = 89\%$ compared to the theoretical amplification factor of 93%.

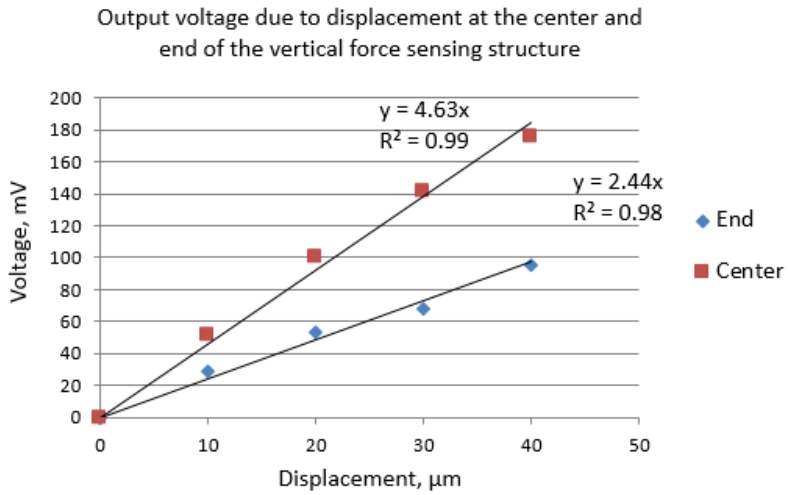

Figure 66: Output voltage due to input displacement applied at the center and end locations of the vertical force sensing structure

The slope for each of the two responses is compared to evaluate the amplification factor. According to the analysis, the experimental amplification factor is calculated to be $(4.62 - 2.44)/2.44 = 89\%$ compared to the theoretical amplification factor of 93%.

4.4 Methodology for Sensor Calibration

This section presents the methodology for vertical and horizontal force sensors calibration in Subsection 4.4.1 and 4.4.2 respectively. With the full assembly of the molar tooth and sensing mechanism secured in the robot workspace, controlled load is applied on the molar tooth occlusal surface. Using

the calibrated/known load cell readings, correlations are established between the applied load and force sensor readings to demonstrate that the proposed tooth embeddable two-axis force sensor can estimate the total force from the independent vertical and horizontal force sensor readings within a reasonable accuracy. Lastly, the calibration equations are validated with different load angles in Subsection 4.4.3.

The SCARA robot was programmed to apply controlled and repeated vertical and oblique loads on the molar tooth. This was accomplished by utilizing the robot trajectory. To apply the vertical load, the robot manipulator moves vertically down from point P to the occlusal surface as shown in Figure 67-A.

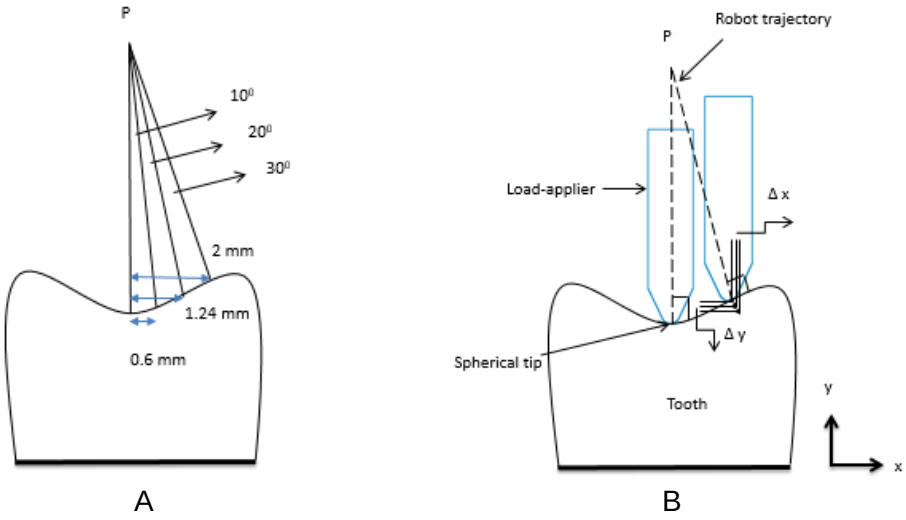

Figure 67: Schematic diagrams illustrating the load application procedure. A, Contact locations on the occlusal surface for $10\ deg$, $20\ deg$, and $30\ deg$ load angles. B, Robot trajectory during vertical and oblique load applications

However, for the oblique (angled) load the contact point at the occlusal surface is offset from the center. The manipulator travels from point P to the

specified point based on a desired angle as illustrated in Figure 67-B. Since the robot takes the shortest route to reach a specified point, a desired load angle may be obtained by defining the start and end point of the trajectory. The load was applied by applying incremental displacements in the vertical and horizontal directions (Figure 67-B). Furthermore, the load cell was augmented with an auxiliary cylindrical shape load-applier with a spherical tip. Due to the spherical tip, the applied load acts perpendicular to the surface which emulates the clinical loading scenario. According to the literature survey, researchers mostly apply up to $30\ deg$ angular load to simulate mastication loading.[114,115] Hence, in the present study the calibration was performed for up to $30\ deg$ loading condition.

4.4.1 Vertical Force Sensor Calibration

The calibration of the vertical force sensor was performed by evaluating two separate equations. Figure 68 shows the sensor responses for $0\ deg$, $5\ deg$, $20\ deg$, and $30\ deg$ loading conditions. Note that the vertical force sensor output decreases and the horizontal force sensor output increases with the increasing load angles. This was expected due to the fact that as the angle increases, the load decomposes and the vertical and horizontal force components are applied further away from the center of the occlusal surface. Consequently, a higher force is required to generate the same output as the $0\ deg$ loading at the center. Similarly, for the horizontal force sensor reading, the tooth experiences higher horizontal force with the increasing load angles due to the cuspal inclinations and hence the increase in voltage output.

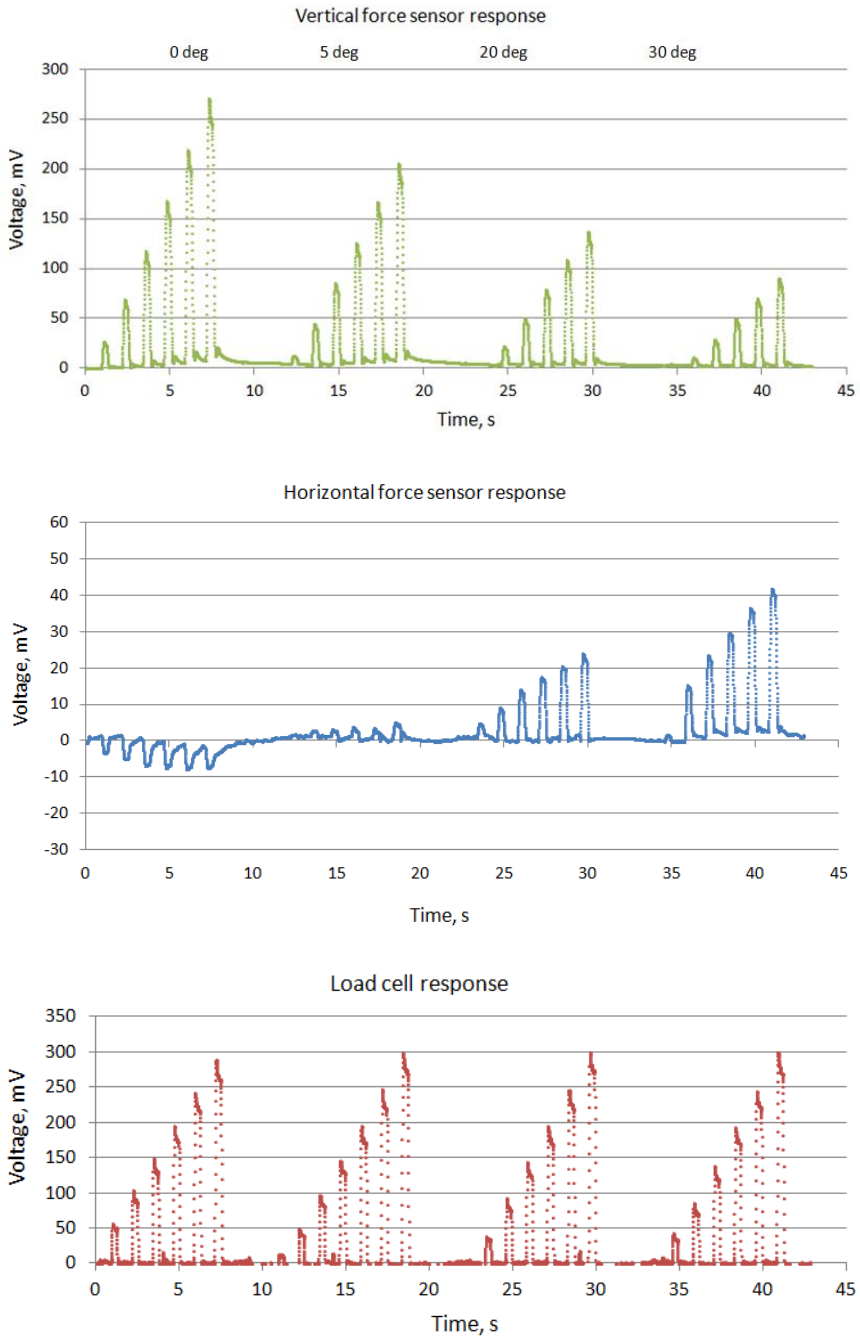

Figure 68: Vertical force sensor, horizontal force sensor and load cell responses under $0\ deg$, $5\ deg$, $20\ deg$, and $30\ deg$ loading conditions

For the load cell response, however, the output voltages are of same magnitudes (approximately) indicating that the total force experienced by the tooth is approximately the same for all four loading conditions. These loading conditions were repeated ($0\ deg$, $10\ deg$, $20\ deg$ and $30\ deg$) three times and similar responses were observed. Since the total force experienced by the tooth is same for all the loading conditions, the vertical and horizontal forces from the sensors can be related with the total applied force by Equation 19.

$$F_L = \sqrt{{F_v}^2 + {F_h}^2} \qquad \text{Equation 19}$$

In Equation 19, F_L is the total force (load cell), F_v is the vertical force component and F_h is the horizontal force component. Using this relationship, correlation equations are established to estimate the total forces from the vertical and horizontal force sensor outputs.

First, the vertical force sensor was calibrated separately for vertical and oblique loads. Once the vertical force sensor calibration equation is obtained, the horizontal force sensor is calibrated by rearranging Equation 19. The separate calibration equations for the vertical force sensor are based on the horizontal force sensor outputs. For $0\ deg$ loading condition, the voltage output from the horizontal force sensor is always negative as shown in Figure 68. However, under oblique loading conditions, the readings are positive. The negative output from the horizontal force sensor is attributed to the fact that the tooth deforms sideways (slightly) in response to the vertical occlusal load applied at the center as illustrated in Figure 69.

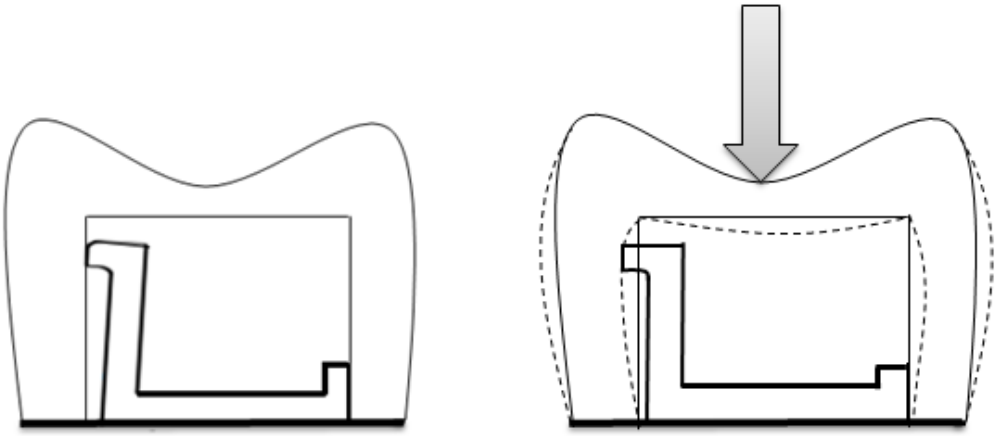

A B

Figure 69: Schematic diagrams explaining negative horizontal force sensor voltage. A, Horizontal force sensing beam position as contact is established with the tooth side wall. B, Sideways deformation due to vertical load

Since the horizontal force sensor has some amount of preload applied to it (due to the way contact is established with the tooth side wall during insertion inside the cavity as shown in Figure 69-A), the sensor will always show some negative output voltage in response to the vertical load. However, this negative voltage is small and does not exceed a certain value ($\sim 8\ mV$). If a perfectly upright position is obtained in the process of establishing contact with the tooth side wall then this negative voltage may be set to zero.

Thus, the calibration of the vertical force sensor is accomplished based on the horizontal force sensor reading. If the horizontal force sensor reading is negative, then the first calibration equation is used, otherwise (if zero or positive voltage) the second equation is used. The first calibration equation (for negative

horizontal sensor reading) is obtained by using the vertical force sensor outputs for $0\ deg$ loading condition. The force and output voltage are linearly correlated with a regression coefficient of 0.98 as shown in Figure 70.

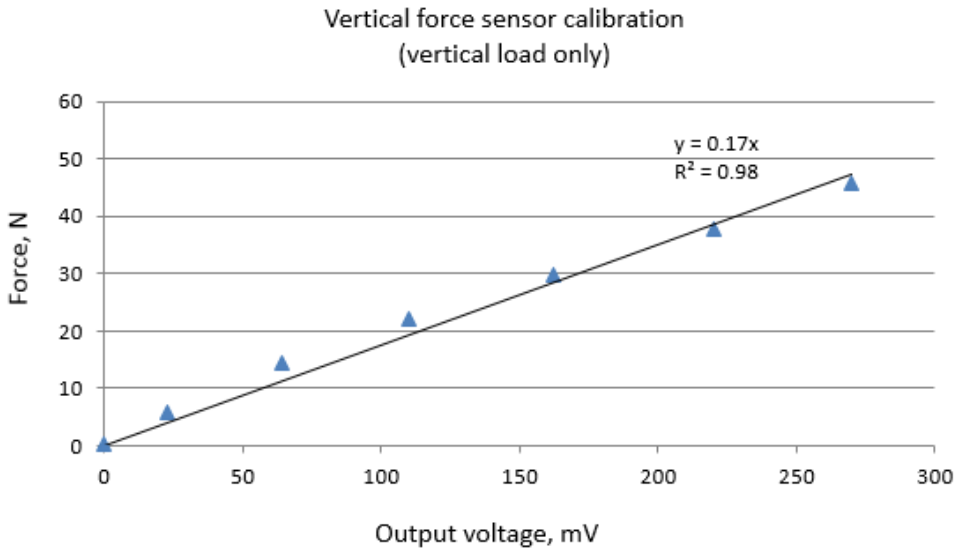

Figure 70: Calibration equation for the vertical force sensor given negative voltage from the horizontal force sensor

Next, the vertical force sensor is calibrated (horizontal sensor with zero or positive reading) with $5\ deg$ oblique loading condition. This angle was selected because the horizontal force sensor readings for the $5\ deg$ loading condition are very small compared to the $20\ deg$ and $30\ deg$ loading conditions. Ideally, the horizontal force sensor should have zero output voltage for the vertical force sensor calibration purpose. The calibration graph is shown in Figure 71. The force and voltage output are linearly correlated with a regression coefficient of 0.97.

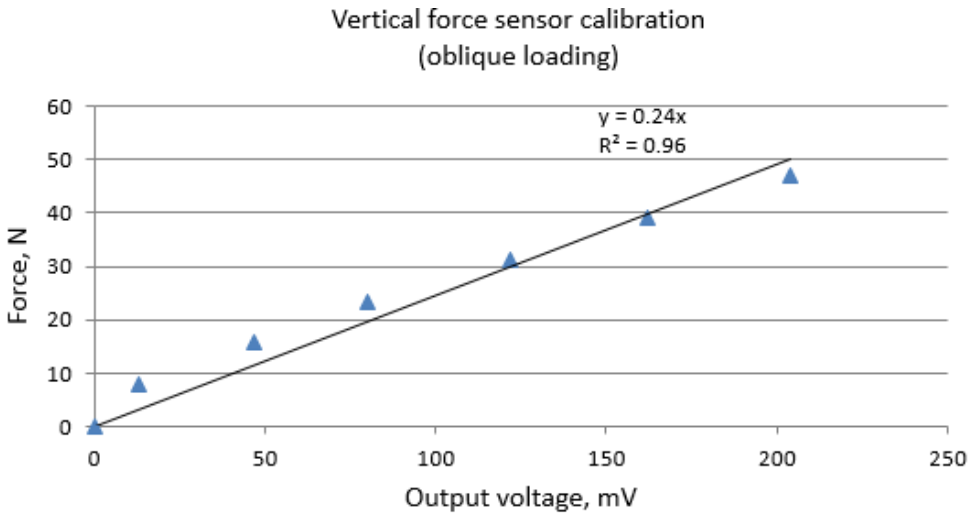

Figure 71: Vertical force sensor calibration given zero or positive horizontal force sensor voltage output

The final calibration equations for the vertical sensor are given in Equation 20, where F_V is the vertical force, v_h is the horizontal force sensor voltage output and v_v is vertical force sensor voltage output.

$$F_V = 0.17 v_v \text{ (if } v_h < 0\text{)}$$
$$F_V = 0.24 v_v \text{ (if } v_h \geq 0\text{)} \qquad \text{Equation 20}$$

4.4.2 Horizontal Force Sensor Calibration

With the vertical force sensor equation for the oblique loads, the horizontal force sensor calibration equation is obtained by assuming a linear relationship between the applied load and output voltage. Using the obtained calibration equation for $v_h \geq 0$ given in Equation 20, first the vertical forces were calculated for $20\ deg$ and $30\ deg$ loading conditions. Since the resultant forces for all angles are equal, the linear equation is set up to estimate the slope by minimizing the errors between the known (load cell) and estimated forces for

$20\ deg$ and $30\ deg$ loading conditions. The average error between the estimated and applied force is $\sim 4\%$. The obtained calibration equation for the horizontal force sensor is presented in Equation 21.

$$F_H = 1.09 v_h \qquad \text{Equation 21}$$

4.4.3 Validation of the Calibration Methodology

With the calibrated vertical and horizontal force sensors, the next step was to verify if these equations can accurately estimate forces applied at different load angles. To accomplish this, forces were estimated in three different configurations ($15\ deg$, $25\ deg$, and $35\ deg$) which are different than the ones used to calibrate the sensors. The maximum applied load was $45\ N$ with six load points for each load configuration at an increment of $\sim 7.5\ N$. Three replicates were collected for each load configuration; since the magnitudes of all the load points in any configuration were similar only a single set is used. The points of contact on the occlusal surface were $0.9\ mm$ $1.6\ mm$, and $2.4\ mm$ away from the central fossa for $15\ deg$, $25\ deg$, and $35\ deg$ loading conditions respectively.

Figure 72 shows the estimated vertical force components and the applied forces in the same graph. The vertical forces were obtained from the vertical force sensor readings and the applied forces were based on the load cell readings. The maximum vertical forces are observed for the $15\ deg$ loading condition and the minimum forces are observed for $35\ deg$ loading condition. Furthermore, the vertical force components decrease with increasing load angle.

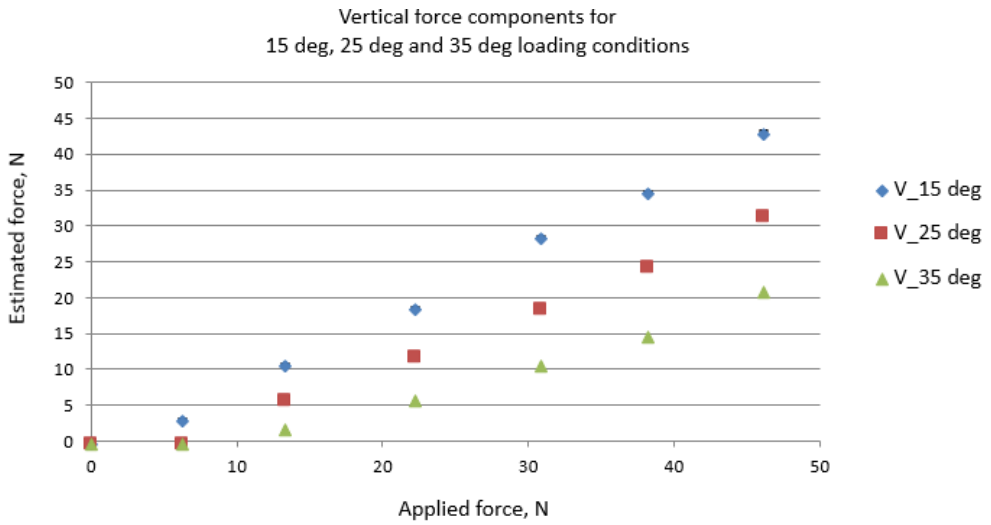

Figure 72: Estimated vertical force components for $15\ deg$, $25\ deg$, and $35\ deg$ loading conditions

The reason for this is attributed to the offset location of the applied load in relation to the load angle. For any offset loading, the maximum deformation at the lower occlusal surface is smaller than the deformation for the same load applied at the central fossa. The further away the location of contact from the central fossa, the smaller the deformation. Since the offset distance increases with increasing load angle, the deformation decreases which leads to the reduced voltage output for the vertical force sensor. Furthermore, the sensor will not respond until a certain amount of force (threshold) is applied on the cusp. However, the sensor may be able to respond to the same load applied on the central fossa. This is evident in $25\ deg$ and $35\ deg$ loading responses as shown in Figure 72, where the sensor voltage outputs are zero even though $\sim 7\ N$ load is applied. For a load greater than this threshold, the sensor is able respond under all loading conditions.

Similarly, the horizontal force components were estimated using the horizontal force sensor calibration equation and are presented in Figure 73. The highest forces are obtained for the $35\ deg$ loading condition and lowest forces are obtained for the $15\ deg$ loading condition.

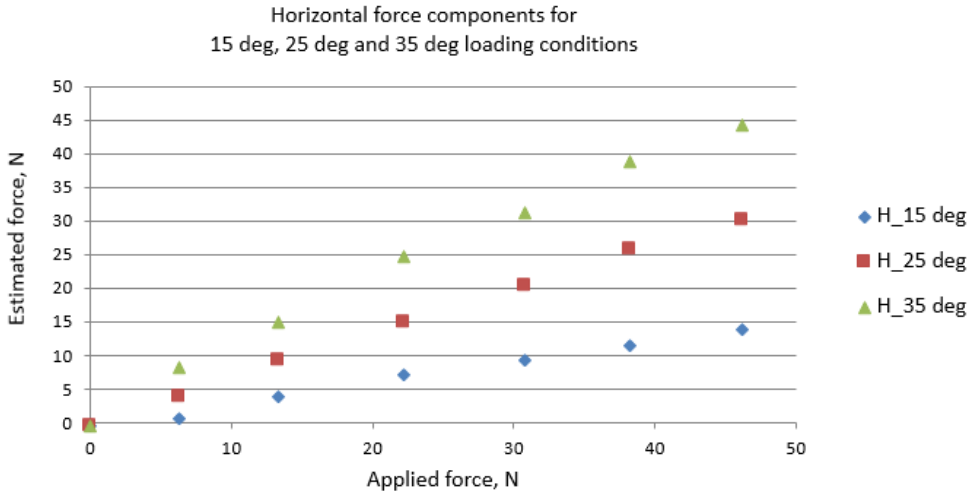

Figure 73: Estimated horizontal force components for $15\ deg$, $25\ deg$, and $35\ deg$ loading conditions

The reason for this is also attributed to the increasing offset distance of the load application location with increasing load angle. The load application locations are spatially distributed in the occlusal surface to enable oblique load application. As the distance increases from the central fossa, the cusp height (measured from the lower occlusal surface) increases due to the $10\ deg$ cuspal inclination of the semi-anatomic tooth. This elevated cusp provides more resistance to the horizontal force component leading to a higher sideway deformation of the tooth, which explains the reason for a higher horizontal force sensor voltage output under a higher load angle.

Lastly, the total forces are calculated from the estimated horizontal and vertical force components and compared with the total applied forces as shown in Figure 74. The average percent error between the estimated and applied forces is $\sim 5\%$.

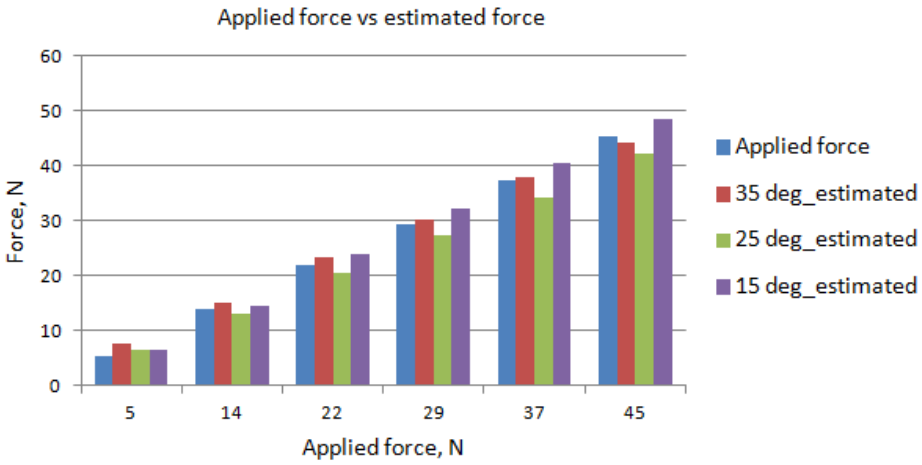

Figure 74: Applied and estimated forces for $15\ deg$, $25\ deg$, and $35\ deg$ loading conditions

4.5 Summary

This chapter presented the design of the experimental testbed and the associated experimental analyses to verify the feasibility of the proposed two-axis tooth embeddable force sensor. The molar tooth and the force sensing structures (vertical and horizontal) are fabricated using additive manufacturing technology. Next, the components are assembled in order to perform experiments for the sensor characterization and calibration. A SCARA robot is used for the load application. The sensor response characterization indicated a dominant overdamped response which was approximated with an equivalent first

order system. Next, the transfer functions of the vertical and horizontal force sensors are determined and the experimental and theoretical responses shown to be in good agreement with each other. The sensor behavior under dynamic loading is investigated by applying a repeated step load (10 times) at a frequency of $1\ Hz$. Both sensors exhibited good repeatability and are expected to be able to reliably measure the mastication loads quite. The vertical force sensor requires two calibration equations which are governed by the horizontal force sensor outputs. The horizontal force sensor is calibrated by curve fitting experimental data for oblique loading conditions. Finally, the calibration equations are validated by estimating applied and sensed forces at different load configurations. It is shown that the designed two-axis force sensor can estimate vertical and oblique occlusal loads on the occlusal surface within an accuracy of 95%.

5 Conclusions and Recommendations for Future Research

5.1 Conclusions

In this research, the conceptual design and development of a tooth embeddable force sensor to induce artificial proprioception in the full arch fixed implant prosthesis is proposed. A novel tooth embeddable sensing mechanism is designed and developed to provide biofeedback to the denture wearer and prevent occlusal overload in the full arch fixed implant restorations. The 1st molar tooth is selected for the sensor integration because it is known to experience the highest occlusal load during mastication. Lingualized occlusion is selected as the centric occlusion scheme which ensures occlusal contacts at the central fossae of the posterior teeth. A cavity is created inside the artificial tooth and effects of various geometric parameters and material Young's modulus are analyzed (using FEA) to obtain deformations at the lower occlusal surface and the tooth side wall. The proposed sensing mechanism is based on the induced deformation, and features a vertical and a horizontal force sensing structure to measure the vertical and horizontal forces on the occlusal surface respectively. The dimensions of the vertical force sensing structure are defined to amplify the deformation at the lower occlusal surface and increase the resultant strain at the sensor location. Similarly, the geometric dimensions of the horizontal force sensing structure were determined to fulfill the design criteria. The design is based on a $200\ N$ mastication load with $1\ Hz$ input frequency. The available space for the sensing structure integration inside the tooth is defined to be approximately $7\ mm\ x\ 7\ mm\ x\ 8\ mm$. The material for the tooth is acrylic resin

and for the sensing structure is titanium alloy ($Ti-6Al-4V$). The finalized sensing structure designs are prototyped out of polymeric material using additive manufacturing technology and strain gauges are mounted on the sensor beams. The fabricated components are then assembled mimicking the clinical denture assembly process and a SCARA robot is used for load application. The sensor responses are characterized using first order systems and mathematical models are developed to predict the sensor behavior. Both the sensors demonstrated good repeatability under dynamic loading of $1\ Hz$ frequency. Finally, the sensors are calibrated using the SCARA robot to closely mimic the clinical mastication loading patterns. A calibration methodology is developed for the two sensors and the total forces are estimated using the calibration equations. It is demonstrated that the calibration equations are able to estimate the total applied forces within an accuracy of 95%.

5.2 Recommendations for Future Research

Future research recommendations can be summarized as follows:

1. Titanium sensing structure should be used for the sensing mechanism. If the strain gauges are mounted on the titanium cantilever beams, the sensor responses will not exhibit stress relaxation behaviors as observed with the somos cantilever beams and the response should reach its steady state value very quickly. People with parafunctional habit such as grinding or clenching exert occlusal loads which may last up to five to seven seconds occasionally. Since the force sensor output with a viscoelastic material beam gradually decays

with time, the estimated force may be erroneous. This could be avoided by using a titanium metal beam which is biocompatible and extensively used for dental applications.

2. Semiconductor strain gauges may be investigated as an alternative to the metal foil strain gauges. These gauges have higher gauge factors (~ 200) and could increase the measurement sensitivity. They are available in higher resistance range with small volumetric footprints. Furthermore, these gauges consume less power and are suitable for small strain applications as is the case with the present study.

3. For the proposed two-axis force sensor, the sensing mechanism is designed to measure the occlusal loads on one side of the cusp only. However, an additional sensing element may be incorporated in the sensing mechanism to measure the applied loads in both cusps.

4. It is recommended that ex-vivo testing be performed in the full arch fixed implant prosthesis. An artificial masticator can be used for the load application. The artificial masticator can replicate the clinical jaw motions and occlusion schemes and is widely used in clinical dentistry.

5. Effect of temperature (inside the mouth) on the sensor performance needs to be investigated. If the change of temperature causes potential thermal drift, then a temperature compensation method will be required. The design has the flexibility to incorporate two strain gauges on either side of each beam which could be used to introduce temperature compensation mechanism with a half bridge Wheatstone bridge circuit configuration.

6. Sensor electronics are integral parts of the proposed approach and required to be incorporated inside the mouth. Figure 75 shows the block diagram of the sensor electronics. The components inside the implantable device setup are a signal conditioning unit, a micro-controller unit and a transmitter. The essentials of the signal conditioning circuit unit are discussed in Section 4.1.2. The transmitter is required for wireless signal transmission. The micro-controller unit may be required to activate or deactivate the transmitter based on preset conditions. This kind of regulation is performed to reduce power consumption.

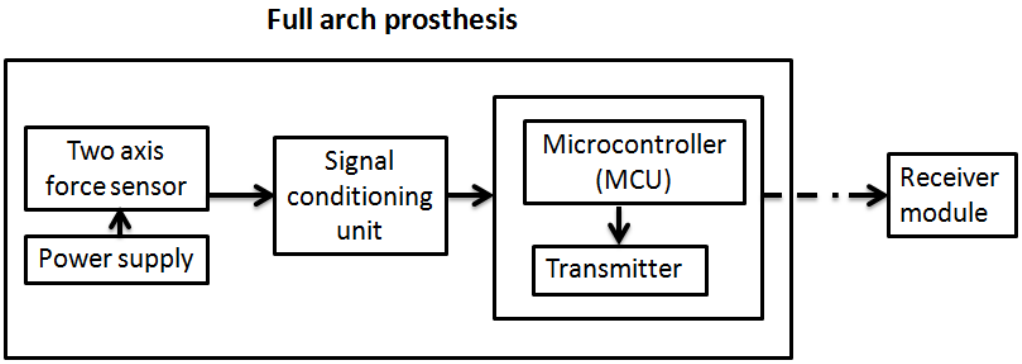

Figure 75: Block diagram of the sensor electronics

For the power supply, there are two options available: battery and wireless power supply/energy harvesting. Batteries have been extensively used in implantable medical devices such as pacemaker, cochlear implant, drug delivery systems etc.[116] However, due to limited capacity and relatively bigger size, the wireless power supply may be more suitable. Common examples of wireless energy transfer methods are capacitive coupling, inductive coupling etc. Sources of energy harvesting include kinetic energy (vibration, body motion, etc.), RF radiation energy, thermal energy, etc.[117]

6 Appendix

6.1 Appendix A

6.1.1 Tooth model

The bucco-lingual and mesio-distal cross sections of the molar tooth are presented in Figure 76. Fillets ($0.4\ mm$) are added inside the edges of the cavity to avoid false stress concentration.

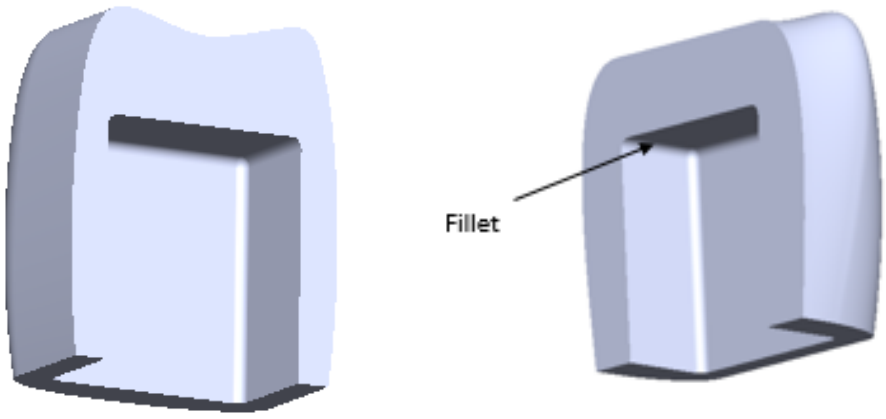

A B

Figure 76: Cross-sectional view of the molar tooth model. A, Bucco-lingual cross section. B, Mesio-distal cross section

6.2 Appendix B

6.2.1 Sensing Mechanism dimensions

The dimensions of the vertical and horizontal force sensing structures are presented in Figure 77 and Figure 78 respectively.

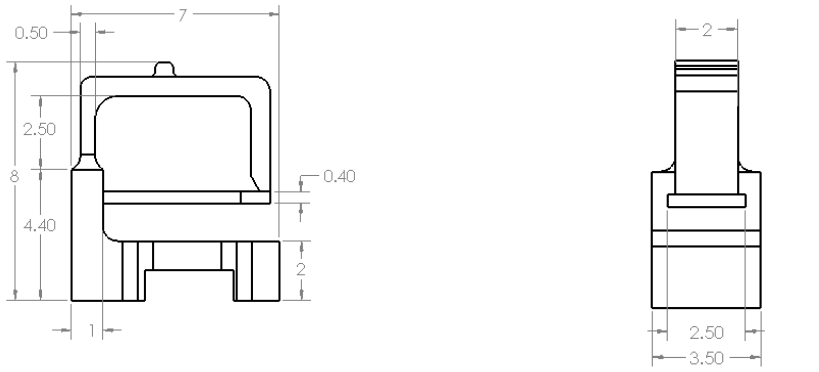

A B

Figure 77: Dimensions (mm) of the vertical force sensing structure. A, Front view. B, Side view

These dimensions are based on a cavity size of approximately $7\ mm\ x\ 7\ mm\ x\ 8\ mm$ and may be adjusted based on design requirements.

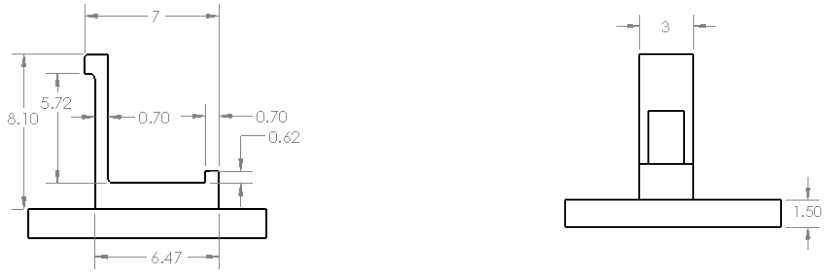

A B

Figure 78: Dimensions (mm) of the horizontal force sensing structure. A, Front view. B, Side view

7 References

1. Sanger MH.:Periodontal and dental implant education and information. [Internet] [cited 2014 Apr 9]. Available from:http://www.sangerdds.com/patient-education.html
2. Bagde AD, Jaju SB, Patil PG.:A review on FEM analysis of mandibular overdenture implant. Int J Innov Res Sci Eng Technol 2013;2:2137–44
3. Douglass CW, Shih A, Ostry L.:Will there be a need for complete dentures in the United States in 2020? J Prosthet Dent 2002;87:5–8
4. The Academy of Prosthodontics.:The glossary of prosthodontic Terms. J Prosthet Dent 2005;94:10–92
5. WebMD.:Dental health and dentures. [Internet] [cited 2014 Sep 7]. Available from: http://www.webmd.com/oral-health/dental-health-dentures
6. Associates D.:Dentures, partial dentures and removable appliances. [Internet] [cited 2014 Sep 7]. Available from: http://www.dentalassociates.com/general-dentistry/dentures-partial-dentures-removable-appliances/
7. Robison NE, Tantbirojn D, Versluis A, et al.:Failure strengths of denture teeth fabricated on injection molded or compression molded denture base resins. J Prosthet Dent 2016;116:292–9
8. Junior JFS, Pellizzer EP, Verri FR, et al.:Stress analysis in bone tissue around single implants with different diameters and veneering materials: a 3-D finite element study. Mater Sci Eng C 2013;33:4700–14
9. Dental health of colorado.:Dentures. [Internet] [cited 2016 Jun 12]. Available from: http://www.dentalhealthcolorado.com/dentures/

10. Dentist J.:Classification of edentulous ridges for fixed partial dentures. [Internet] [cited 2014 Sep 10]. Available from: http://www.juniordentist.com/classification-of-edentulous-ridges-for-fixed-partial-dentures.html
11. Dedicated Dental Group.:Dental implants, fixed bridges, or dentures? [Internet] [cited 2014 Sep 7]. Available from: http://www.dedicateddentist.com/dental-implants/dental-implants-fixed-bridges-or-dentures/
12. Doblare M, Merodio J.:Biomechanics. Eolss Publishers Co. Ltd, 2015.
13. Dental Implants-01.com.:Types of dental implants. [Internet] [cited 2014 Sep 10]. Available from: http://www.dental-implants-01.com/types-of-dental-implants.htm
14. Ebadian B, Talebi S, Khodaeian N, et al.:Stress analysis of mandibular implant-retained overdenture with independent attachment system: effect of restoration space and attachment height. Gen Dent 2015;63:61–7
15. Misch CE.:Mandibular and maxillary implant overdenture design and fabrication. In: Dental Implant Prosthetics Second Ed. Elsevier Inc., 2015. p. 753–828
16. Misch CE.:Dental implant prosthetics. Elsevier Health Sciences, 2014. p 1008
17. Dental S.:Dental Implants. [Internet] [cited 2014 Sep 11]. Available from: http://www.samdental.org/treatment-list/dental-implants/#!
18. Care VSD.:Dental implants. [Internet] [cited 2014 Sep 11]. Available from: http://vasmilesdental.com/site/?page_id=360
19. Affordable Dentures & Implants.:Affordable implant solutions. [Internet]

[cited 2016 Dec 6]. Available from: http://www.affordabledentures.com/implants/affordable_implant_solutions.html

20. Chee W, Jivraj S.:Treatment planning of the edentulous mandible. Br Dent J 2006;201:337–47

21. Davies SJ, Gray RJM, Young MPJ.:Good occlusal practice in the provision of implant borne prostheses. Br Dent J 2002;192:79–88

22. Kwon T, Bain P a., Levin L.:Systematic review of short- (5-10 years) and long-term (10 years or more) survival and success of full-arch fixed dental hybrid prostheses and supporting implants. J Dent Elsevier Ltd, 2014;42:1228–41

23. Papaspyridakos P, Chen C-J, Chuang S-K, et al.:A systematic review of biologic and technical complications with fixed implant rehabilitations for edentulous patients. Int J Oral Maxillofac Implants Centre for Reviews and Dissemination (UK), 2012;27:102–10

24. Bidez MW, Misch CE.:Force transfer in implant dentistry: basic concepts and principles. J Oral Implantol 1992;18:264–74

25. Orleans N.:Bone remodeling I : theory of adaptive elasticity. 1976;6:313–26

26. Frost HM.:Bone “mass” and the “mechanostat”: a proposal. Anat Rec 1987;219:1–9

27. Priest G, Smith J, Wilson MG.:Implant survival and prosthetic complications of mandibular metal-acrylic resin implant complete fixed dental prostheses. J Prosthet Dent 2014;111:466–75

28. Dhima M, Paulusova V, Lohse C, et al.:Practice-based evidence from 29-year outcome analysis of management of the edentulous jaw using osseointegrated dental implants. J Prosthodont 2014;23:173–81

29. Purcell BA, McGlumphy EA, Holloway JA, et al.:Prosthetic complications in mandibular metal-resin implant-fixed complete dental prostheses: a 5- to 9-year analysis. Int J Oral Maxillofac Implants 2008;23:847–57

30. Aglietta M, Siciliano VI, Zwahlen M, et al.:A systematic review of the survival and complication rates of implant supported fixed dental prostheses with cantilever extensions after an observation period of at least 5 years. Clin Oral Implants Res 2009;20:441–51

31. McCracken M, Ouellette JP.:Bruxzir solid zirconia full-arch implant prosthesis: clinical and scientific compendium. [Internet] [cited 2015 Feb 5]. Available from: http://www.glidewelldental.com/services/

32. Misch CE, Suzuki JB, Misch-Dietsh FM, et al.:A positive correlation between occlusal trauma and peri-implant bone loss: literature support. Implant Dent 2005;14:108–16

33. Fu J-H, Hsu Y-T, Wang H-L.:Identifying occlusal overload and how to deal with it to avoid marginal bone loss around implants. Eur J Oral Implantol 2012;5:91–103

34. Dănilă V, Augustin M.:Occlusal overload--a risk factor in implant based prostheses. Rev medico-chirurgicală a Soc Medici şi Nat din Iaşi 2010;114:214–7

35. Oh T-J, Yoon J, Misch CE, et al.:The causes of early implant bone loss:

myth or science? J Periodontol 2002;73:322–33

36. Hsu Y-T, Fu J-H, Al-Hezaimi K, et al.:Biomechanical implant treatment complications: a systematic review of clinical studies of implants with at least 1 year of functional loading. Int J Oral Maxillofac Implants 2012;27:894–904

37. Kim Y, Oh T-J, Misch CE, et al.:Occlusal considerations in implant therapy : clinical guidelines with biomechanical rationale. Clin Oral Implants Res 2005;16:26–35

38. Chambrone L, Chambrone L a, Lima L a.:Effects of occlusal overload on peri-implant tissue health: a systematic review of animal-model studies. J Periodontol 2010;81:1367–78

39. M. Trulsson HSJG.:Food-holding and biting behavior in human subjects lacking periodontal receptors. J Dent Res 77:574–82

40. Grieznis L, Apse P, Blumfelds L.:Passive tactile sensibility of teeth and osseointegrated dental implants in the maxilla. Stomatologija 2010;12:80–6

41. Misch CE.:Stress treatment theorem for implant dentistry: the key to implant treatment plans. In: Dental Implant Prosthetics 2nd Ed. Elsevier Health Sciences, 2014. p. 161

42. Hasan MA, Shiakolas PS.:3D finite element stress analysis of an implant supported overdenture under bruxism and lingualized loading conditions. In: Volume 3: Biomedical and Biotechnology Engineering ASME, 2015. p. V003T03A043

43. Manfredini D, Bucci MB, Sabattini VB, et al.:Bruxism: overview of current knowledge and suggestions for dental implants planning. Cranio - J Craniomandib Pract 2011;29:304–12

44. BruxismBiofeedbackHeadband.com.:Teeth grinding - bruxism. [Internet] [cited 2014 Sep 13]. Available from: http://bruxismbiofeedbackheadband .com/about-bruxism/

45. Gu W, Yang J, Zhang F, et al.:Efficacy of biofeedback therapy via a mini wireless device on sleep bruxism contrasted with occlusal splint: A pilot study. J Biomed Res Education Department of Jiangsu Province, 2015;29:160–8

46. Lobbezoo F, Brouwers JEIG, Cune MS, et al.:Dental implants in patients with bruxing habits. J Oral Rehabil 2006;33:152–9

47. Johansson A, Omar R, Carlsson GE.:Bruxism and prosthetic treatment: a critical review. J Prosthodont Res 2011;55:127–36

48. Sarmento HR, Dantas RVF, Pereira-Cenci T, et al.:Elements of implant-supported rehabilitation planning in patients with bruxism. J Craniofac Surg 2012;23:1905–9

49. Brunski JB.:Biomaterials and biomechanics in dental implant design. Int J Oral Maxillofac Implants 1988;3:85–97

50. Schulte W.:Implants and the periodontium. Int Dent J 1995;45:16–26

51. Aparna IN, Dhanasekar B, Lingeshwar D, et al.:Implant crest module: a review of biomechanical considerations. Indian J Dent Res 2012;23:257–63

52. Yuan JC-C, Sukotjo C.:Occlusion for implant-supported fixed dental prostheses in partially edentulous patients: a literature review and current concepts. J Periodontal Implant Sci 2013;43:51–7

53. Jambhekar S, Kheur M, Kothavade M, et al.:Occlusion and occlusal considerations in implantology. Indian J Dent Adv 2010;2:125–30

54. Lang BR.:Complete denture occlusion. Dent Clin North Am 2004;48:641–65

55. Sidana V, Bhasin S, Makkar M, et al.:Group function occlusion. Indian J Oral Sci 2012;3:124

56. Prasad D. K, Prasad BR, Bardia A, et al.:Enhancing stability: a review of various occlusal schemes in complete denture prosthesis. Nitte Univ J Heal Sci 2013;3:105–12

57. Michalakis KX, Calvani P, Hirayama H.:Biomechanical considerations on tooth-implant supported fixed partial dentures. J Dent Biomech 2012;3:1758736012462025

58. McAuliffe P, Kim JH, Diamond D, et al.:A sleep bruxism detection system based on sensors in a splint - pilot clinical data. J Oral Rehabil 2014;42:34–9

59. Kim JH, McAuliffe P, O'Connell B, et al.:Development of wireless bruxism monitoring device based on pressure-sensitive polymer composite. Sensors Actuators, A Phys Elsevier B.V., 2010;163:486–92

60. Dylina TJ.:A common-sense approach to splint therapy. J Prosthet Dent 2001;86:539–45

61. Kato T, Masuda Y.:Masseter EMG activity during sleep and sleep bruxism. Arch Ital Biol 2011;478–91

62. Lantada AD, Bris CG, Morgado PL, et al.:Novel system for bite-force sensing and monitoring based on magnetic near field communication. Sensors (Basel) 2012;12:11544–58

63. Hussain M, Choa Y-H, Niihara K.:Fabrication process and electrical behavior of novel pressure-sensitive composites. Compos Part A Appl Sci Manuf 2001;32:1689–96

64. Nordlander JY, Gallia LJ.:Method and apparatus for sensing and treating bruxism. US Patent 5078153. 1992.

65. Summer JD, Bodegom E, Lee A.:Intraoral jaw tracking device. US, 5989023, 1999

66. Ilovar S, Zolger D, Castrillon E, et al.:Biofeedback for treatment of awake and sleep bruxism in adults: systematic review protocol. Syst Rev 2014;3:42

67. Abichandani SJ, Bhojaraju N, Guttal S, et al.:Implant protected occlusion : A comprehensive review. Eur J Prosthodont 2013;1:29–36

68. Fernandes CP, Glantz P-OJ, Svensson SA, et al.:A novel sensor for bite force determinations. Dent Mater 2003;19:118–26

69. Chen Y-Y, Kuan C-L, Wang Y-B.:Implant occlusion: biomechanical considerations for implant-supported prostheses. J Dent Sci 2008;3:65–74

70. Basso MFM, Nogueira SS, Arioli-Filho JN.:Comparison of the occlusal vertical dimension after processing complete dentures made with

lingualized balanced occlusion and conventional balanced occlusion. J Prosthet Dent 2006;96:200–4

71. Prasad DK.:Enhancing stability: A review of various occlusal schemes in complete denture prosthesis. Nitte Univ J Heal Sci 2013;3:105–12

72. Gross M.:Occlusion in implant dentistry. A review of the literature of prosthetic determinants and current concepts. Aust Dent J 2008;53:60–3

73. Apicella A, Masi E, Nicolais L, et al.:A finite-element model study of occlusal schemes in full-arch implant restoration. J Mater Sci Mater Med 1998;9:191–6

74. Madalli P, Murali CR, Subhas S, et al.:Effect of occlusal scheme on the pressure distribution of complete denture supporting tissues : an in vitro study. J Int Oral Heal 2015;7:68–73

75. Heintze SD, Monreal D, Rousson V.:Fatigue resistance of denture teeth. J Mech Behav Biomed Mater Elsevier, 2016;53:373–83

76. Ferreira MB, Barão VA, Faverani LP, et al.:The role of superstructure material on the stress distribution in mandibular full-arch implant-supported fixed dentures. A CT-based 3D-FEA. Mater Sci Eng C Mater Biol Appl 2014;35:92–9

77. Mark HF.:Encyclopedia of polymer science and technology. Third Ed. John Wiley & Sons, Inc., 2013

78. Ciftci Y, Canay S.:The effect of veneering materials on stress distribution in implant-supported fixed prosthetic restorations. Int J Oral Maxillofac Implants 2000;15:571–82

79. Mericske-Stern R, Assal P, Mericske E, et al.:Occlusal force and oral tactile sensibility measured in partially edentulous patients with ITI implants. Int J Oral Maxillofac Implants 10:345–53

80. Fontijn-Tekamp FA, Slagter AP, Van Der Bilt A, et al.:Biting and chewing in overdentures, full dentures, and natural dentitions. J Dent Res 2000;79:1519–24

81. Alkan A, Keskiner I, Arici S, et al.:The effect of periodontal surgery on bite force, occlusal contact area and bite pressure. J Am Dent Assoc American Dental Association, 2006;137:978–83

82. Burkhart TA, Andrews DM, Dunning CE.:Finite element modeling mesh quality, energy balance and validation methods: A review with recommendations associated with the modeling of bone tissue. J Biomech 2013;46:1477–88

83. Suwannaroop P, Chaijareenont P, Koottathape N, et al.:In vitro wear resistance, hardness and elastic modulus of artificial denture teet. Dent Mater J 2011;30:461–8

84. Barão VAR, Assunção WG, Tabata LF, et al.:Finite element analysis to compare complete denture and implant-retained overdentures with different attachment systems. J Craniofac Surg 2009;20:1066–71

85. Darbar UR, Huggett R, Harrison A, et al.:Finite element analysis of stress distribution at the tooth-denture base interface of acrylic resin teeth debonding from the denture base. J Prosthet Dent 1995;74:591–4

86. Ferreira MB, Barão VA, Delben JA, et al.:Non-linear 3D finite element

analysis of full-arch implant-supported fixed dentures. Mater Sci Eng C Mater Biol Appl 2014;38:306–14

87. Göre E, Evlioğlu G.:Assessment of the effect of two occlusal concepts for implant-supported fixed prostheses by finite element analysis in patients with bruxism. J Oral Implantol 2014;40:69–75

88. Ates M, Cilingir A, Sulun T, et al.:The effect of occlusal contact localization on the stress distribution in complete maxillary denture. J Oral Rehabil Blackwell Publishing Ltd, 2006;33:509–13

89. Norton RL.:Machine design: an integrated approach. 4th ed. Upper Saddle River, N.J: Prentice Hall, 2010. p. 260-262

90. Koichi F.:Fatigue properties of acrylic denture base resins. J Chem Inf Model 1989;53:1689–99

91. Issa Salih S, Kadhum Oleiwi J, Adnan Hamad Q.:Investigation of fatigue and compression strength for the PMMA reinforced by different system for denture applications. Int J Biomed Mater Res 2015;3:5–13

92. Yousef H, Boukallel M, Althoefer K.:Tactile sensing for dexterous in-hand manipulation in robotics - a review. Sensors Actuators, A Phys Elsevier B.V., 2011;167:171–87

93. Chen LT, Chang JS, Hsu CY, et al.:Fabrication and performance of mems-based pressure sensor packages using patterned ultra-thick photoresists. Sensors 2009;9:6200–18

94. Carter S, Ned A, Chivers J, et al.:Selecting piezoresistive vs piezoelectric pressure Transducers. Kulite Semiconductor Products. 2010

95. Tekscan.:Flexiforce A101 sensor. [Internet] Available from: https://www.tekscan.com/products-solutions/force-sensors/a101

96. Giovanelli D, Farella E.:Force sensing resistor and evaluation of technology for wearable body pressure sensing. J Sensors Hindawi Publishing Corporation, 2016;2016:1–13

97. Tiwana MI, Redmond SJ, Lovell NH.:A review of tactile sensing technologies with applications in biomedical engineering. Sensors Actuators, A Phys Elsevier B.V., 2012;179:17–31

98. Sidambe AT.:Biocompatibility of advanced manufactured titanium implants-A review. Materials (Basel) 2014;7:8168–88

99. Hosseini S.:Fatigue of Ti-6Al-4V. In: Biomedical Engineering - Technical Applications in Medicine InTech, 2012. p. 75–92

100. Nuño N, Amabili M, Groppetti R, et al.:Static coefficient of friction between Ti-6Al-4V and PMMA for cemented hip and knee implants. J Biomed Mater Res 2002;59:191–200

101. Young WC, Budynas RG.:Roark's formulas for stress and strain. Seventh.New York: McGraw-Hill Companies, Inc., 1989.

102. Tang C-B, Liul S-Y, Zhou G-X, et al.:Nonlinear finite element analysis of three implant- abutment interface designs. Int J Oral Sci 2012;4:101–8

103. Niinomi M.:Mechanical properties of biomedical titanium alloys. Mater Sci Eng A 1998;243:231–6

104. Xu W, Brandt M, Sun S, et al.:Additive manufacturing of strong and ductile Ti–6Al–4V by selective laser melting via in situ martensite decomposition.

Acta Mater 2015;85:74–84

105. Rangert B, Krogh PHJ, Langer B, et al.:Bending overload and implant fracture: a retrospective clinical analysis. Int J Oral Maxillofac Implants 1997;10:326–34

106. Reeson MG, Jepson NJA.:Achieving an even thickness in heat-polymerized permanent acrylic resin denture bases for complete dentures. J Prosthet Dent 1999;82:359–61

107. El-Anwar MI, Mohammed MS.:Comparison between two low profile attachments for implant mandibular overdentures. J Genet Eng Biotechnol 2014;12:45–53

108. Tokyo Sokki Kenkyujo Co. L.:F series foil strain gauge. [Internet] [cited 2017 Mar 1]. Available from: http://www.tml.jp/e/product/strain_gauge_list/F_list.html

109. James ML.:Vibration of mechanical and structural systems: with microcomputer applications. Harper & Row, 1989. p. 652

110. Thompson WT.:Theory of vibrations with applications. Third. New Jersey: Prentice Hall, 1988.

111. Lumkes JH.:Control strategies for dynamic systems. New York: Marcel Dekker, Inc., 2002. p. 83

112. Barua B, Saha MC.:Incorporating temperature and density terms in the stretched exponential model in predicting stress relaxation behavior of polymer foams. J Eng Mater Technol 2015;138:1–7

113. Okada C, Ueda T, Sakurai K.:Blood flow in denture-supporting maxillary

mucosa in response to simulated mastication by loading. J Prosthodont Res Japan Prosthodontic Society, 2010;54:159–63

114. Assunção WG, Gomes EA, Barão VAR, et al.:Stress analysis in simulation models with or without implant threads representation. Int J Oral Maxillofac Implants 24:1040–4

115. Perillo L, Jamilian A, Shafieyoon A, et al.:Finite element analysis of miniscrew placement in mandibular alveolar bone with varied angulations. Eur J Orthod 2014;1–4

116. Bock DC, Marschilok AC, Takeuchi KJ, et al.:Batteries used to Power Implantable Biomedical Devices. Electrochim Acta 2012;84

117. Hannan MA, Mutashar S, Samad SA, et al.:Energy harvesting for the implantable biomedical devices: issues and challenges. Biomed Eng Online 2014;13:79

8 Biographical Information

Md Abu Hasan earned his bachelor's degree in mechanical engineering from IUT OIC, Bangladesh. He moved to the US in 2011 to pursue higher studies and started his PhD at the University of Texas Arlington (UTA). His research interests lie in the area of electromechanical design, biomedical device design, and prosthodontics. During his PhD at UTA, Hasan worked on multiple projects related to prosthodontics. He developed models of full mandibular jaw bone and fixed implant prosthesis and studied effects of centric and eccentric occlusal loading schemes using finite element analysis. As part of his PhD dissertation he designed and developed a two-axis force sensor to induce artificial proprioception in the mandibular full arch prosthesis. Hasan's future plan is to gain industrial job experience and continue to grow as a researcher. He also intends to continue his research work and contribute towards the improvement of full arch prosthesis rehabilitation modalities.